Universidade do Minho
Escola de Medicina

Ana Carolina Pinto Castro

HCN channelopathy as a key mechanism for auditory hypersensitivity in a *Shank3* mouse model of ASD

outubro de 2022

HCN channelopathy as a key mechanism for auditory hypersensitivity in a *Shank3* mouse model of ASD
Ana Carolina Pinto Castro
UMinho | 2022

Universidade do Minho
Escola de Medicina

Ana Carolina Pinto Castro

HCN channelopathy as a key mechanism for auditory hypersensitivity in a *Shank3* mouse model of ASD

Dissertação de Mestrado
Mestrado em Ciências da Saúde

Trabalho efetuado sob a orientação da
Professora Doutora Patrícia Monteiro
e do
Professor Doutor Luís Jacinto

outubro de 2022

AGRADECIMENTOS

Começo por agradecer à minha orientadora, Professora Patrícia Monteiro, que tão bem me acolheu desde o primeiro momento na sua equipa. Obrigada pelas oportunidades e pelos ensinamentos. Ao Professor Luís Jacinto, meu coorientador, por ter sido também um enorme apoio, especialmente na altura de arranjar soluções criativas para os problemas.

Sou grata também pelas minhas colegas de equipa. Agradeço à Margarida Falcão, à Patrícia Silva e à Alexandra Cruz, pessoas que me deram imensa força nesta jornada. Obrigada à Sara e ao Carlos V., companheiros de outras andanças, mas que permaneceram e permanecerão. Às novas amizades, que o ICVS me deu, Ricardo, Carlos e Inês. Deixo um agradecimento especial à Diana, que admiro muito e que tem uma paciência e dedicação inesgotáveis.

Agradeço à Bruna, à Daniela, à Ana Campos-Ríos e a todas essas cientistas de garra que, tal como todas as outras que já mencionei até agora, tiveram sempre uma palavra de força para me dar. É uma enorme honra partilhar ciência com mulheres assim. Aos colegas de equipa, colegas de mestrado, colegas de laboratório, estou grata por todas as interações porque todos vocês tiveram algo para me ensinar.

Finalmente, agradeço à minha família, aqueles que estiveram lá desde o início. À minha mãe, aos meus irmãos, à minha tia e aos meus queridos avós. Agradeço ainda ao João, por tornar os momentos felizes ainda mais brilhantes e os tristes mais suportáveis.

FUNDING

The work included in this dissertation was performed at the Life and Health Sciences Research Institute (ICVS), University of Minho. Financial support was provided by FCT project PTDC/MED-NEU/28073/2017 (POCI-01-307 0145-FEDER-028073); "La Caixa" banking foundation under grant agreement LCF/PR/HR21-00410; FEBS excellence award 2021; ICVS scientific microscopy platform, member of the national infrastructure PPBI - portuguese platform of bioimaging (PPBI-POCI-01-0145-FEDER-022122); and national funds through FCT- projects UIDB/50026/2020 and UIDP/50026/2020.

STATEMENT OF INTEGRITY

I hereby declare having conducted this academic work with integrity. I confirm that I have not used plagiarism or any form of undue use of information or falsification of results along the process leading to its elaboration.

I further declare that I have fully acknowledged the Code of Ethical Conduct of the University of Minho.

RESUMO

CANALOPATIA DE HCN COMO UM MECANISMO CHAVE PARA A HIPERSENSIBILIDADE AUDITIVA NUM MODELO ANIMAL DE SHANK3 PARA PEA

A perturbação do espetro do autismo (PEA) é uma perturbação do neurodesenvolvimento de etiologia desconhecida. Fatores de natureza ambiental e genética estão associados a um maior risco para PEA. Até à atualidade, mais de 100 genes foram identificados como genes de risco para PEA, estando associados à regulação da expressão genética e à maturação de linhas neuronais excitatórias e inibitórias. Entre eles, o gene *SHANK3* é dos mais estudados e está associado a cerca de 1-2% dos casos de PEA.

As características principais da PEA incluem dificuldades na comunicação e interação social, comportamentos repetitivos e hipo- ou hipersensibilidade a estímulos sensoriais. Uma das alterações sensoriais mais reportadas em PEA é a sensibilidade auditiva. Diversos modelos animais para PEA também apresentam em comum esta característica, nomeadamente o modelo de murganho *Shank3-InsG3680*$^{+/+}$ utilizado neste estudo. Neste trabalho, pretendeu-se clarificar potenciais mecanismos por detrás do fenótipo de hipersensibilidade auditiva observado no modelo de murganho *Shank3-Insg3680*$^{+/+}$.

O principal foco foi a região cerebral do córtex auditivo primário (A1), uma vez que esta é importante para o processamento auditivo. Através de uma análise de proteómica SWATH-MS em A1, identificámos o canal HCN1 (canal regulado por hiperpolarização e por ligação a nucleótido) como um dos mais sobre-expressos em murganhos *InsG3680*$^{+/+}$ machos adultos (6-10 semanas), mas não durante o desenvolvimento (1-5 semanas). Transcritos de HCN1 (*mHcn1*) estão também aumentados aos 21 dias de idade (P21) em murganhos *InsG3680*$^{+/+}$ machos. Foram também realizados registos intracelulares de correntes de hiperpolarização mediadas por HCN (I_h) por eletrofisiologia de *whole-cell patch clamp*. Os resultados indicam uma diminuição das correntes I_h especificamente em neurónios principais putativos em murganhos *InsG3680*$^{+/+}$, o que sugere uma perturbação funcional dos canais HCN em A1. Sabendo que a SHANK3 interage com HCN1 e é provavelmente responsável pela ancoragem de HCN1 na sinapse, propomos um mecanismo através do qual a falta de SHANK3 compromete a localização sub-celular de HCN1, causando redução na I_h. Como mecanismo de compensação, a célula aumenta os seus níveis de HCN1, tentando compensar os défices funcionais e levando a um fenótipo molecular de sobre-expressão de HCN1 em murganhos *InsG3680*$^{+/+}$ adultos.

Em suma, estes resultados contribuem para a melhor compreensão do funcionamento dos circuitos do córtex auditivo no modelo *InsG3680*$^{+/+}$ e sugerem HCN1 como um potencial alvo terapêutico em PEA.

Palavras-chave: Perturbação do Espetro do Autismo, Neurodesenvolvimento, Hipersensibilidade auditiva, *SHANK3*, Canal regulado por hiperpolarização e por ligação a nucleótido 1.

ABSTRACT

HCN CHANNELOPATHY AS A KEY MECHANISM FOR AUDITORY HYPERSENSITIVITY IN SHANK3 MOUSE MODEL OF ASD

Autism spectrum disorder (ASD) is a neurodevelopmental disorder with elusive etiology. There are environmental and genetic factors underlying an increased risk for ASD. So far, over 100 genes have already been identified as ASD-risk genes, most of them associated with gene expression regulation and maturation of excitatory and inhibitory neuronal lineages. Among them, the *SHANK3* human gene is one of the most studied and accounts for 1–2% of ASD cases.

The core features of ASD include social-communication impairments, restricted repetitive behaviors and hypo- or hyperreactivity to sensory stimuli. One of the most reported sensory-perceptual abnormalities in ASD is auditory sensitivity. Many rodent models of ASD also share auditory impairments, namely the *Shank3-InsG3680*$^{+/+}$ mouse model, which was used in this study. Our aim was to unveil potential mechanisms underlying the auditory hypersensitivity phenotype observed in the *Shank3-InsG3680*$^{+/+}$ mouse model of ASD.

We focused on the primary auditory cortex (A1) brain region since it is an important region for auditory processing. Using SWATH-MS proteomics screening in A1, we identified HCN1 as one of the most upregulated proteins in adult *InsG3680*$^{+/+}$ male mice (6-10 weeks), but not during development (1-5 weeks). HCN1 transcripts (*mHcn1*) were also found to be increased at postnatal day 21 (P21) in *InsG3680*$^{+/+}$ male mice. Intracellular recordings of HCN-mediated hyperpolarization currents (I_h) were also performed using whole-cell patch clamp electrophysiology. Results revealed a cell-type specific decrease of I_h in putative cortical principal neurons in *InsG3680*$^{+/+}$ mice, suggesting a functional impairment of HCN channels in A1 brain region. Knowing that SHANK3 interacts with HCN1 and it is likely required for anchoring HCN1 at the synapse, we propose a mechanism by which lack of SHANK3 disrupts HCN1 sub-cellular localization, compromising HCN1 function and causing a reduction in I_h. As a compensation mechanism, the cell increases HCN1 levels trying to compensate for the lack of function, leading to a molecular phenotype of HCN1 overexpression in adult *InsG3680*$^{+/+}$ mice.

Together these results contribute to our understanding of auditory cortex circuits in the *InsG3680*$^{+/+}$ model of ASD and reveal HCN1 as a potential therapeutic target in ASD.

Keywords: Autism Spectrum Disorder, Neurodevelopment, Auditory hypersensitivity, *SHANK3*, Hyperpolarization cyclic nucleotide-gated channel 1.

INDEX

ABBREVIATIONS

		A
A1	Primary auditory cortex	
AAF	Anterior auditory field	
ABR	Auditory brainstem response	
AC	Auditory cortex	
aCSF	Artificial cerebrospinal fluid	
ADCY	Adenylate cyclase	
AMPA	α-amino-3-hydroxy-5-methyl-4-isoxazolepropionic acid	
AN	Auditory nerve	
ANK	Ankyrin domain	
ASD	Autism Spectrum Disorder	
ASR	Acoustic startle response	
ATP	Adenosine triphosphate	**C**
cAMP	Cyclic adenosine monophosphate	
CB	Calbindin	
cDNA	Complementary DNA	
CF	Characteristic sound frequency	
CN	Cochlear nucleus	
CNIC	Central nucleus of the inferior colliculus	
CNTNAP2	Contactin-associated protein-like 2	
Cp	Capacitance	
CR	Calretinin	
C_T	Threshold cycle value	**D**
DCN	Dorsal cochlear nucleus	
DGAV	Direção Geral de Alimentação e Veterinária	
DMSO	Dimethyl sulfoxide	
DNA	Deoxyribonucleic Acid	
DNLL	Dorsal nucleus of the lateral lemniscus	
DSM-5	Diagnostic and Statistical Manual of Mental Disorders	**E**
E/I	Excitation/inhibition	
EDTA	Ethylenediamine tetra acetic acid	
ERP	Event related potentials	**F**
FDR	False discovery rate	
FM	Frequency modulated	
FMRP	Fragile X mental retardation protein	
FMS	Frequency modulated sweep	
FXS	Fragile X syndrome	**G**
G	Guanine nucleotide	
GABA	Gamma-aminobutyric acid	
GKAP	Guanylate kinase-associated protein	
GluA	Glutamate AMPA receptors	

GluR	Glutamate receptor	**H**
GMM	Gaussian Mixture Model	
GPCR	G-coupled protein receptor	
HCN	Hyperpolarization cyclic nucleotide-gated channel	
HEPES	N-(2-Hydroxyethyl)piperazine-N'-(2-ethanesulfonic acid)	
HRP	Horseradish peroxidase	**I**
IC	Inferior colliculus	
IDA	Information dependent acquisition	
IgG	Immunoglobulin G	
I_h	Hyperpolarization current	
InsG3680	Guanine insertion in gene *locus* 3680	
I_{ss}	Steady-state current	
I-V	Current/voltage curve	**K**
KO	Knockout	**L**
LC-MS	Liquid chromatography/Mass spectrometry	
LFP	Local field potential	
LL	Lateral lemniscus	
LLN	Lateral lemniscus nucleus	
LSO	Lateral superior olive	**M**
m/z	Mass-to-charge ratio	
MeCP2	Methyl-CpG binding protein	
MGB	Medial geniculate body	
MMP-9	Matrix metalloproteinase-9	
MNTB	Medial nucleus of the trapezoid body	
MSO	Medial superior olive	**N**
n.s.	Not significant	
N/A	Not applicable	
NGS	Normal Goat Serum	
NMDG	N-methyl-D-glucamine	
NR	Nicotinamide riboside	**P**
p	p-value	
PAF	Posterior auditory field	
PCR	Polymerase chain reaction	
PDZ	Postsynaptic density protein 95–discs large homologue 1–zonula occludens 1 domain	
pGluN	Phospho-NMDA receptor	
PMS	Phelan-McDermid Syndrome	
PNN	Perineuronal net	
PPI	Prepulse inhibition	
PRO	Proline-rich region	
PSD	Post-synaptic density complex	
PSD95	Postsynaptic density protein-95	

PTEN	Phosphatase and tensin homolog	
PV^+	Parvalbumin-positive	**R**
Ra	Access resistance	
Rin	Input resistance	
Rm	Membrane resistance	
RMP	Resting membrane potential	
RNA	Ribonucleic Acid	
RT	Room temperature	
RT-qPCR	Real-time quantitative polymerase chain reaction	**S**
SAM	Sterile alpha motif domain	
SAPAP	SAP90/PSD95associated protein	
SD	Standard deviation	
SDS	Sodium Dodecyl Sulfate	
SDS-PAGE	Sodium Dodecyl Sulfate Polyacrylamide Gel Electrophoresis	
SEM	Standard error of the mean	
SES	Startle eliciting stimulus	
SG	Silent gap	
SH3	SRC homology 3 domain superfamily	
SHANK	SH3 and multiple ankyrin repeat domains	
SOC	Superior olivary complex	
SWATH-MS	Sequential Windowed data independent Acquisition of the Total High-resolution Mass Spectra	
SynGap	Synaptic Ras GTPase-activating protein	**T**
TBE	Tris/Borate/EDTA buffer	
TBS	Tris-Buffered Saline	
TBST	Tris-Buffered Saline Tween	
TG	Transgenic	
TH^+	Tyrosine hydroxylase-positive	**U**
USV	Ultrasonic vocalization	**V**
$V_{0.5}$	Half-maximal activation voltage	
VAF	Ventral auditory field	
VB	Ventrobasal	
V_c	Voltage-clamp	
VCN	Ventral cochlear nucleus	
VPA	Valproic acid	**W**
WT	Wild type	
α7-nAChR	α7-nicotinic acetylcholine receptor	
Δex	Exon deletion	
ΔR_m	Membrane resistance change	
τ_{act}	I_h decay time constant	
τ_{memb}	Membrane time constant	

LIST OF FIGURES

LIST OF TABLES

1 INTRODUCTION

Parts of this introduction have been recently published by us in a peer-reviewed journal (Castro and Monteiro, 2022) (DOI: 10.3389/FNMOL.2022.845155).

1.1 Autism spectrum disorder (ASD): from symptoms to etiology

Autism Spectrum Disorder (ASD) is a neurodevelopmental disorder with different severity levels and poorly understood etiology. It is diagnosed up to 4 times more often in males than in females (Werling and Geschwind, 2013) and it is estimated to affect around 1 in 160 children worldwide (Elsabbagh et al., 2012). Current diagnosis criteria and core features are described in the Diagnostic and Statistical Manual of Mental Disorders (DSM-5; American Psychiatric Association, 2013) and include deficits in social communication and interaction, and repetitive restricted behaviors. Such deficits in social-emotional interaction range from maintaining a conversation to sharing interests or emotions with peers, deficits in non-verbal communication (e.g. the use and interpretation of body language and facial expressions), and difficulties in establishing and maintaining relationships. The repetitive restricted behaviors may include stereotyped motor movements, insistence on sameness and rigid patterns of behaviors and routines, strict interests towards objects or activities, and hyper- or hyposensitivity to sensory stimuli inputs from vision, audition, touch, smell and taste, or unusual interest in sensory aspects of the environment (American Psychiatric Association, 2013; Robertson and Baron-Cohen, 2017). Usually, symptoms start to arise during the second year of life, although this may change with the severity of the disorder. Typically, the first noticeable symptoms are delayed development of language and lack of social interest (American Psychiatric Association, 2013).

The etiology of ASD is not fully understood and is likely multifactorial. Earlier, it was though that ASD would arise mostly from environmental causes. Indeed, there are environmental risk factors that may disturb normal embryonic development and contribute to ASD, such as exposure to teratogens (certain drugs, pollutants or food contaminants), maternal infections, and even advanced parental age (Arndt et al., 2005; Herbert, 2010). Nonetheless, a growing body of evidence demonstrates that ASD has a strong genetic component (Rylaarsdam and Guemez-Gamboa, 2019). Studies in monozygotic and dizygotic twins indicate concordance rates of 60-90% and up to 10%, respectively, being the initial evidences of ASD as a genetic-linked disorder (Muhle et al., 2004). However, only around 5% of the cases are associated with syndromic forms of ASD, such as Rett syndrome, Fragile X syndrome, PTEN macroencephaly syndrome, tuberous sclerosis, among others. Even nowadays many of the diagnosed cases are still idiopathic forms of autism with unknown cause. Recent studies suggest that chromosomal

duplications/deletions and single nucleotide mutations in ASD-risk genes are probably behind ASD phenotypes (Sztainberg and Zoghbi, 2016). Considering all the evidence, it is clear that ASD stems from both environmental and genetic factors, having mono- and polygenic causes.

1.2 Genetic causes for ASD

One of the largest whole-exome sequencing studies to date used over 35,000 samples from neurotypical and ASD diagnosed individuals (Satterstrom et al., 2020). The authors identified 102 ASD-associated genes which they broadly group according to two main functions: regulation of gene expression and neuronal communication (Satterstrom et al., 2020). In accordance with the categorization of ASD as a neurodevelopmental disorder, indeed most of the candidate genes identified are expressed exactly during pre- and early post-natal development and display cortical enrichment in maturing excitatory and inhibitory neuronal lineages (Figure 1) (Satterstrom et al., 2020). Earlier this year, an analysis of *de novo* and inherited variants in ASD cases identified five new ASD-risk genes: *NAV3*, *ITSN1*, *MARK2*, *SCAF1* and *HNRNPUL2* (Zhou et al., 2022). Furthermore, the study showed that some of the most highly penetrant loss of function mutations, which may be either inherited or *de novo*, occur in well-known ASD-risk genes such as *SYNGAP1*, *ADNP*, *FOXP1*, *PTEN*, *POGZ*, *KDM5B*, *GIGYF1*, *CHD8*, *SCN2A* and *SHANK3* (Zhou et al., 2022).

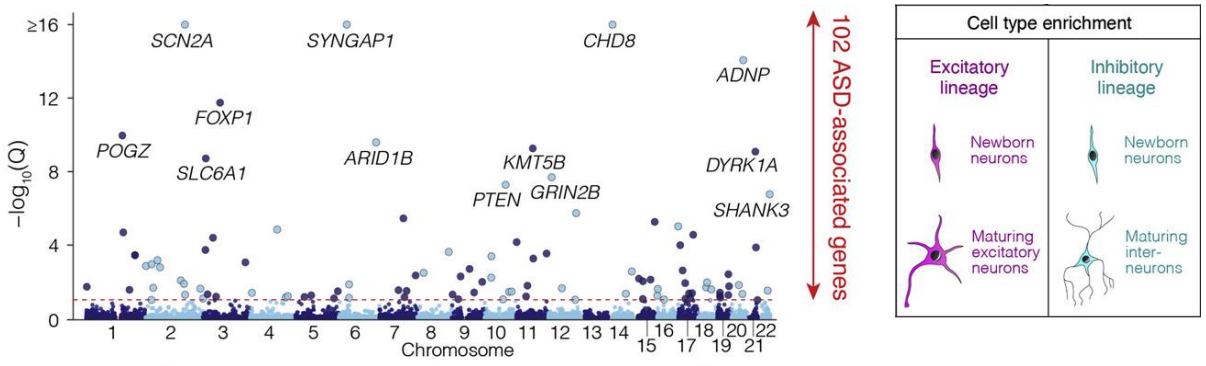

Figure 1. Large-scale exome sequencing study reveals 102 ASD-associated genes.

Left) Manhattan plot obtained from the analysis of over 35'584 samples collected from neurotypical controls and ASD patients shows 102 genes identified as ASD-risk genes (top candidate genes are labeled). The red dashed line represents the threshold for a false discovery rate (FDR) of 0.05%. Right) Most of the ASD-associated genes found in this study are enriched in excitatory and inhibitory lineages of both newborn and maturing neurons. Image modified from Satterstrom et al., 2020.

1.2.1 *SHANK3*: a major risk gene for ASD

Among all the ASD candidate genes, *SHANK3* is one of the most studied, being considered as a possible monogenic cause for ASD, with its variants explaining approximately 1% of ASD cases. Evidence from postmortem analysis of brains from individuals diagnosed with ASD indicates that around 15% present increased SHANK3 methylation, which may shift SHANK3 isoform expression pattern in the brain. The *SHANK3* gene was initially studied in the context of Phelan-McDermid Syndrome (PMS), a disorder belonging to the autistic spectrum and caused by a terminal deletion of chromosome 22, encompassing the 22q13.3 region where *SHANK3* is located. PMS main symptoms include neonatal hypotonia and delays in development and speech. In this context, *SHANK3* was implicated as the major genetic cause underlying the neurological symptoms in PMS (Wilson et al., 2003). Later on, *SHANK3* mutations were found in individuals diagnosed with ASD but without PMS. This provided evidence that *SHANK3*, by itself, is a determinant gene in ASD (Durand et al., 2007).

The SHANK3 protein belongs to a family of SHANK (SH3 and multiple ankyrin repeat domains) proteins which are scaffolding proteins located at excitatory synapses and responsible for orchestrating the organization of the post-synaptic density complex (PSD) (Monteiro and Feng, 2017) (Figure 2). Different SHANK proteins present shared domains, namely the ankyrin domain (ANK; located at the N terminus), the SRC homology 3 domain superfamily (SH3), the postsynaptic density protein 95–discs large homologue 1–zonula occludens 1 domain (PDZ), the proline-rich region (PRO domain) and the sterile alpha motif domain (SAM; located at the C terminus). These are all protein-protein interacting domains that determine the scaffolding function of SHANK proteins (Monteiro and Feng, 2017). Through these domains, SHANK proteins can interact with other proteins present at the PSD complex, such as the SAP90/PSD95-associated protein (SAPAP), the Homer and cortactin proteins (through the PRO domain), and the glutamate receptor 1 (GluR1) subunit of α-amino-3-hydroxy-5-methyl-4-isoxazolepropionic acid (AMPA) receptors (through the PDZ domain). These interactions are important for the formation and maintenance of dendritic spines, synaptic communication, plasticity and cytoskeleton dynamics (Monteiro and Feng, 2017).

Several studies have shown that *Shank3* mutations in zebrafish (Liu et al., 2018), mice (Mei et al., 2016; Zhou et al., 2016), rats (Song et al., 2019), and even primates (Zhou et al., 2019b), lead to reduced social interaction and repetitive behaviors, which are core ASD-like features (Peça et al., 2011; Zhou et al., 2016; Delling and Boeckers, 2021). But despite these behavioral phenotypes associated with *Shank3* mutations being conserved among different species, the mouse is still by far the most studied animal model.

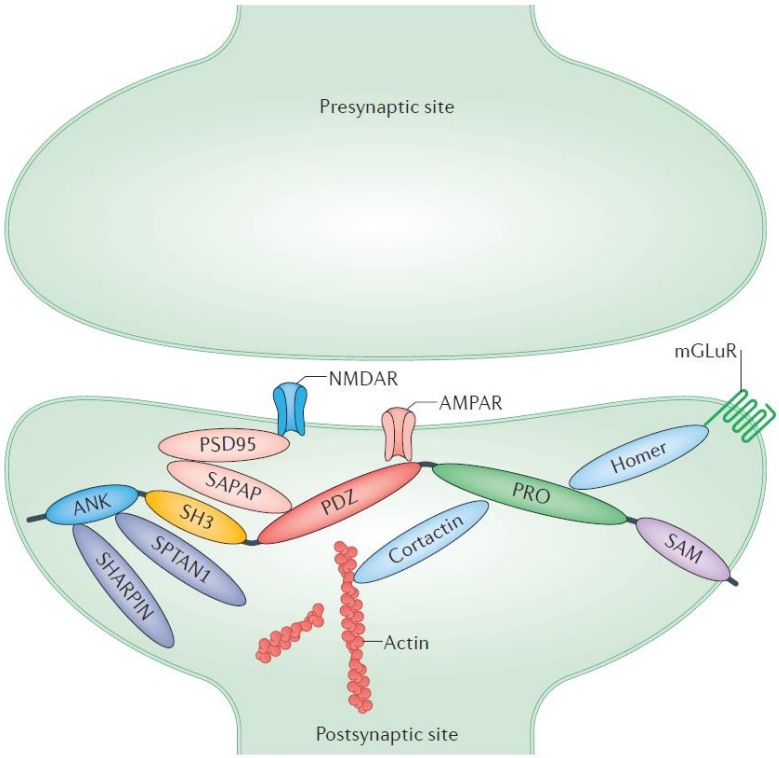

Figure 2. Schematic representation of SHANK protein and its main interactors at the post-synaptic density.

The SHANK protein (SH3 and multiple ankyrin repeat domains) tethers several other PSD proteins at excitatory post-synaptic sites through its multiple protein-protein interaction domains: 1) ankyrin repeat domain (ANK) - SHARPIN and SPTAN1 (spectrin alpha chain, non-erythrocytic 1) interact with the N-terminal of ANK; 2) PDZ domain (PSD protein 95 (PSD95)–discs large homologue 1-zonula occludens 1) - SHANK interacts with NMDA and AMPA receptors (NMDAR and AMPAR, respectively) through the PDZ domain. The interaction with NMDAR occurs indirectly through two other proteins: SAPAP (SAP90/PSD95-associated proteins) and PSD95. 3) PRO domain (proline rich) - SHANK protein establishes connections with the cytoskeleton (interacts with actin through cortactin) and with metabotropic glutamate receptors (mGluRs; interacts with mGluRs through homer) via PRO domain. Image adapted from Monteiro and Feng, 2017.

1.2.2 *Shank3* mouse models of ASD

Most *Shank3* transgenic mouse models of ASD generated so far present social impairments and repetitive behavior (essentially manifested through increased self-grooming behavior) (Table 1). The severity of such features can vary depending on the transgenic mouse line studied (e.g. repetitive grooming can range from a moderately increment in time spent grooming to self-inflicted skin lesions).

Regarding sensory alterations, these have not been typically studied in animal models until very recently, perhaps reflecting the recent alterations in DSM-5 classification where ASD criteria now includes sensory alterations. Nonetheless, alterations in acoustic thresholds (either as increased or decreased) have been reported, as well as olfactory deficits and hyposensitivity (Zhou et al., 2016; Drapeau et al., 2018). A more detailed overview can be seen in Table 1.

Table 1. Summarized characterization of *Shank3* mouse models.

Abbreviations: ANK (Ankyrin domain), Δex (exon deletion), GluR1 (Glutamate receptor 1), GKAP (guanylate kinase-associated protein), GluA (Glutamate AMPA receptor), NR (Nicotinamide riboside), PPI (Prepulse inhibition), SAPAP3 (SAP90/PSD95¬associated protein 3), PSD93 or PSD95 (Postsynaptic density protein 93 or 95), pGluN (phospho-NMDA receptor), SynGap (Synaptic Ras GTPase-activating protein), n.s. (not signifficant), N/A (Not applicable). Modified from (Monteiro and Feng, 2017).

Protein domains	Isoforms not disrupted	Altered synaptic proteins	Social behaviors	Repetitive behaviors	Sensorial alterations	Refs.
ANK repeat: Δex4-9[Buxbaum]	3 - 10	Decreased density of GluR1-immunoreactive puncta	Less sniffing in male-female interactions. Normal sociability in 3-chamber	Increased self-grooming	Hotplate: n.s.; Olfactory discrimination: n.s.	(Bozdagi et al., 2010; Yang et al., 2012)
ANK repeat: Δex4-9[Jiang]	3 - 10	Decreased GKAP, Homer1b/c, GluA1, NR2A	Abnormal social interaction; Normal social novelty	Increased self-grooming. Hole-board test: increased head pokes	PPI: n.s.; Olfactory discrimination: n.s.	(Wang et al., 2011)
ANK repeat: Δex4-7[Feng]	3 - 10	N/A	Normal social interaction; Abnormal social novelty	No increase in self-injurious grooming	N/A	(Peça et al., 2011)
PDZ domain: Δex13-16[Feng]	8,9,10	Reduced Homer1, SAPAP3, NR2, NR2B, GluA2, PSD93	Abnormal social interaction and abnormal social novelty in adults and juveniles	Self-injurious grooming, causing skin lesions	N/A	(Peça et al., 2011; Dhamne et al., 2017; Balaan et al., 2019)
SH3 domain: Δex11[Boeckers]	6 - 10	Increased NR2B and Shank2; Reduced Homer1b/c, mGluR5	Abnormal social interaction; Abnormal social novelty	Self-injurious grooming, causing skin lesions	Hotplate: hyposensitivity	(Schmeisser et al., 2012; Vicidomini et al., 2017)
ANK repeat: Δex9[Kim]	3 - 10	Decreased pGluN2B Tyr1472	Inconclusive testing (even WT mice did not show preference for social target)	Grooming: n.s.	N/A	(Lee et al., 2015)

Pro domain: InsG3680-ex21[Feng]	2,5,10	Reduced Homer, SAPAP3, SynGap, NR1, NR2A, NR2B, GluR2, mGluR5	Abnormal social interaction; Abnormal social novelty	Self-injurious grooming, causing skin lesions	PPI: mildly impaired; Acoustic startle response: impaired.	(Zhou et al., 2016)
Pro domain: R1117X-ex21[Feng]	2,5,10	Reduced Homer, PSD95, SynGap, NR1, NR2B, trend of reduced GluR2 and SAPAP3	Abnormal social interaction; Abnormal social novelty	Allogrooming present in heterozygous mice only	PPI: mildly impaired; Acoustic startle response: impaired	(Zhou et al., 2016)
ANK repeat: Δex4-9[Powell]	3 - 10	Decreased GluA2, GluA3, Homer1 b/c, and PSD95	Mildly impaired	Increased self-grooming	PPI: n.s.	(Jaramillo et al., 2016)
PDZ domain: FLEx-Δex13-16[Feng]	8,9 10	Reduced Homer, SAPA3, NR2A, NR2B, GluA2	Abnormal social interaction; Social novelty: N/A	Self-injurious grooming causing skin lesions	N/A	(Mei et al., 2016)
All domains: Δex4-22[Jiang]	All disrupted	Reduced PanSAPAP, SAPAP3, and Homer1b/c	Normal social interaction and normal social novelty	Self-injurious grooming, causing skin lesions	PPI: impaired startle; Olfactory discrimination: n.s.	(Wang et al., 2016)
PDZ domain: Δex13-19	10	Reduced Homer-1 b/c and PSD95	Abnormal social interaction and social novelty	Increased self-grooming	PPI and startle response: n.s.	(Jaramillo et al., 2017)
All domains: Δex4-22[Buxbaum]	All disrupted	N/A	Increased latency for first male-female interaction, normal social novelty.	Increased self-grooming	Cornea reflex, toe pinch retraction, pinna reflex, tail flick: n.s.; Preyer reflex: n.s., Startle response decreased, PPI: n.s.; Visual placing: n.s.; buried food test (olfactory): impaired	(Drapeau et al., 2018)

1.3 Sensory processing in ASD: the auditory pathway

Sensory-perceptual abnormalities are present in approximately 90% of individuals with ASD (Leekam et al., 2007; Tomchek and Dunn, 2007; Crane et al., 2009), being auditory hypersensitivity the most common sensory-perceptual abnormality (Gomes et al., 2008). By perceiving auditory inputs as noxious or unpleasant, patients may instinctively learn to avoid them (Marco et al., 2011), which could potentially be the root for the communication, socialization and learning impairments observed in ASD.

Upon an auditory stimulus, the nervous impulse travels through the auditory nerve (AN) until a relay center in the brainstem, the cochlear nucleus (CN), which is mainly divided in dorsal (DCN) and ventral (VCN) regions. The superior olivary complex (SOC) receives input from the CN and has three nuclei involved in auditory input processing: the lateral superior olive (LSO), the medial superior olive (MSO) and the medial nucleus of the trapezoid body (MNTB). The SOC then projects to the inferior colliculus (IC) through the fibers of the lateral lemniscus (LL), synapsing in the LL nucleus (LLN). From the IC,

information travels to the medial geniculate body (MGB), which lies in the thalamus and is the last auditory center before reaching the auditory cortex (AC), conveying information from several regions of the auditory system (Figure 3) (Malmierca, 2003; Knipper et al., 2013; Di Bonito and Studer, 2017).

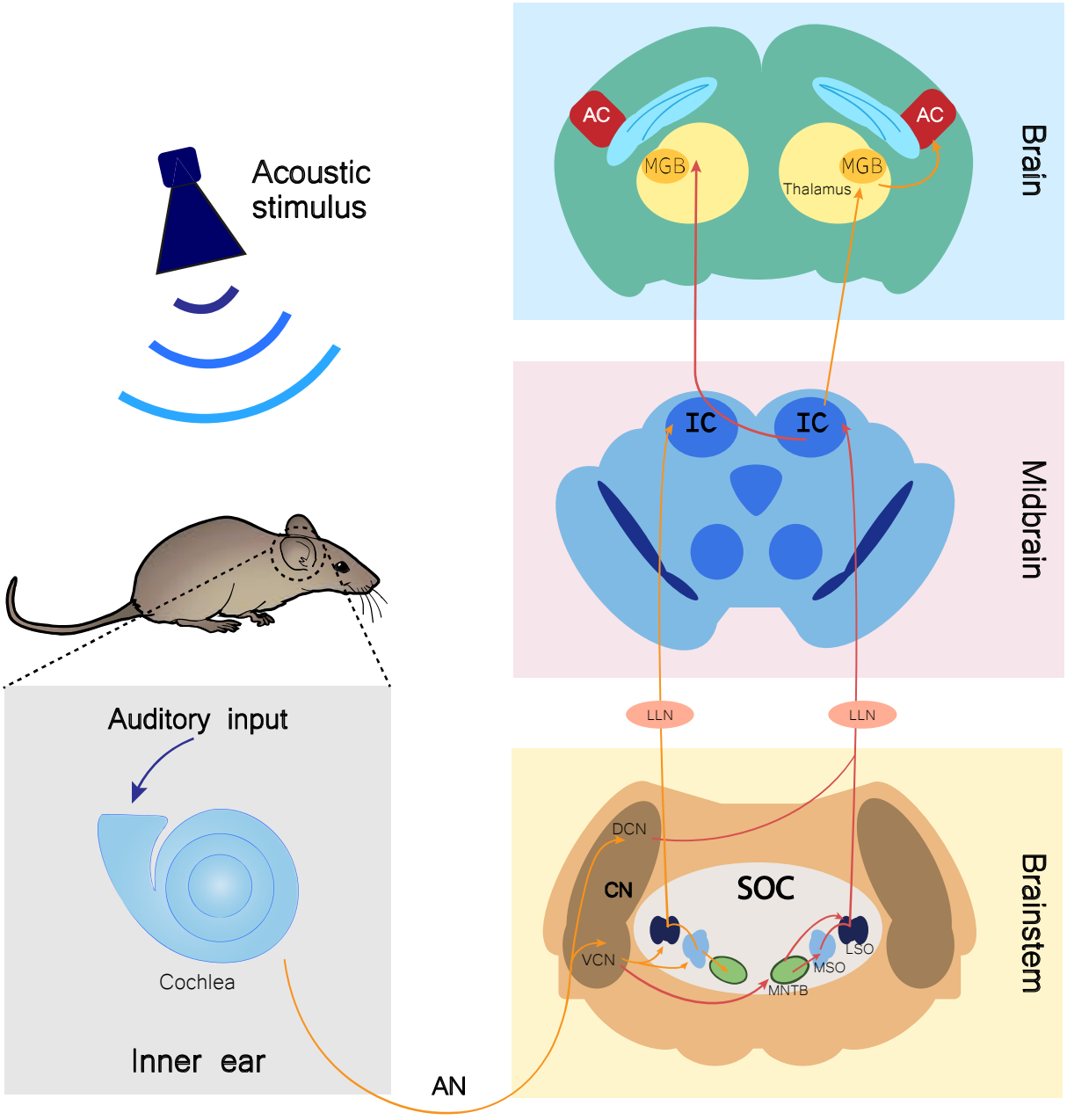

Figure 3. Monoaural ascending auditory pathway.

Auditory input arriving to the cochlea is transmitted through the auditory nerve (AN) to the cochlear nucleus (CN) in the brainstem. In this nucleus, AN bifurcates to the ventral cochlear nucleus (VCN) and the dorsal cochlear nucleus (DCN). Information is directed to the ipsilateral (orange arrows) and contralateral (red arrows) SOC (superior olivary complex), travelling through several of its nuclei, namely the lateral superior olive (LSO), medial superior olive (MSO) and medial nucleus of the trapezoid body

(MNTB). Both contralateral and ipsilateral input from the brainstem reach the inferior colliculus (IC) in the midbrain through fibers of the lateral lemniscus (LL), synapsing in the LL nucleus (LLN). From the IC, fibers project ipsilaterally and contralaterally to the medial geniculate body (MGB). The MGB is located in the thalamus and is the brain region that precedes the auditory cortex (AC) in the information flow of ascending auditory pathway. Image adapted from Castro and Monteiro, 2022.

1.4 Excitation and inhibition in primary auditory cortex circuits

The primary auditory cortex (A1) is the final stop of the ascending auditory pathway. By receiving and filtering subcortical inputs, the A1 region conveys a cortical representation of the sensory information. Here, sensory inputs are processed by an intricate but highly efficient network of excitatory and inhibitory connections that are perfectly shaped and tightly pruned during development (Sanes and Kotak, 2011). The primary auditory cortex (A1), like the rest of the neocortex, is organized in cortical layers, typically 6 in the rodent brain ($L_{1\text{-}6}$, Figure 4). The balance between excitation and inhibition in sensory regions is an important mechanism that allows the definition of fine receptive fields and ensures temporal precision of the cortical output. This excitation/inhibition (E/I) balance can vary with the cortical layer and is important to filter relevant information within each neuronal circuit (D'Souza and Burkhalter, 2017).

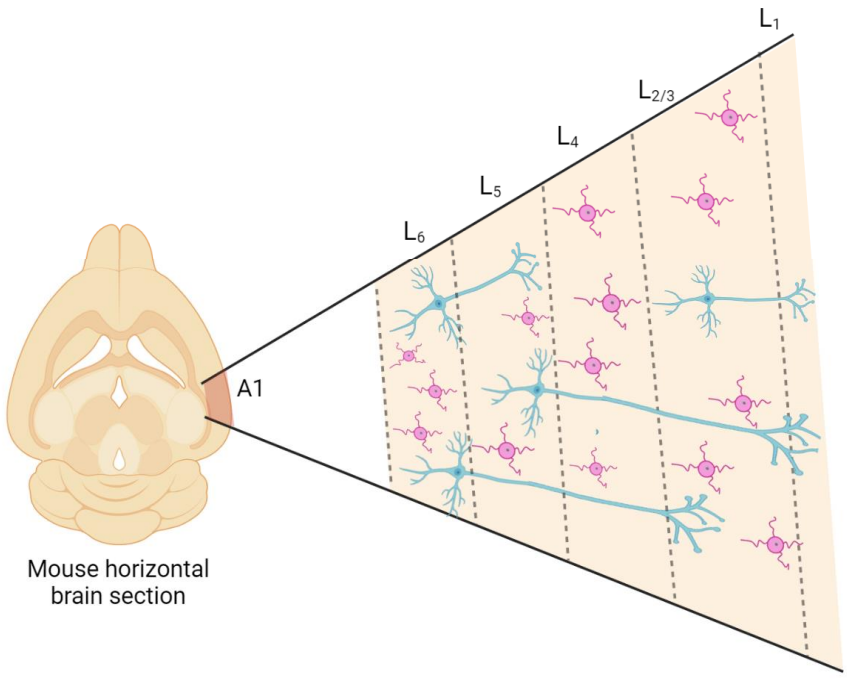

Figure 4. Representation of the layered organization of the primary auditory cortex (A1). Representation of a horizontal section of the mouse brain with the primary auditory cortex (A1) region

highlighted. In a zoom-in of the A1, it is visible the layered organization of this region, which is typically divided into 6 layers (L_{1-6}). The principal neurons are represented in blue and are typically pyramidal neurons whose dendrites may span from L_5 until as far as L_1. In pink are represented the local GABAergic interneurons, responsible for modulating the activity of principal cells and other interneurons. Created with Biorender.com.

Such excitation/inhibition interplay is supported by two major cellular populations: cortical excitatory neurons (mainly pyramidal cells) that receive and provide sensory input, and inhibitory cells (mainly GABAergic local interneurons) that modulate the activity of pyramidal cells by releasing gamma-aminobutyric acid (GABA) (DeFelipe et al., 2002). These cells are organized in a fine microcircuit where the pyramidal cells present input-output connections with either other brain regions or other cortical neurons (DeFelipe et al., 2002). Not only the direct inhibitory effect of interneurons on pyramidal neurons regulates their activity, but also the inhibitory effect of interneurons over other interneurons has also a disinhibitory effect over pyramidal cells (D'Souza and Burkhalter, 2017). But besides this circuit-level regulation, the intrinsic excitability of each neuron also defines the way it will respond to inputs (Chen et al., 2022), being also an important mechanism to maintain E/I balance.

The main determinants for intrinsic neuronal excitability are ionic channels. They may be classified according to their gating: voltage or ligand gated channels, or by the cations they allow to flow: Na^+, K^+, Ca^{2+} or Cl^-. The channel composition of a cell determines its intrinsic properties such as resting membrane potential and input resistance, which closely relate to its excitability. Briefly, when the depolarizing signal (the action potential) reaches an axon terminal, voltage-sensing Ca^{2+} channels open and the Ca^{2+} intake leads to neurotransmitters release. These neurotransmitters then bind to their respective receptors on the post-synaptic neuron, causing the opening of ligand-gated ionic channels that will allow the inward flow of cations and the depolarization of the post-synaptic neuron. The magnitude of this process depends on the frequency by which action potentials arrive to the synapse but also on the channel composition of the synapse. The depolarization signal of the post-synaptic membrane travels to the soma of the neuron in the form of a graded potential. This means that, depending on timing and frequency by which other graded potentials reach the soma, even a small membrane depolarization may sum and allow the generation of another action potential in a phenomenon called dendritic integration (Stanfield, 2013). In this process, the presence of other voltage-gated channels such as the hyperpolarization cyclic nucleotide-gated channels (HCNs) is determinant. These are channels activated upon hyperpolarizing voltages and are organized in a gradient throughout the dendrites of L5 pyramidal neurons. The great density of HCN

at distal sites of the dendrites has a dampening effect on the excitatory input and enables a more efficient temporal and spatial summation (Wahl-Schott and Biel, 2009).

Several studies have suggested impaired E/I balanced and altered cortical hyperexcitability in ASD (Sohal and Rubenstein, 2019). But despite recent evidence linking GABAergic defects and E/I imbalance to multisensory integration deficits in some mouse models of ASD (Gogolla et al., 2014), very little is known regarding their A1 circuits.

1.5 Auditory dysfunction in rodent models of ASD

It is well described that auditory hypersensitivity is one of the core features of ASD in humans, being now included in the diagnosis criteria. As in repetitive behaviors and social deficits, abnormal sensory perception is also identifiable in rodent models currently used to study ASD. Specifically, auditory abnormalities are found across ASD models despite the underlying mechanism not completely overlapping.

Given the broad etiology of ASD, many animal models have been developed to uncover ASD's molecular underpinnings. These models are based in genetic and non-genetic factors associated with increased risk for autism (Table 2). Other models not specifically conceived to study ASD display some ASD-like behaviors and may be useful for clarifying potentially shared mechanisms. We will further summarize the current knowledge regarding auditory alterations that have been found through multiple experimental approaches (Figure 5), as well as physiological, anatomical, and functional alterations identified in several rodent models of ASD.

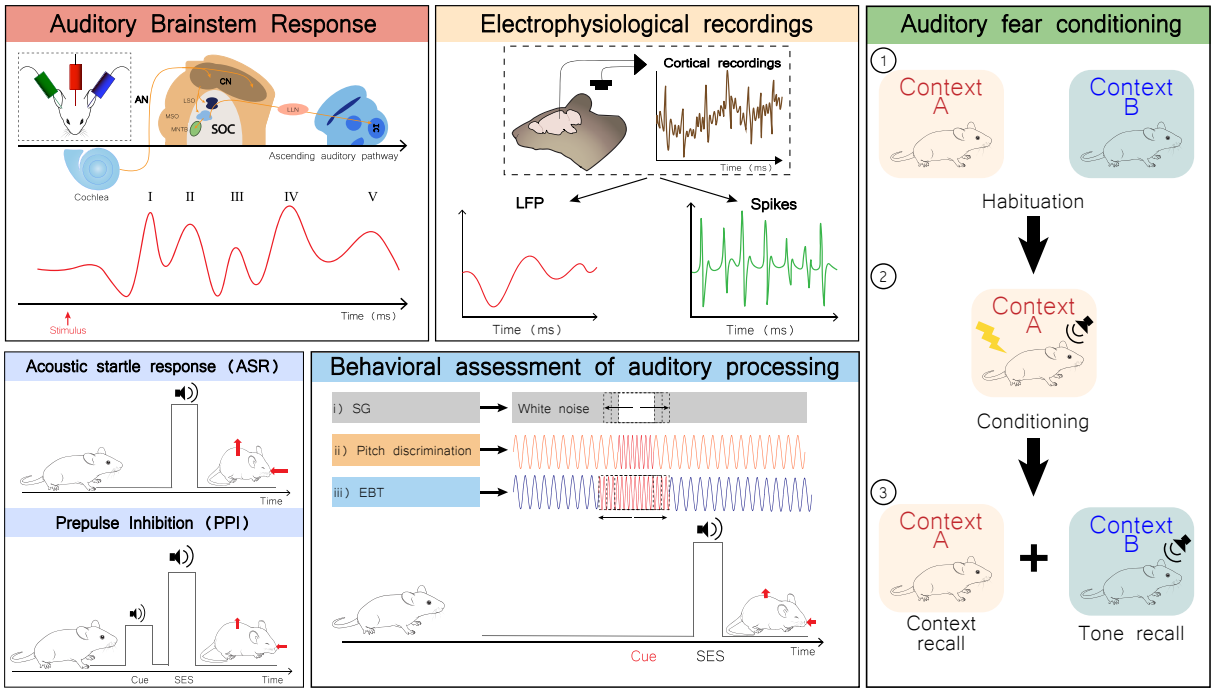

Figure 5. Examples of some experimental approaches to study auditory alterations in rodents.

Auditory brainstem response (ABR): Schematic representation of electrodes placement for ABR recording (inset; top left). Representation of the auditory pathway and corresponding ABR waves generated upon sound stimulation. Measuring ABR is a non-invasive method to assess the sum of evoked potentials that occur in the first milliseconds after sound stimulation across the auditory system. Wave I is generated by signal propagation through the auditory nerve (AN), wave II through the cochlear nuclei (CN), wave III through the superior olivary complex (SOC), wave IV through the lateral lemniscus (LL) and wave V through the inferior colliculus (IC). LSO: lateral superior olive, MSO: medial superior olive; MNTB: medial nucleus of the trapezoid body. Electrophysiological recordings: Local field potentials (LFP) and spiking activity can be obtained from in vivo electrophysiological recordings in the auditory cortex. LFPs represent the summed activity of a certain population of neurons that is recorded in a specific region, while spiking refers to a single neuron activity. Acoustic startle response (ASR) and prepulse inhibition (PPI): The ASR is a short-latency response to a startle eliciting stimulus (SES), considered a defensive reaction to a strong and sudden stimulus that prepares the individual to face a potential threat. It is characterized by a rapid contraction of facial and skeletal muscles (red arrows). This response is preserved across mammalian species, involving the brainstem, and the auditory and vestibular systems. The PPI test evaluates the attenuation of the ASR by presentation of a non-startling stimulus immediately preceding the SES. This enables to quantitatively assess the sensory-motor gating function, and the ability to effectively filter

sensory information, hence preventing sensory overload. Behavioral assessment of auditory processing: representation of behavioral paradigms to measure the ASR attenuation by a previously presented auditory cue. While in PPI test the type of stimulus used as cue is the same as in the SES, this set of behavioral tests takes advantage of other types of auditory cues for ASR inhibition. Adequately processing these auditory cues underlies an effective ASR inhibition, which in turn becomes a measure for auditory discrimination of different types of auditory cues. i) The subject is exposed to a white-noise background and a silence gap of variable duration in the background noise is used as cue for the upcoming SES; ii) and iii) The subject is exposed to a background pure tone. The cue preceding the SES is a momentaneous change in frequency. In ii) the duration of the cue is constant, but the frequency varies between trials and in iii) the duration of the cue is variable, but its frequency is the same across trials. Fear conditioning paradigm: 1) Subjects are habituated to contexts A and B; 2) Subjects are conditioned in context A by pairing a tone with shock; 3) Context and tone recall are performed 24h later. Freezing behavior is evaluated and compared across the whole test. Although the central role of the amygdala in the process of fear conditioning is well accepted, this is not the only critical player in this process. The auditory thalamus is increasingly considered as an important sensory integration center in the network involved in fear conditioning. Hence, this paradigm may also provide valuable information regarding auditory processing. Image adapted from Castro and Monteiro, 2022.

1.5.1 Auditory processing deficits in non-genetic models of ASD

Some of the most relevant environmental risk factors for ASD are: parental age, maternal nutrition, diseases, and infections; fetal exposure to teratogenic drugs, alcohol or other toxic compounds; and complications during delivery (e.g., perinatal hypoxia) (Burd et al., 1999; Masini et al., 2020). Prenatal exposure to the antiemetic drug thalidomide, the anticonvulsant drug valproic acid (VPA), and the antidepressant drug citalopram, affect neurodevelopment and behavior (Arndt et al., 2005; Maciag et al., 2006). Among these teratogenic drugs, valproic acid and thalidomide have been linked to the risk of autism in epidemiological studies (Matsuzaki et al., 2012). Auditory processing deficits in rodents exposed to these two drugs are thus summarized below.

1.5.1.1 Valproic acid

Rodents exposed to VPA *in utero* are perhaps the most studied environmental model of ASD, displaying impaired social interaction, abnormal sensory reactivity, anxiety-like and repetitive behaviors (Gandal et al., 2010; Engineer et al., 2014a; Nagode et al., 2017).

VPA-exposed mice show delayed ear opening (Zimmerman et al., 2018) and reduced ultrasonic vocalizations (USVs), both in early-life stages (decreased pup distress calls) and after sexual maturation (pre-mating vocalization) (Gandal et al., 2010). Their acoustic startle response (ASR) is normal but prepulse inhibition (PPI) is decreased, indicating impairments in sensory motor gating without hypo- or hyperreactivity to sound (Gandal et al., 2010).

Their primary and non-primary regions of the AC show alterations according to stimulus type (speech sound, noise burst or pure tone) (Engineer et al., 2014a; Anomal et al., 2015). Weaker local field potentials (LFPs) in the anterior auditory field (AAF), but stronger in the A1, are evoked by speech sounds. In response to pure tones, AAF presents the weakest, most delayed responses. Temporal and spectral processing is mainly impaired in the AAF, and this area seems to be the most affected regardless of stimulus type (Engineer et al., 2014a). Regarding A1, VPA-exposed rats exhibit a disorganized tonotopic map with overrepresented higher frequencies and receptive fields less accurately tuned to characteristic sound frequencies (CFs). Onset latency for neuronal firing in response to tones is decreased in A1 of VPA-exposed rats (Anomal et al., 2015). Although it has been suggested that a shorter inhibition in post-stimulus suppression may underlie these impairments (Engineer et al., 2014a), it is perhaps worth mentioning that number and density of parvalbumin-positive (PV^+) neurons in A1 is not changed (Anomal et al., 2015).

Observations from ASD patients and VPA-exposed rodents both indicate hypoplasia and dysmorphology of the brainstem (Dubiel and Kulesza, 2016). After pure tone sound exposure, c-Fos immunolabeling of the brainstem auditory centers suggests a generalized overactivation (Dubiel and Kulesza, 2016). In the CN and MNTB of VPA-exposed animals it is noticeable an overactivation together with tonotopical disruption (neuronal activation is observed beyond its normal tonotopic bands) (Dubiel and Kulesza, 2016). Additionally, VPA exposure leads to the development of fewer, smaller, and irregularly shaped neurons across the entire SOC (Lukose et al., 2011; Zimmerman et al., 2018, 2020). This happens at the level of several nuclei of the auditory brainstem (CN, SOC, LLN) with special impact on MNTB (Dubiel and Kulesza, 2016; Zimmerman et al., 2018).

Prenatal VPA exposure also seems to induce deficits in the expression of calbindin (CB) in principal neurons and octopus cells of the MNTB, as well as deficits in the expression of calretinin (CR) in the

globular bushy cells of the VCN (Zimmerman et al., 2018). This may destabilize calcium signaling on those cells, leading to problems in sound localization and temporal coding (Zimmerman et al., 2018).

VPA-induced alterations in the brainstem seem to arise from developmental differences in synaptic maturation with decreased inhibition (GABAergic signaling) or increased excitation (glutamatergic signaling). Other possibility is an excitatory hyperconnectivity promoted by abnormal axonal projections (Dubiel and Kulesza, 2016; Zimmerman et al., 2018). Interestingly, VPA exposure seems to increase postsynaptic glutamatergic excitatory connections between cortical plate and subplate (L5/6 and L4) by the second postnatal week (Nagode et al., 2017). By the same period, there is an increase in GABAergic inhibitory connections to subplate neurons. Although such concomitant increase in excitatory and inhibitory connections could in principle reflect a preservation effect of the E/I balance, the effect of VPA over inhibition seems to be greater than over excitation, affecting final E/I balance in the developing A1 (Nagode et al., 2017).

Lastly, VPA model presents reduced proportion of neurons sending ascending projections from NLL, SOC and CN to the central nucleus of the IC (CNIC). This impacts connectivity between brainstem and midbrain, hence, sound processing in the midbrain (Zimmerman et al., 2020), which seems to be particularly susceptible to VPA damage. The CNIC and NLL present reduced size, reduced neuronal density, and abnormal neuronal morphology. A reduction in CB^+ neurons was also reported in the dorsal nucleus of the LL (DNLL) and reduced dopaminergic input to the CNIC can be assumed based on reduced TH^+ (tyrosine hydroxylase positive) labeling in this region (Mansour et al., 2019). The CNIC projects to the MGB, that is also affected in VPA model, presenting fewer and smaller neurons and receiving less input from the midbrain and brainstem (Mansour et al., 2021).

1.5.1.2 Thalidomide

Many of the findings from the VPA model are also true for the thalidomide model, although fewer studies are available and focus essentially on MNTB alterations. MNTB is reported to be functionally impaired and diminished in size, with decreased projecting neuronal fibers, and increased c-Fos expression (expanded responsive area), upon tone stimulation (Ida-Eto et al., 2017; Tsugiyama et al., 2020). In line with the VPA model, decreased levels of CB expression are apparent in the SOC of thalidomide model (Tsugiyama et al., 2020).

1.5.2 Auditory processing deficits in monogenic models of ASD

Despite the apparently diverse genomic landscape behind ASD (Betancur, 2011), convergent molecular functions have been found for many ASD-candidate genes. Animal models are crucial tools to uncover such findings and besides gene function, important work has been carried out regarding auditory deficits.

1.5.2.1 Fmr1 knockout

Mutations in the *FMR1* gene are responsible for fragile X syndrome (FXS) and contribute to 8% of ASD cases (Zhang et al., 2019). The *FMR1* gene encodes the fragile X mental retardation protein (FMRP), which is an RNA-interacting protein that shuttles RNA from the nucleus to neuronal dendrites. FMRP seems to be a key player in dendritic spine formation (Braun and Segal, 2000), contributing to excitatory synapses and brain plasticity (Bassell and Warren, 2008; Sethna et al., 2014). *Fmr1* knockout (*Fmr1*-KO) animals are used as FXS models and typically display hyperactivity and learning deficits (The Dutch-Belgian Fragile X Consorthium et al., 1994).

When exposed to high intensity sounds, *Fmr1*-KO mice present increased tendency to audiogenic seizures that increases with age (Chen and Toth, 2001). According to the same study, these mice also present lower ASR and more efficient PPI. However, ASR was tested for one sound intensity only (no startle response curve reported), hence information on ASR threshold is absent and could potentially be an indicator of auditory sensitivity (Chen and Toth, 2001).

Regarding auditory fear conditioning, *Fmr1*-KO mice show lower freezing response to conditioned-unconditioned paired stimulus and to tone recalling (Reinhard et al., 2019). Such reduced freezing does not seem to be due to genotype-associated differences in locomotion but rather due to sound processing impairments in the KO (Reinhard et al., 2019). Reinforcing this, it was observed that *Fmr1*-KO rats present temporal integration of sound stimulus impaired but enhanced spectral integration. Since they present faster reaction times in response to a wider range of sound intensities, there is evidence of sound hyperacusis (Auerbach et al., 2021)**.** Lack of FMRP does not affect the ability to discriminate phonemes, suggesting that speech sound discrimination is likely normal (Engineer et al., 2014b).

Further evidence for the presence of auditory deficits in the *Fmr1* model has been obtained from electrophysiological studies where functional cortical impairments have been found (Rotschafer and Razak, 2013; Engineer et al., 2014b). KO cortical neurons show normal intensity threshold but enhanced response magnitude to tones, as well as broader frequency tuning. Such enhanced magnitude might arise from an inability to shut down neuronal activity during sound exposure (Rotschafer and Razak,

2013). When KO mice are exposed to trains of noise, the obtained responses differ between the first and subsequent stimulus. Initially, weaker responses are recorded at the AAF and ventral auditory field (VAF), but after several trains of noise, VAF presents weaker response, and the posterior auditory field (PAF) becomes stronger. The overall most affected area seems to be VAF (Engineer et al., 2014b). *Fmr1*-KO also present less selectivity to frequency modulated (FM) sweep rates and higher response to fast sweep rates, without differences regarding direction selectivity (up- or downward sweeps) (Rotschafer and Razak, 2013). Regarding AC response to speech sounds, evoked LFPs display lower peak amplitudes (N1, P2, N2 and P3 components) in *Fmr1*-KO. When splitting AC data into four fields (AAF, A1, VAF, and PAF), A1 and VAF show the weakest amplitudes for all components (Engineer et al., 2014b). Furthermore, onset latency in PAF and VAF is increased but temporal precision and strength to speech sounds are reduced (Engineer et al., 2014b).

Fmr1-KO mice are reported to have higher ABR thresholds for click sounds and pure tone frequencies, and reduced peak I and III amplitudes, suggesting defects in AN and brainstem. Response latency to sound stimulation and inter-peak latency are not altered (Rotschafer et al., 2015).

Histological assessments in the auditory brainstem of adult *Fmr1*-KO mice further reveal that neuronal cell size is reduced in VCN, MSO and MNTB (not in LSO) (Rotschafer et al., 2015; Ruby et al., 2015). Interestingly, although several cellular defects can be detected since birth at MNTB, these only emerge at VCN after hearing onset (Ruby et al., 2015; Rotschafer and Cramer, 2017). Of note, FMRP is expressed across the auditory brainstem in a specific pattern. In MNTB it has a tonotopical expression similar to potassium channel Kv3.1b, a channel that seems crucial for normal sound processing specifically in the binaural sound localization circuit (Strumbos et al., 2010; Ruby et al., 2015). In *Fmr1*-KO, however, the typical expression pattern of Kv3.1b in MNTB is not observed, namely its tonotopical gradient or increased expression upon sound stimulation (Strumbos et al., 2010; Ruby et al., 2015). Additionally, *Fmr1*-KO mice present reduced axonal profiles and CB immunoreactive terminals in MNTB somata which may indicate abnormal Ca^{2+} signaling regulation (Ruby et al., 2015).

Focusing on two important auditory nuclei of the SOC (MNTB and LSO), one study found a greater strengthening of excitatory input from the VCN to the LSO in *Fmr1*-KO, likely due to an increased number of synaptic connections (Garcia-Pino et al., 2017). Besides receiving excitatory input from the VCN, the LSO receives inhibitory input from the MNTB, which seems unaffected in *Fmr1*-KO mice. Therefore, the net effect is a potential increase in excitation. Such changes in E/I balance could explain the increased firing rates and broadened tuning curves observed in the LSO of *Fmr1*-KO mice and might contribute to their reported acoustic hypersensitivity (Garcia-Pino et al., 2017).

Auditory stimulation with tone bursts and amplitude-modulated tones leads to increased activation of IC in *Fmr1*-KO mice, especially in neurons that respond to lower frequencies (<20kHz). Broader tuning frequency is generally observed in individual neurons (Nguyen et al., 2020). Although the development of connections within the auditory circuitry seems to occur normally in *Fmr1*-KO, sound-driven refinements of excitatory inputs seem affected by the time of hearing onset (~P10-P11) (Nguyen et al., 2020). Because these refinements depend on precisely timed inhibitory inputs, it is thought that impairments in GABAergic signaling may cause E/I defects in IC. Of note, neurons in the dorsal region of the IC present a CF <20kHz, being the most responsive in *Fmr1*-KO and more hypersensitive. Given the prominent role of GABA in the dorsal region of the IC, it seems that GABAergic dysfunction may underlie abnormal responsiveness in this area (Nguyen et al., 2020).

In a broader picture, there is evidence consistent with both an increase in excitation mediated by strengthening of excitatory inputs and decrease in inhibition due to impairments on GABA-related neurotransmission. Thus, the E/I imbalance often described as a hallmark of ASD seems to hold true in the *Fmr1*-KO model. At the molecular level, one of the possible candidates underlying this imbalance and contributing to auditory hypersensitivity in *Fmr1*-KO is matrix metalloproteinase-9 (MMP-9). This enzyme is upregulated in the AC of *Fmr1*-KO mice and has been associated with its reduced ERP habituation (event related potentials) (Lovelace et al., 2016, 2018, 2020b). Furthermore, MMP-9 upregulation likely hinders the formation of perineuronal nets (PNNs) around PV^+ cortical interneurons (GABAergic neurons), leading to reduced cortical network inhibition and E/I imbalance in the AC (Wen et al., 2018). Genetic or pharmacological strategies for reducing MMP-9 levels seem to rescue the following phenotypes: 1) audiogenic seizure susceptibility, 2) AC activity (spontaneous and evoked), 3) auditory ERP habituation, 4) formation of PNNs around PV^+ cells, 5) anxiety-like and hyperactive behaviors, 6) ASR (Gkogkas et al., 2014; Lovelace et al., 2016, 2020a; Wen et al., 2018; Kokash et al., 2019; Pirbhoy et al., 2020). Enhancement of endocannabinoid production (2-arachidonoyl-sn-glycerol) seems to ameliorate synchrony in the cortical response to auditory stimuli, and rescue anxiety-like and hyperactive behaviors (Pirbhoy et al., 2021). Inhibiting phosphodiesterase 10A seems an additional therapeutic approach since it was shown to improve auditory processing in *Fmr1*-KO mice (Jonak et al., 2021). Interestingly, sound exposure during postnatal development seems to rescue/normalize ERP, PV^+ cell density and dendritic spine density in the AC (Kulinich et al., 2020).

1.5.2.2 *α7-nAChR knockout*

CHRNA7 is a gene encoding for α7-nicotinic acetylcholine receptor (α7-nAChR), an homopentameric transmembranar protein highly expressed in the brain (Schaaf, 2014). α7-nAChR expression starts during prenatal development and peaks during the first synaptogenesis events. Changes in channel expression negatively influence neurogenesis, synaptogenesis and neuroblasts' migratory events (De Jaco et al., 2016). In humans, microduplications in this gene are associated with a wide range of neurobehavioral disorders, including ASD (Dennis et al., 2012).

In rodents, α7-nAChR loss is associated with developmental impairments that affect auditory processing. ABR hearing thresholds and peak amplitudes are unaffected, but peak IV latency is increased, suggestive of impairments in the midbrain. Accordingly, single unit responses recorded in the IC revealed that KO animals have a subset of neurons with an atypical response to pure tones, presenting also deficits in spike timing, forward masking, and silent gap detection (Felix et al., 2019). In more detail, evoked responses in the IC are typically transient (1- to 40-ms duration) and sustained (80- to 120-ms). In the KOs, however, a third type of response can be detected with intermediate response (40- to 80-ms) (Felix et al., 2019). Degraded spike timing was also found in the VNLL and SPON, which are primary targets of octopus cells (highly temporal precise cells likely responsible for shaping temporal responses in the midbrain) (Felix et al., 2019).

1.5.2.3 *Cntnap2 knockout*

Contactin-associated protein-like 2 (CNTNAP2) is encoded by an ASD-related gene implicated in language impairments (Rodenas-Cuadrado et al., 2014). The CNTNAP2 is responsible for tethering potassium channels in myelinated axons, being crucial for action potential propagation (Truong et al., 2015). Loss of CNTNAP2 in rodents leads to alterations in social behavior, reduced USVs and hyperactivity (Peñagarikano et al., 2011; Brunner et al., 2015).

Conclusions regarding sensory-motor gating ability of *Cntnap2*-KO mice are not consensual. Different studies report either unchanged (Peñagarikano et al., 2011), impaired (Scott et al., 2018), or more efficient PPI (Brunner et al., 2015; Truong et al., 2015). The same is observed regarding ASR whose changes may impact PPI and explain results disparity (probably also age factor). A battery of tests based on PPI paradigm have been performed in *Cntnap2*-KO. By changing the type of prepulse cue, it is possible to detect impaired ability to perceive short SGs in a continuous broadband white noise background, but increased ability to discriminate slight changes in pitch (Truong et al., 2015). In order to elicit a startle inhibition with SGs, these must be much longer, suggesting that *Cntnap2*-KO have impairments in

temporal sound processing. Ability to attenuate a startle response when a pitch cue was presented was, however, independent of pitch tone duration. The auditory alterations reported in this model seem to be linked to MGB neuronal changes (Truong et al., 2015).

Analysis of ABR to click sounds and pure tones in *Cntnap2*-KO rats shows altered peak amplitudes and latencies but overall unaffected hearing thresholds. In more detail, peaks II, III and IV latencies were observed to be consistently increased in juvenile rats, although this trait was recovered in adulthood. The amplitude of peak IV was decreased across development and in adulthood. Interpeak latencies were also affected, mostly the latency between peaks I-II which was decreased both during development and adulthood (Scott et al., 2018).

Histological data shows reduced neuronal count and size in the MGB, which may help explain sound processing abnormalities. Given the results from ABR testing, further histological data would be useful to clarify the extent of changes in this model, similarly to other ASD models presented in this review (Truong et al., 2015; Scott et al., 2018).

1.5.2.4 *Shank3 knockout*

Being *SHANK3* haploinsufficiency a clear monogenic cause of ASD, dozens of mouse lines carrying different *Shank3* mutations have been generated so far (Monteiro and Feng, 2017). One in particular, carries a human genetic mutation from an ASD patient - the *InsG3680-Shank3* mouse line – making it a valuable translational model in preclinical research. This rodent model displays increased ASR, which indicates a possible impairment in sound processing and potential auditory hypersensitivity. PPI seems to be decreased in this model, although the baseline acoustic reactivity may portrait a confounding factor to this test, as discussed by the authors (Zhou et al., 2016). In a different model, the *Shank3B*-KO, no differences were found in PPI or silent gap (SG) test (Figure 5). On the other hand, *Shank3B*-KO seem to have increased ability to discriminate pitch changes (Rendall et al., 2019).

Impairments in cortical sound processing are reported for heterozygous *Shank3*-deficient rats carrying a 68 bp deletion in exon six with a premature stop codon (Engineer et al., 2018). Cortical response to tone stimulus, noise bursts, and speech sounds, are overall weaker in these rats, but temporal properties seem to be unaltered in response to tones. The same is not true for response to speech sounds, that besides being weaker, is also delayed. Of note, although neural discrimination accuracy does not seem to be impaired when sounds are presented in an isolated manner, neural responses are degraded when sounds are presented at increased rates, such as human speech rate (Engineer et al., 2018).

1.5.2.5 *Pten* conditional *knockout*

PTEN mutations have been identified in individuals diagnosed with ASD and also displaying macrocephaly. Accordingly, *PTEN*-KO mice present several alterations namely increased neuronal soma size, hypertrophic dendrites, higher excitatory spontaneous activity, and hypertrophic and ectopic dendrites (Xiong et al., 2012). Such alterations are also consistent with the known role of this gene, which is required for normal brain wiring and development.

Pten-KO pups tend to present increased frequency of USVs when separated from their mothers, a result interpreted as evidence of higher anxiety (Sarn et al., 2021). Conditional KO of *Pten* in the left AC of mice increases the strength of callosal inputs to that region and the efficiency of excitatory long-range synaptic inputs from contralateral AC and thalamus. An increase in dendritic branch number and spine density together with increased amplitude of miniature excitatory postsynaptic currents is consistent with overall strengthening of synaptic connections in this region (Xiong et al., 2012).

1.5.2.6 *Mecp2* transgenic mouse

The *MECP2* gene encodes methyl-CpG binding protein (MeCP2) that acts as a regulator of gene expression, playing an important role in prenatal neurogenesis and postnatal synaptic development, function, and plasticity (Brand et al., 2021). *MECP2* genetic loss of function is associated with intellectual disability and Rett syndrome (Brand et al., 2021), whereas its duplication is characterized by motor and cognitive impairments, delayed or absent speech, seizures, and ataxia (D'Mello, 2021). In both situations, ASD-related phenotypes are often times present.

Altered sound-evoked cortical responses have been reported in *Mecp2*-overexpressing transgenic mice (*Mecp2*-TG). Although displaying normal CF distribution, thresholds to trigger tone-evoked cortical responses are increased. In contrast, cortical responses to noise are stronger, but delayed. Such abnormalities indicate a noise sensitivity phenotype associated to fast-spiking neurons that might be due to lack of cortical inhibition (Zhou et al., 2019a). Unlike many other ASD models, ABR is normal in *Mecp2* overexpressing mice and cortical tonotopy does not seem to be affected (Zhou et al., 2019a).

1.5.2.7 Other ASD models displaying auditory related impairments

Although far less explored, there are other animal models that potentially display auditory processing abnormalities. The *Cyfip1*$^{+/-}$ mouse model presents a lower PPI, evidencing sensory-motor gating impairments (Domínguez-Iturza et al., 2019) and the *Nrxn1α*-KO presents increased ASR without

changes in PPI, perhaps due to acoustic hypersensitivity (Esclassan et al., 2015). However, PPI results in *Nrxn1α*-KO rats may be confounded by their decreased ASR (Esclassan et al., 2015). *Adnp*$^{+/-}$ mice display increased ABR thresholds and latency, as well as decreased number of USV calls. Such findings might be a consequence of the reported significant hearing loss displayed by *Adnp*$^{+/-}$ mice (Hacohen-Kleiman et al., 2019).

1.6 Open questions and future perspectives

Increasing evidence from animal models demonstrates that auditory-perceptual alterations found in ASD patients can be recapitulated in several animal models. Such neurodivergent processing of auditory inputs, translated into hypo- or hypersensitivity to sensory stimulation, may have a strong impact on behavior and impose limitations in the quality of life for individuals diagnosed with ASD. In particular, auditory processing abnormalities may underlie deficits in communication and social interaction. Tackling the neurobiological mechanisms causing such alterations becomes of utmost importance to design strategies to attenuate or prevent sensory impairments. Rodent models are a powerful resource to better understand behavioral and neurobiological alterations in ASD, holding tremendous translational potential.

Despite the great diversity of ASD models, mirroring the great heterogeneity in the etiology of ASD, it is possible to identify shared features across models. Auditory impairments seem to arise from deficits in central processing rather than from periphery. Along the auditory pathway, multiple defects are observed, such as decreased tonotopicity, altered thresholds to sound stimuli, and abnormal spectral and temporal processing (especially in the auditory regions of the brainstem and cortex). The origin of these differences is still not fully understood, but E/I imbalances during postnatal development seem to be contributing to these defects, mainly due to impairments in GABAergic signaling.

Future work is needed to better support these observations and unveil specific regions, neuronal circuits, and molecular players that are determinant for the auditory phenotype. Since ASD is a neurodevelopmental disorder, clarifications on critical developmental stages will be crucial, together with the establishment of novel molecular targets that might be particularly effective during those developmental windows. Together, this knowledge will hopefully help defining efficient therapeutic approaches in the near future.

Table 2. Overview of the most relevant findings regarding ASD rodent models with reported auditory dysfunctions. Abbreviations: acoustic startle response (ASR), prepulse inhibition (PPI), phosphatidylinositol-3-kinase (PI3K), auditory cortex (AC), auditory brainstem response (ABR), medial geniculate body (MGB), inferior colliculus (IC), ventral nucleus of the lateral lemniscus (VNLL), superior paraolivary nucleus (SPON), medial nucleus of the trapezoid body (MNTB), valproic acid (VPA).

Model	Gene	Mouse *locus*	Human *locus*	Protein	Protein function	Main findings
***Shank3*-KO**	*Shank3*	15; 15 E3	22q13.3	SHANK3 (SH3 and multiple ankyrin repeat domains protein 3)	Scaffold protein important for organization of excitatory synapses and integrity of the post-synaptic density (Monteiro and Feng, 2017).	Increased ASR, decreased PPI, increased ability for pitch discrimination (Zhou et al., 2016; Rendall et al., 2019). Weaker cortical responses to sounds, temporal processing is impaired when sounds are presented at high rate, resembling speech rate (Engineer et al., 2018).
***Pten* conditional KO**	*Pten*	19 C1; 19 28.14 cM	10q23.31	PTEN (phosphatase and tensin homolog)	Negative regulator of the PI3K/AKT signaling, important for cell growth, proliferation and survival, and axonal growth (Zhou and Parada, 2012; Sarn et al., 2021).	Strengthened synaptic connectivity: stronger callosal inputs to the AC from contralateral AC and thalamus (Xiong et al., 2012).
***Cntnap2*-KO**	*Cntnap2*	6; 6 B2.2- B2.3	7q35-q36.1	CNTNAP2 (Contactin associated protein 2)	Maintenance of normal action potential propagation through tethering of potassium channels in myelinated axons (Truong et al., 2015).	Increased pitch discrimination, but impaired temporal processing of sounds. Altered ABRs (peak amplitudes and latencies), histological alterations in MGB (Truong et al., 2015; Scott et al., 2018).
***α7-nAChR*-KO**	*Chrna7*	7 C; 7 34.47 cM	15q13.3	α7-AChR (α7-nicotinic acetylcholine receptor)	Ligand-gated cationic channel that interacts with acetylcholine and mediates synaptic transmission (Schaaf, 2014; De Jaco et al., 2016).	Increased latency of ABR peak IV, atypical spectral and temporal response of IC neurons. Degraded spike timing in VNLL and SPON (Felix et al., 2019).
***Fmr1*-KO**	*Fmr1*	X A7.1; X 34.83 cM	Xq27.3	FMRP (Fragile X Mental Retardation Protein)	Actin remodeling, regulation of cytoskeleton-related gene expression (Braun and Segal, 2000).	Behavioral evidence of deficits in sound processing and hyperacusis (Reinhard et al., 2019; Auerbach et al., 2021). Altered cortical responses to different types of stimuli (Rotschafer and Razak, 2013), higher ABR thresholds (Rotschafer et al., 2015) and lack of tonotopicity in MNTB (Strumbos et al., 2010; Ruby et al., 2015), IC (Nguyen et al., 2020) and AC (Rotschafer and Razak, 2013).
***Mecp2*-TG**	*Mecp2*	X A7.3; X 37.63 cM	2p16.3	MECP2 (methyl-CpG binding protein 2)	Mainly expressed in the brain. Gene expression regulator, important for prenatal neurogenesis and synaptic development (Brand et al., 2021).	Normal ABR and cortical tonotopy. Increased thresholds for tone-evoked cortical responses, heightened and delayed cortical responses to noise (Zhou et al., 2019a).
VPA	*N/A*	*N/A*	*N/A*	*N/A*	*N/A*	Reduced USVs throughout life, normal ASR but reduced PPI suggesting sensory-motor gating impairments (Gandal et al., 2010). Cortical alterations on LFPs, temporal and spectral processing, and tonotopicity (Engineer et al., 2014a; Anomal et al., 2015). Auditory brainstem overactivation upon sound stimulation (Dubiel and Kulesza, 2016). Impaired connectivity between the brainstem and the midbrain, which is one of the most susceptible regions to VPA exposure (Zimmerman et al., 2020).
Thalidomide	*N/A*	*N/A*	*N/A*	*N/A*	*N/A*	Impairments in MNTB: diminished in size, fewer projections, expanded responsive area to sound stimulation (Ida-Eto et al., 2017; Tsugiyama et al., 2020).

2 RESEARCH OBJECTIVES

Sensory-perceptual abnormalities are present in approximately 90% of individuals with ASD being auditory hypersensitivity one of the most commonly reported sensory-perceptual abnormalities. This translates into a huge impact on patients' life quality and may even underlie other ASD-related traits such as communication difficulties.

Several animal models used in ASD studies share traits of auditory dysfunction, namely hypersensitive auditory phenotypes, which could suggest a shared upstream mechanism among different animal models of ASD. Accordingly, our research group has been studying auditory sensory function in a transgenic mouse line that carries an ASD-patient derived mutation – the *Shank3-InsG3680*$^{+/+}$ mice. In line with the literature, we found that these mice present not only typical ASD-like behaviors such as social interaction deficits and repetitive behaviors, but also behavioral auditory hypersensitivity (unpublished).

In order to begin unveiling potential molecular mechanisms that might underlie auditory sensory dysfunction in the *Shank3-InsG3680*$^{+/+}$ mouse model of ASD, we decided to focus this dissertation work on the A1 brain region (primary auditory cortex). It is our aim to:

1. Identify unique molecular signatures in the primary auditory cortex of *Shank3-InsG3680*$^{+/+}$ mutant mice;

2. Evaluate the emergence of such molecular signatures along development;

3. Study those alterations at the molecular and functional levels and evaluate potential cell-type specific profiles.

This work will contribute to a better understanding of the molecular and cellular changes occurring in the developing ASD brain. Results may potentially uncover novel molecular targets which may hold future therapeutic potential in ASD.

3 METHODS

3.1 Animals

Animals used in this study (C57/BL6 male *Shank3-InsG3680*$^{+/+}$ and WT controls) were housed in an animal facility approved by Portuguese national authorities (Direção Geral de Alimentação e Veterinária - DGAV). Housing was performed at standard conditions (temperature 20-24 °C, humidity 55 ± 10%), with a light/dark cycle of 12/12 h. Food (Mucedola: 4RF25 during gestation and before weaning, 4RF21 post weaning) and water were available *ad libitum*. All animals were housed in polysulfone cages (1264C EUROSTANDARD type II or 1284L EUROSTANDARD type II L, Tecniplast) in groups of 5 to 6 mice respectively. The floor of the cages was covered by corncob bedding and enriched with tissue paper before weaning and with a combination of tissue paper and paper strips after weaning, both to enable naturalistic nesting behavior. All animal procedures were approved by national authorities Direção Geral de Alimentação e Veterinária (ID: DGAV 8519), the Ethics Subcommittee for Life Sciences and Health (SECVS) of University of Minho (ID: SECVS 01/18) and were performed in accordance with European Community Council Directives (2010/63/EU) and the Portuguese law DL N° 113/2013 for the care and use of laboratory animals.

3.2 Genotyping

Genotype of the animals used in this study was confirmed through polymerase chain reaction (PCR) analysis. Between postnatal days 10 and 14, a tail sample was collected and preserved at -20 °C until further processing. For DNA extraction, a strong alkaline solution (25 mM NaOH, 0.2 mM EDTA, pH 12) was added to each tail sample. After 30 minutes incubation at 95 °C, a neutralization buffer (40 mM Tris-HCl, pH 5) was added in 1:1 ratio. The PCR for *Shank3* fragment amplification was performed with MyTaq PCR Mix (Bioline, BIO-25041: Taq buffer containing MgCl, 10 nM dNTPs (dCTP, dGTP, dATP, dTTP), Taq polymerase enzyme, template DNA from each tail sample, forward and reverse primers:

Primer forward - 5' AGCTGGCCTCATTGTTGTG 3'

Primer reverse - 5' CAGGTTCACAGCGAATACCA 3'

Samples from known WT, *Shank3-InsG3680*$^{+/+}$ and *Shank3-InsG3680*$^{+/-}$ animals were used as positive controls together with a negative control without any DNA sample. The initial denaturation step lasted for 1 minute at 95 °C followed by 35 repeated cycles of: denaturation at 95 °C, primer annealing at 58 °C and polymerization at 72 °C. All these three steps lasted for 15 seconds each, at every cycle. After this, samples were kept at 8 °C. The PCR product was mixed with bromophenol blue (1:1 ratio)

and loaded to a 1.5% agarose gel containing GreenSafe and submerged in Tris/Borate/EDTA buffer (TBE). An electric current of 100 V was applied during ≈1.5 h for DNA migration and band resolution. The gel image was obtained with Gel-Doc (BIO RAD) and the genotype was determined by comparison of the obtained bands with the above-mentioned positive controls.

3.3 Behavioral tests

All behavioral tests were performed at nighttime, which corresponds to the active period of mice. The mice used were 7 weeks-old (Figure 8A). Before testing, animals were habituated to the room for at least 1 hour under the same lighting conditions as the experimental test.

3.3.1 Splash test

Each animal was placed in an individual polysulfone box (42,5×26,6×18,5 cm; clean housing cage) containing corncob bedding covering the entire floor and evenly exposed to dim light (100 – 110 lux). At beginning of the test, animals were sprayed on their dorsal coat with a 30% sucrose solution and a transparent acrylic cover was placed on top of the cage to allow animal visualization and videotaping for 10 minutes (Figure 6). The number and duration of grooming bouts, rears and digs were manually counted from the resulting videos. Grooming bouts comprise nose and face grooms (circular movements around these regions), head grooms (circular movements encompassing the top head of the animal and the ears) and body grooms (body fur scratching or licking) (Yalcin et al., 2005).

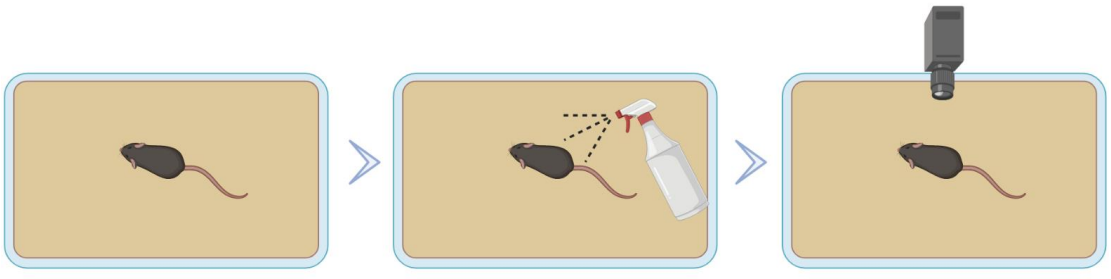

Figure 6. Schematics of the splash test paradigm.

The animal is placed in a clean homecage containing bedding on the floor. The animal's back is then sprayed with a 30 % sucrose solution and the resulting behavior is videotaped for 10 minutes. Created with Biorender.com.

3.4 Acute brain slices preparation

Acute brain slices were prepared for both A1 macrodissection and further protein/RNA extraction and for patch clamp electrophysiology assays (Figure 8B). The mice were deeply anesthetized with avertin (tribromoethanol 20 mg/mL in PBS; dose of 0.5 mg/g body weight). After confirming lack of pedal withdrawal reflex, animals were transcardially perfused with room-temperature (RT) NMDG-based solution (in mM): 30 NaHCO3, 25 glucose, 20 N-(2-Hydroxyethyl)piperazine-N'-(2-ethanesulfonic acid) (HEPES), 18 N-methyl-D-glucamine (NMDG), 10 MgSO4, 5 Na-ascorbate, 3 Na-pyruvate, 2.5 KCl, 2 thiourea, 1.2 NaH2PO4, 0.5 CaCl2 (≈300 mOsm, pH 7.3-7.4, all reagents from Sigma Aldrich) saturated with carbogen (95% O_2/ 5% CO_2). After extracting the brain, the cerebellum and the olfactive bulbs were removed and the brain was transferred to the same NMGD-based solution for sectioning. Acute horizontal brain slices (300 µm-thick) containing the primary auditory cortex (A1) were cut in a Vibratome Leica VT1000S programmed for 1 mm cutting amplitude and level 10 frequency.

3.4.1 Primary auditory cortex macrodissection

Acute brain slices described above were transferred to a petri dish containing carbogenated NMDG-based solution and the A1 region was quickly dissected under a magnifier (Figure 8B). Immediately after the dissection, the tissue was promptly collected, snap-frozen in liquid nitrogen and stored at -80 °C until further use. All samples frozen contained A1 from 3 different mice combined per group and were later used for protein or RNA extraction.

3.4.2 Acute brain slices preparation for *ex vivo* patch clamp electrophysiology

Brain slices containing A1 were prepared as described above (section 3.4) and transferred to NMDG-based solution at 32 °C where they were left to recover for 11 minutes (Figure 8B). Slices were then transferred to regular artificial cerebrospinal fluid (aCSF, in mM): 119 NaCl, 24 $NaHCO_3$, 12.5 glucose, 2.5 KCl, 2.0 $CaCl_2$, 2.0 $MgSO_4$, 1.2 NaH_2PO_4, (≈300 mOsm, pH 7.3-7.4, all reagents from Sigma Aldrich) where they were left to recover for at least 1 hour at RT. Slices were then used for patch clamp electrophysiology recordings.

3.5 Protein extraction and quantification

A1 tissue previously frozen (section 3.4.1) was manually homogenized in ice-cold RIPA buffer (150 mM NaCl, 0.1% SDS, 50 mM Tris-Base, 1% Triton, 0.5% sodium deoxycholate) containing protease and phosphatase inhibitors (Complete EDTA free and PhosSTOP, Roche). The resultant homogenate was left

shaking for 2 h at 4 °C and then centrifuged at 14000 rpm for 15 minutes at 4 °C. The supernatant was collected, and total protein was quantified using the BCA protein assay kit from Biorbyt. Samples were then stored at -80 °C and later used for western blot and proteomics screening.

3.6 Proteomics screening by SWATH-MS

Briefly, protein extracts from postnatal days P10, P14, P21, P35, and 6 and 10 weeks (Figure 8A) were prepared from A1 brain tissue and shipped to The Mass Spectrometry Unit of the Center for Neuroscience and Cell Biology - University of Coimbra. Proteomics analysis was performed using information-dependent acquisition (IDA) and SWATH-MS (Sequential Windowed data independent Acquisition of the Total High-resolution Mass Spectra). For IDA, 10 µg from each sample was pooled for each genotype, resulting into 2 pooled samples representing the WT and the *InsG3680*$^{+/+}$ group. The remaining individual protein samples were used for SWATH analysis. Both individual and pooled samples were denaturated and alkylated before separation by SDS-PAGE. The resultant gels were separated into 3 fractions, destained, and then proteins were digested with trypsin. The resultant digested peptides were extracted from the gels and the organic solvents used for this purpose were then evaporated. The portions of peptides for IDA extracted from each gel piece were kept separated, while the gel pieces from each sample for SWATH were joined together. All samples were resuspended and sonicated before liquid-chromatography/mass spectrometry analysis (LC-MS).

The basis for LC separation is that molecules with different properties will have different affinities towards either the stationary phase or the varying mobile phases they contact with. Here, the mobile phases used were combinations of different proportions of dimethyl sulfoxide (DMSO) and formic acid in water or acetonitrile. After this stage, the peptides were ionized and separated according to the respective mass-to-charge ratio (m/z), through a technique called mass spectrometry (MS) that was, in this case, coupled with the LC component. Finally, to obtain an ion library, the data acquired with the IDA samples was compared against an online protein database, which allowed the protein identification. SWATH plug-in PeakView was used for relative quantification of proteins in each sample. Only proteins with a false-discovery rate (FDR) inferior to 1% were considered for quantification and the sum of the peak areas attributed to each eligible protein was normalized to the sum of the total peak area of the sample.

3.7 Western Blot

Protein extracts from mice A1 (Figure 8) containing 40 µg of total protein were eluted in 4x laemmli buffer (Tris-base, SDS, glycerol, 2-mercapto-ethanol, bromophenol-blue) and run on a 10% SDS-PAGE (80

minutes, 120 V) in triplicates. The proteins were blotted in a nitrocellulose membrane through wet transfer method, using an ice-cold transfer buffer [0.125 M tris-Base, 0.96 M glycine, 20% (v/v) methanol] for 2 h at 100 V on ice to prevent protein denaturation due to overheating. Blots were blocked for 1 h in blocking buffer containing 5 % milk and 1 % normal goat serum (NGS) in TBS-Tween 20 (TBST, 0.01%) and incubated with the primary antibodies - polyclonal rabbit-anti-HCN1 (1:200, #APC-056, Alomone Lab) and monoclonal mouse-anti-β-actin (1:20000, #A5441, Sigma-Aldrich) - in 1% milk, 1% NGS overnight at 4 °C. Membranes were washed 3 times for 10 minutes in TBST (0.01%) and probed with HRP (horseradish peroxidase) conjugated secondary antibodies: polyclonal goat-anti-rabbit IgG and goat-anti-mouse IgG (1:1000, #AB_2313567 and #AB_10015289, Jackson ImmunoResearch Europe, Lda.). For detection, HRP substrate was added to the blot membrane, incubated for ≈3 minutes (Pierce™ ECL Plus Western Blotting Substrate, Thermo Scientific™) and then scanned in Azure Saphire Biomolecular Imager.

3.8 Real-Time Quantitative PCR

The transcript levels of *Hcn1*, *Hcn2* and *Hcn3* were assessed in samples from A1 region (Figure 8A).

3.8.1 RNA extraction and purification

RNA was extracted after tissue homogenization with TRIzol (ThermoFisher), using chloroform (Sigma-Aldrich) in a 5:1 ratio. The samples were incubated for a total of 5 minutes at room temperature, being vigorously shaken in the first 30 seconds of incubation and then centrifuged for phase separation. The aqueous phase (top, colorless layer) was kept for RNA co-precipitation with 5 µg of RNase-free glycogen using isopropyl alcohol. After shanking vigorously and incubating at RT for 10 minutes, the samples were centrifuged (12000g, 10 minutes at 4 °C) and the supernatant removed. To wash the RNA, the pellet was resuspended in ethanol 75% (v/v), centrifuged (7500 g, 5 minutes, 4 °C) and left to air-dry for approximately 5 to 10 minutes. Purified RNA samples were dissolved in RNase-free water and quantified by spectrophotometry (NanoDrop). Absorbance at 260 nm was used to obtain RNA concentration and the ratio between the sample's absorbance at 260 nm and 280 nm (reference absorbance for proteins) was used to assess purity. Acceptable samples should have A260/A280 ≈ 2.

3.8.2 RNA synthesis

Before complementary DNA (cDNA) synthesis, a DNAse treatment was applied to remove contaminant genomic DNA. For that, RNA samples were incubated with DNAase I in a buffer containing

$MgCl_2$ (ThermoFisher Scientific) at 37 °C for 30 minutes, after which the samples were heated to 65 °C for enzyme denaturation, during 10 minutes with EDTA. cDNA was obtained using qScript™ cDNA SuperMix (QuantaBio), following the manufacturer instructions (reaction protocol: 5 minutes at 25 °C, 30 minutes at 42 °C and 5 minutes at 85 °C).

3.8.3 Real-time quantitative PCR

For real-time quantification, the cDNA was amplified and probed using HOT FIREPol® EvaGreen® qPCR Mix Plus (Solis Biodyne). The primers used are listed below in Table 3. Before the amplification phase, the samples were heated to 95 °C for 15 minutes for sample denaturation and enzyme activation. This was followed by 40 cycles of amplification that consisted of a 95 °C denaturation step of 15 seconds, a 59 °C annealing step for 20 seconds and a 72 °C elongation step for 30 seconds. The melting curve was obtained by fluorescence measurements throughout a temperature ramp from 59 °C to 95 °C (see Figure 7). Actin was used as a reference gene.

Table 3. Primer sequence used for gene amplification in RT-qPCR. The location (nucleotide position) and size of each gene fragment amplified are also indicated.

Primer	Sequence (5' → 3')	Nt position	Size	Gene	Gene accession number
HCN1	F - CTCAGTCTCTTGCGGTTATTACG R - TGGCGAGGTCATAGGTCAT	1138 - 1228	91	*Hcn1*	NM_010408
HCN2	F - ATCGCATAGGCAAGAAGAACTC R - CAATCTCCTGGATGATGGCATT	1936 – 2037	102	*Hcn2*	NM_008226
HCN3	F - GTGCAGTGGTTCGCATCTTC R - AGTGGTTCACCATGCGGTTC	867 - 1007	141	*Hcn3*	NM_008227
β-Actin	F - CCACACCCGCCACCAGTTCG R - TACAGCCCGGGGAGCATCGT	88 – 199	112	*Actb*	NM_007393.3

The difference between the threshold cycle (C_T) value of the target gene and the reference gene (ΔC_T) was normalized to the WT (control group) values in each age group ($\Delta\Delta C_T$) and transformed to the form of $2^{-\Delta\Delta C_T}$.

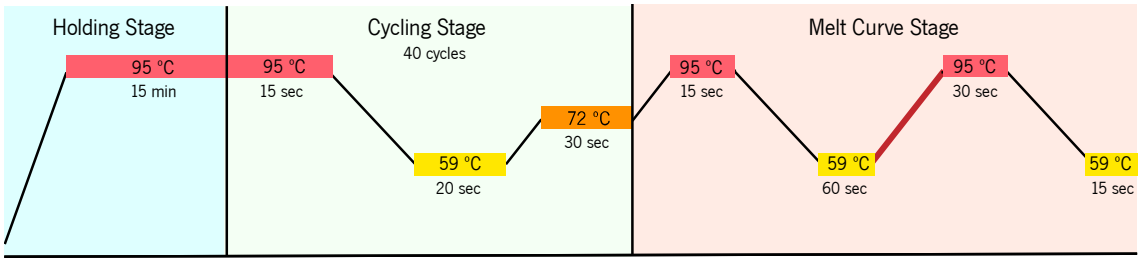

Figure 7. Schematics of the thermic profile for HCN gene amplification and real-time quantification.

3.9 Electrophysiology recordings

Patch clamp recordings were performed as previously described (Yi et al., 2016). From a group of WT and *Shank3-InsG3680*$^{+/+}$ mice aged 7 to 10 weeks (Figure 8), one animal was selected per day for whole-cell patch clamp recording. For each recording, a brain section previously prepared (according to above sections) was placed in the recording chamber and continuously perfused with carbogenated aCSF, at 2 mL/min and 32-34 °C. Patch pipettes were pulled from borosilicate-glass capillaries (GB150F-8P, Science Products) using a P1000 horizontal puller (Sutter Instruments) and filled with potassium-gluconate internal solution (in mM): 131 K-gluconate, 17.5 NaCl, 1 $MgCl_2.6H_2O$, 10 HEPES, 1.1 EGTA, 2 MgATP, 0.2 Na_2GTP, 17.5 KCl (pH 7.4, 300-315 mOsm, all reagents from Sigma Aldrich). The pipette resistance, when filled with the internal and in contact with the bath solution, was typically 2 – 4 MΩ. After accommodating the slice in the recording chamber, it was visualized with an Olympus BX51WI microscope. Recordings were performed in deeper layers (between L4 and L6) of the A1. The membrane resistance (R_m, in MΩ), access resistance (R_a, in MΩ), holding current (in pA), membrane capacitance (C_p, in pF) and membrane time constant (τ_{memb}, in ms) were automatically calculated by the Clampex software (Molecular Devices) and were saved before each recording. Whole-cell patch clamp recordings were performed in voltage-clamp (V_c) mode. From a holding potential of -70 mV, several 2-seconds hyperpolarizing voltage steps were sequentially applied in 10 mV intervals until -130 mV. By the end of each step, the clamping voltage returned to -70 mV for 1 second. This voltage protocol was applied for each cell and recordings were always obtained in 2 conditions: aCSF media (baseline recordings) and 15 minutes after incubation with aCSF media containing 10 µM ZD7288 (Sigma-Aldrich) to fully block HCN channels (ZD7288 recordings) (Shah, 2016). The signal was acquired using Digidata 1440 and MultiClamp 700B (Molecular Devices) at 20 kHz and low-pass filtered at 1 kHz. The amplitude of steady state currents (I_{ss}) was measured at the end of the hyperpolarizing voltage step in all recordings. The amplitude of the hyperpolarization currents (I_h) was obtained after deducting the ZD7288 trace to the

corresponding control trace of each cell and measure the current amplitude at the end of the hyperpolarizing step. All current amplitudes were normalized to the cell's capacitance and represented as current density, in pA/pF. I_h decay time constant (τ_{act}, ms) was obtained by fitting the initial segment of the -130 mV step with a mono-exponential function (equation 1). To measure the impact of HCN blockade on the R_m, R_m change was calculated (ΔR_m) by the difference between the R_m value after ZD7288 incubation for 15 minutes and the R_m value at baseline conditions [$\Delta R_m = R_m(ZD7288) - R_m(Baseline)$]. Cells with an R_a > 20 MΩ were discarded.

Equation 1. Standard mono-exponential function. Function used to fit the initial segment of each I_h sweep. This fits the amplitude A, the time constant τ_{act}, and the constant y-offset C for each component i (Yang et al., 2018).

$$f(t) = \sum_{i=1}^{n} A_i e^{-t/\tau act_i} + C$$

3.10 Statistical analysis

Statistical analysis and data visualization was done using GraphPad Prism 8 software. All data was checked for normality through the Shapiro-Wilk test and the Kolmogorov-Smirnov test. Outliers were detected using the "Outlier Calculator" from GraphPad that uses the extreme studentized deviate method with a 0.05 significance level.

For behavioral analysis, a two-tailed independent samples Student's *t*-test was used to compare the time each group spent performing a behavior and the respective number of events. For proteomics analysis, all samples were normalized to the WT levels and one sample student's *t*-test was used to compare the fold-change of *Shank3-InsG3680*$^{+/+}$ protein levels in comparison to matching WT controls. For the RT-qPCR, the $2^{\Delta\Delta_{Ct}}$ was compared between genotypes at each timepoint through an unpaired student's t-test or the corresponding non-parametric Mann-Whitney test whenever normality could not be assumed.

In patch clamp analysis, R_m, ΔR_m and τ_{act} values were compared by unpaired student's *t*-tests or by ANOVA mixed-effects model in the cell type-specific analysis. All current-voltage (I-V) curves were analyzed using the mixed-effects model. The effect of ZD7288 in I_{ss} current amplitude was compared through Student's paired *t*-tests.

The level of confidence used for all statistical tests was 95% unless stated otherwise. Results are reported with mean and standard deviation (SD) (see supplementary tables in annexes for detailed statistical reports) and plotted with mean and standard error of the mean (SEM). Statistical significance was considered when the p-value (p) ≤ 0.05, unless stated otherwise.

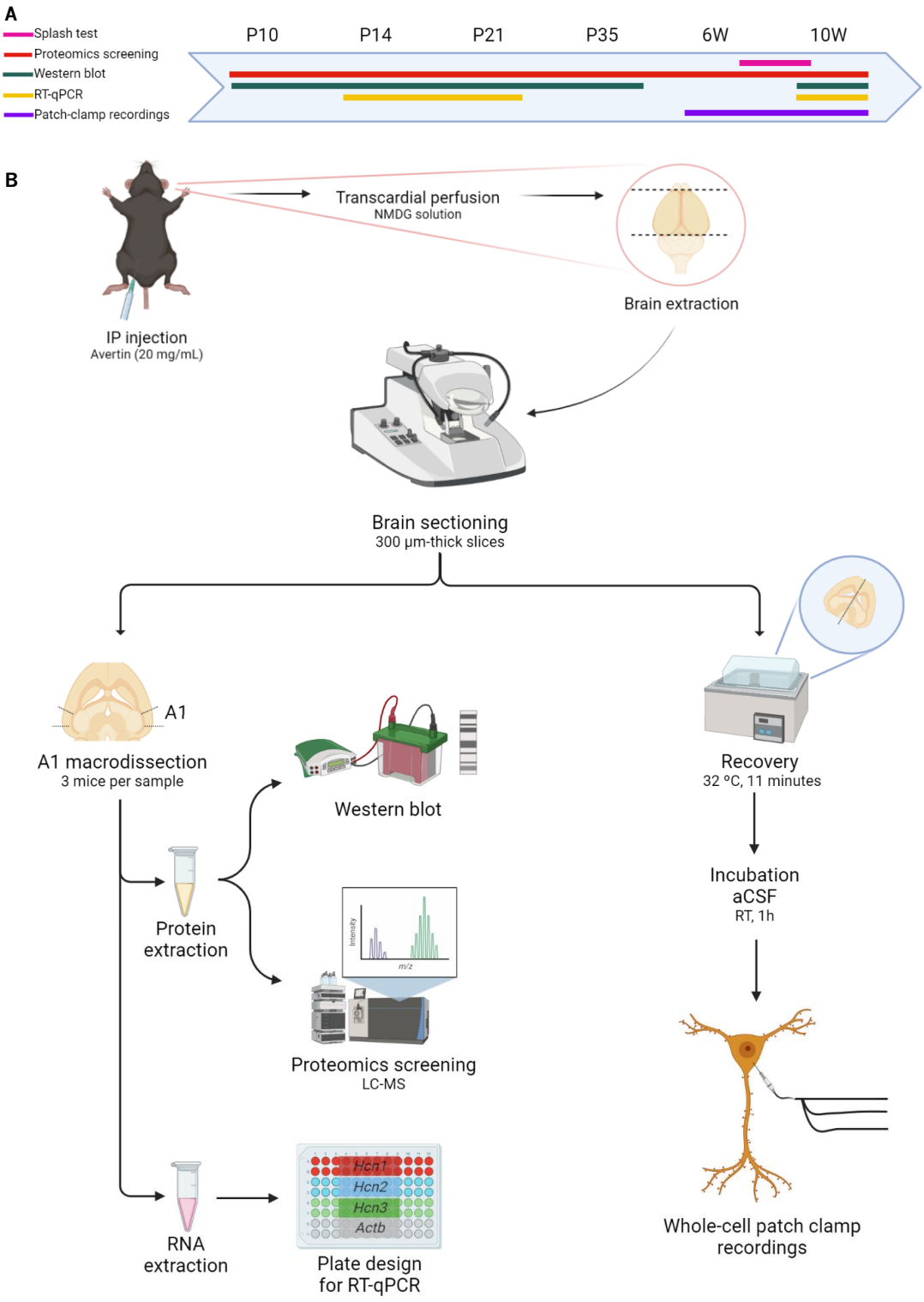

Figure 8. Schematics of the study design used for molecular and functional experiments.

A) Experimental timeline indicating the timepoints at which the different procedures were performed. B) Schematic representation of the study design. For molecular biology and *ex vivo* electrophysiology experiments, acute horizontal brain sections were obtained to extract the primary auditory cortex (A1). Mice were deeply anesthetized with avertin and transcardially perfused with NMDG-based solution. Brain was quickly extracted and sectioned in 300 µm-thick slices using a vibratome. A1 region was macrodissected and used for protein or RNA extraction. After protein quantification, protein homogenates were used for proteomics screening or western blot analysis. For *ex vivo* electrophysiology, the brain slices were recovered in NMDG-based solution at 32 °C for 11 minutes and incubated in regular aCSF at room temperature (RT) for 1 h and afterwards recordings were performed. Created with Biorender.com

4. RESULTS

4.1 Genotyping protocol allows identification of mutant mice

All mice genotypes were confirmed by PCR analysis where a fragment of the *Shank3* gene was amplified. This fragment comprised the guanine insertion locus (*InsG3680*), allowing the distinction between all possible genotypes (Figure 9):

- *InsG3680*$^{+/+}$ mutants: longer PCR fragment, producing a band of 310 base pairs (bp) due to the presence of the guanine insertion with leftover cassette from the original targeting vector;

- Wild type (WT) / *InsG3680*$^{-/-}$ mice: shorter PCR fragment, producing a band of 235 base pairs (bp) due to the absence of the extra guanine and its associated leftover transgenic cassette;

- *InsG3680*$^{+/-}$ mice: presence of both fragments (310 and 235 bp), indicating the presence of a WT allele as well as a mutant allele.

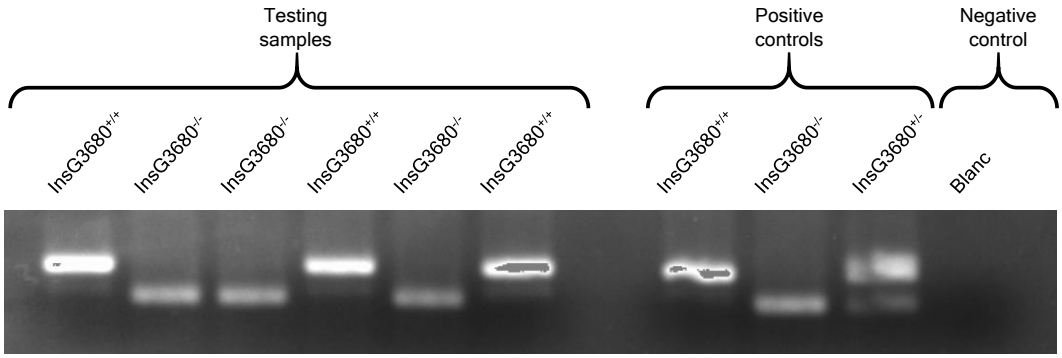

Figure 9. Representative genotyping gel.

Image shows an agarose gel containing several gene amplification products. The bands obtained in the testing samples are identified by comparison to the positive controls. The fragments containing the guanine insertion mutation correspond to the higher molecular weight bands. Hence, samples containing a single band of higher molecular weight represent transgenic homozygous mice *(Shank3-InsG3680*$^{+/+}$). Samples displaying only a lower molecular weight band represent wild type mice (*InsG3680*$^{-/-}$). Samples contain both alleles (*InsG3680*$^{+/-}$) represent heterozygous mice which were not used in this study. Negative control does not contain any DNA sample.

4.2 *InsG3680*$^{+/+}$ mice present repetitive grooming behavior

After successful establishment of a transgenic mouse colony of *Shank3-InsG3680*$^{+/+}$ mice, we proceed to evaluate their ASD-like behavioral phenotypes. Results show that *InsG3680*$^{+/+}$ mice have

reduced social interaction as well as auditory hypersensitivity (data obtained by other lab members; data not shown), hence, we proceed to evaluate their grooming behavior.

Repetitive and stereotyped behaviors are one of the core features of ASD (American Psychiatric Association, 2013). This feature is also quite extensively reported for animal models of ASD (Gandhi and Lee, 2021), including different *Shank3* mutant mouse lines (Peça et al., 2011; Yoo et al., 2019; Liu et al., 2021). Increased spontaneous grooming has been previously reported in *InsG3680*$^{+/+}$ mice (Zhou et al., 2016). Here, we used the splash test to investigate induced grooming behavior. The splash test begins by spraying mice's fur coat with a sucrose solution, followed by behavioral videotaping for 10 minutes. The solution triggers a self-care grooming behavior in order to remove the sticky sucrose solution from the fur (Pitzer et al., 2022).

Results revealed that *InsG3680*$^{+/+}$ mice spent significantly more time grooming compared to WT control group (Figure 10, A). Besides total time, the number of grooming bouts was also significantly increased in the mutant group (Figure 10, B). When analyzing the videos, we noticed that other behavioral patterns also seemed altered. Hence, exploratory and naturalistic behaviors such as rearing and digging were also quantified. Data revealed that *InsG3680*$^{+/+}$ mice tended to spend less time rearing compared to WT controls, although the difference did not reach statistical significance. The same tendency was also observed in the number of rearing bouts (Figure 10, C and D). Strikingly, *InsG3680*$^{+/+}$ did not display any digging behavior during the entire duration of the test while WT controls spent approximately 10% of their time digging (Figure 10 E and F). Together, these findings show that *InsG3680*$^{+/+}$ mice present repetitive grooming and reduced exploratory behavior (Figure 10G and H), perhaps due to high anxiety levels. Such behavioral alterations add face validity to their construct validity as a rodent model of ASD.

Given our hypothesis that sensory alterations in the auditory pathway, namely auditory hypersensitivity, may lead to social withdrawal, acoustic avoidance and promote self-centered behaviors, we proceeded to explore the molecular landscape of primary auditory cortex brain region in *InsG3680*$^{+/+}$ mice.

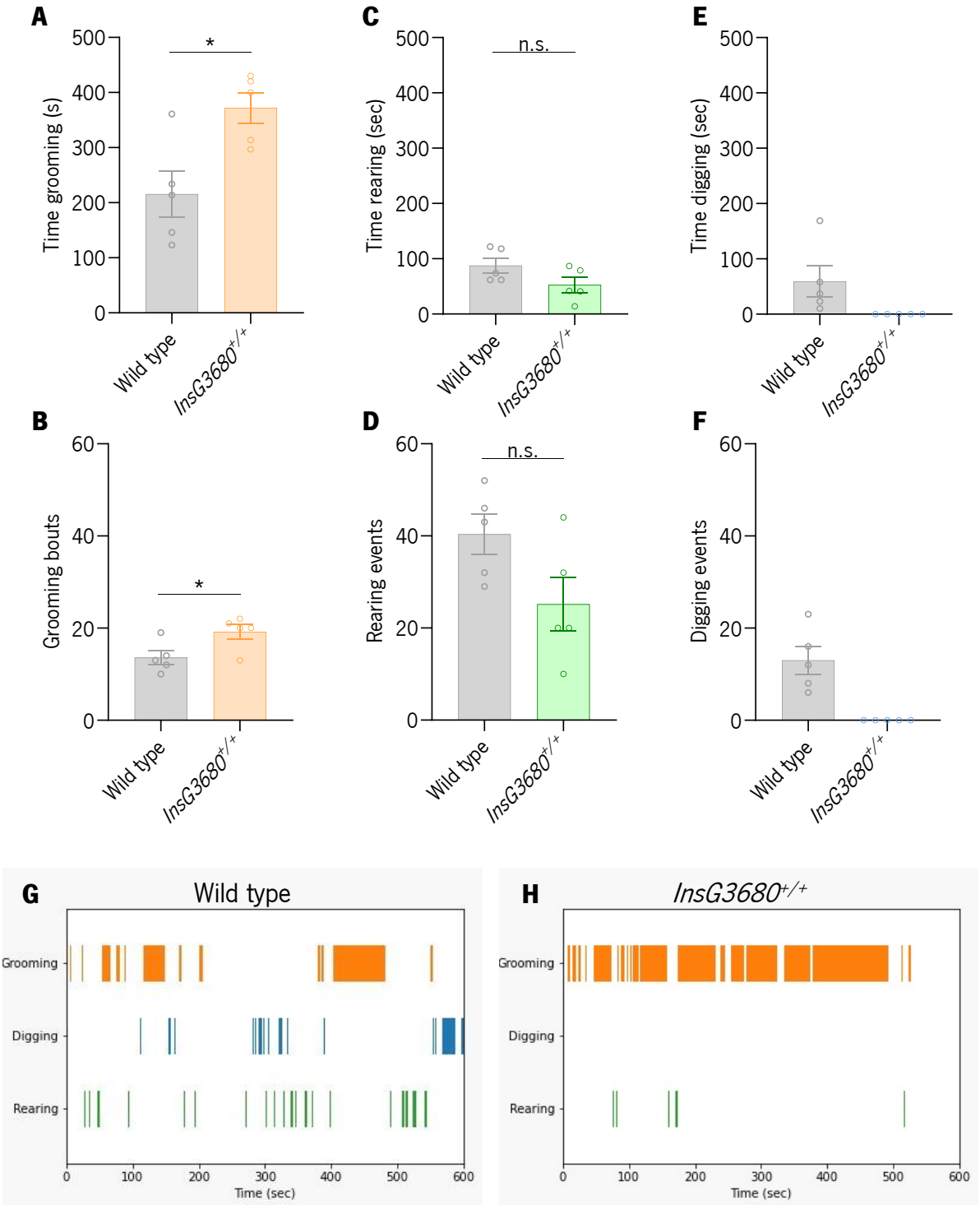

Figure 10. Behavioral results from the splash test: *InsG3680*$^{+/+}$ mice spend more time grooming and less time digging and rearing.

Splash test successfully induced grooming behavior in both genotypes. However, *InsG3680*$^{+/+}$ mice spent significantly more time grooming (A) and had a higher number of grooming bouts (B) when compared to wild type (WT) controls. Although not statistically significant, the time spent rearing (C) and the number of rearing events (D) display a trend towards reduction in *InsG3680*$^{+/+}$ mice. Digging behavior was absent

in *InsG3680*$^{+/+}$ mice during the splash test (E, F). Illustrative timestamps for one WT (G) and one *InsG3680*$^{+/+}$ mouse (H) showing the distribution of grooming, digging and rearing events during the entire duration of the splash test (G,H). Two-tailed unpaired Student's *t*-test, n = 5 mice per group (male, 7 weeks old); Data are mean ± SEM; *p < 0.05, n.s. not significant.

4.3 *InsG3680*$^{+/+}$ mice have HCN1 overexpression in A1 region

To begin unveiling potential molecular underpinnings of auditory hypersensitivity, we performed a shotgun proteomics analysis of the primary auditory cortex (A1) of adult (6- and 10-week-old, 6W and 10 W) *InsG3680*$^{+/+}$ and WT control mice. From 4144 proteins identified, 2862 were confidently quantified by SWATH-MS. Then, using the online open-access tool REACTOME, we restricted our analysis to proteins involved in neuronal pathways (139 proteins). For each of those, the *InsG3680*$^{+/+}$ relative protein level was normalized to its matching WT sample (Figure 11A). Several proteins were found to be significantly altered in *InsG3680*$^{+/+}$ mice (Figure 11B). The top 10 upregulated and downregulated proteins are represented in Figure 11C and 11D. As expected, SHANK3 was the top downregulated protein, consistent with the known effects of *InsG3680* mutation where the insertion of a single guanine nucleotide (G) at cDNA position 3680 leads to a frameshift mutation and a downstream stop codon. One of the most upregulated proteins found in adult *InsG3680*$^{+/+}$ mice was the hyperpolarization cyclic nucleotide gated channel 1 (HCN1), a cationic channel whose activity is modulated by, among others, cyclic adenosine monophosphate (cAMP) (Biel et al., 2009).

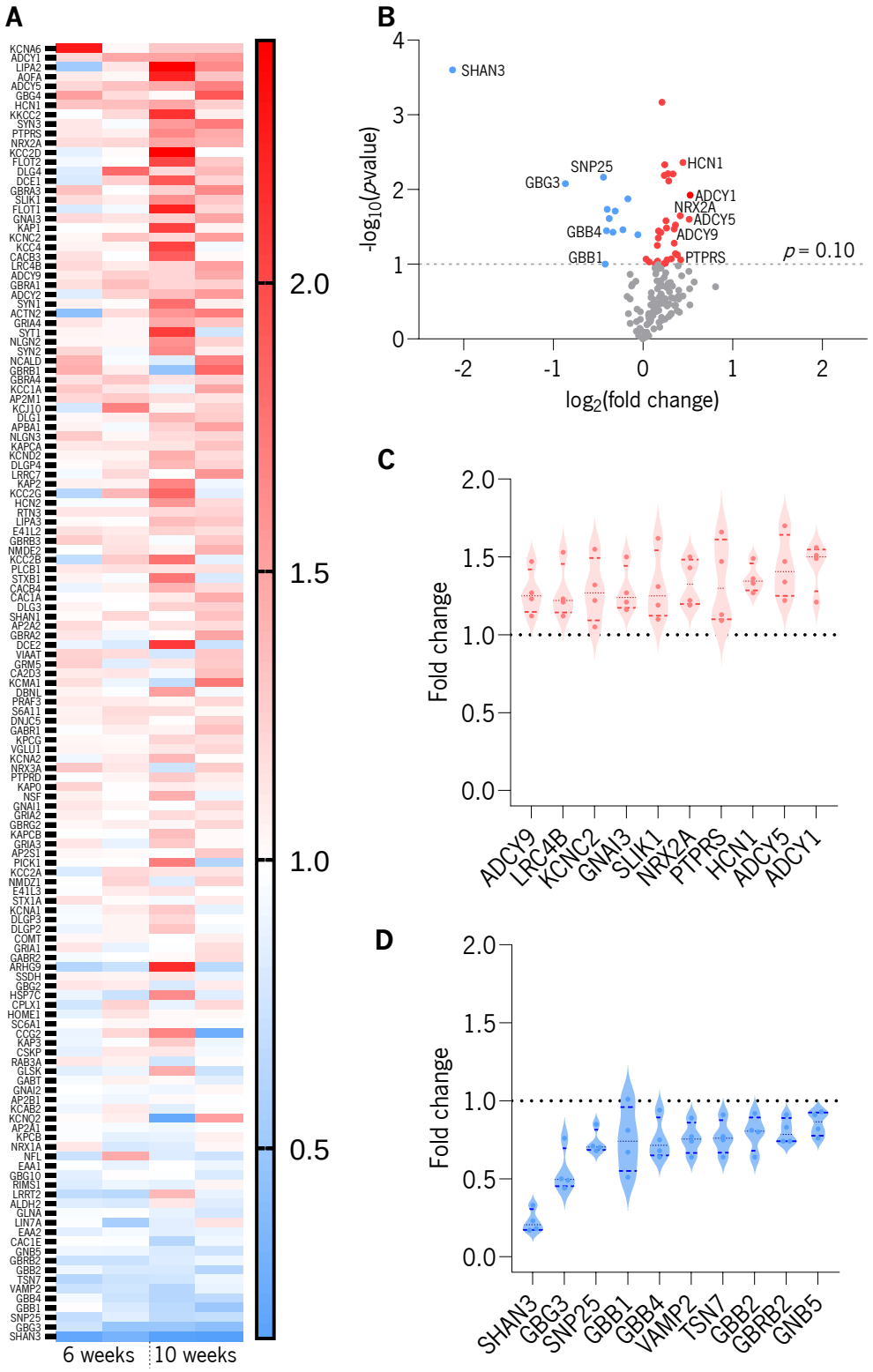

Figure 11. Proteomics screening of primary auditory cortex (A1) from adult *InsG3680*$^{+/+}$ mice.

(A) Heatmap showing all A1 proteins (y-axis) from the "neuronal system" family according to the REACTOME database. Each column represents *InsG3680*$^{+/+}$ protein levels normalized to the WT levels.

Protein fold-enrichment is color coded (blue: decreased expression; red: increased expression relative to control). (B) Volcano plot representing neuronal proteins identified in the proteomics screening. For a level of significance of 0.10, the ten proteins with the biggest fold change difference are depicted in the violin plots (C,D). One-sample Student's *t*-test, n = 4 per genotype (each sample corresponds to A1 tissue combined from 3 mice, aged 6 or 10 weeks).

Interestingly, three different isoforms of adenylate cyclase (ADCY1, ADCY5 and ADCY9) are also among the most upregulated proteins. Knowing that ADCYs catalyze the conversion of ATP (adenosine triphosphate) to cAMP upon activation of G-coupled proteins (Figure 12), these results suggest that the upregulation of this set of proteins might increase the intracellular concentration of cAMP and consequently have an effect on HCN activity, suggesting a strong convergence on this pathway.

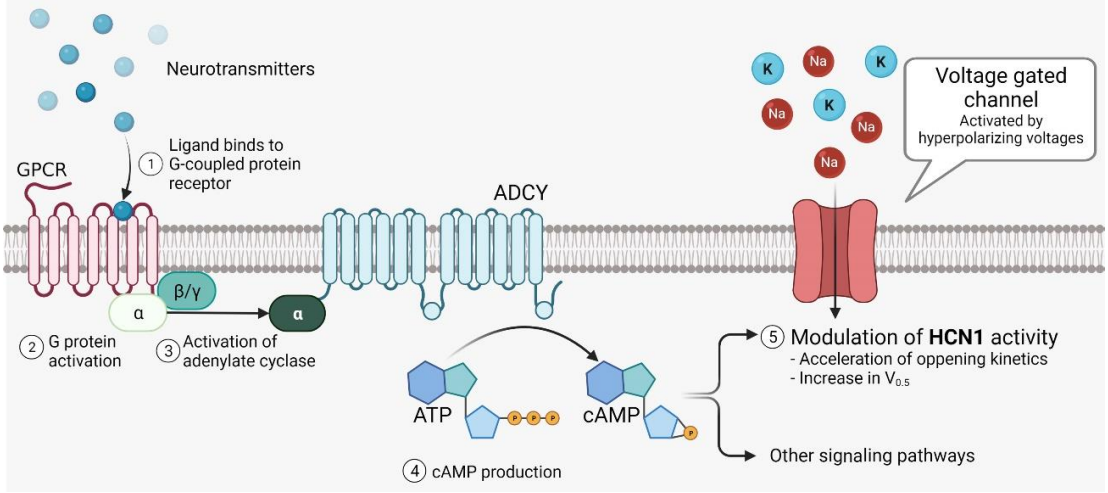

Figure 12. ADCY indirect modulation of HCN activity through cAMP.

The activation of G-coupled protein receptors (GPCRs) leads to the subsequent activation of adenylate cyclase (ADCY) through GPCR subunit α. The ADCY promotes the conversion of ATP to cAMP which is an important secondary messenger in the cell. cAMP also binds to the cyclic nucleotide binding domains of HCN receptors, modulating their activity by accelerating their opening kinetics and producing a positive shift on their half-maximum opening voltage ($V_{0.5}$). Created with Biorender.com

4.4 HCN1 overexpression seems to emerge after P21

Given that ASD is a neurodevelopmental disorder, we wondered whether this HCN1 upregulation could be noticeable before adulthood. During postnatal development, there are time windows known as critical periods of plasticity in which sensory regions (such as A1) present increased plasticity. During these periods, the brain regions associated to sensory processing are very immature and particularly sensitive to any incoming sensory inputs. After that, critical windows close and sensory circuits become less plastic, but more stable, in adulthood. The development/maturation of these regions occurs sequentially in the brain and is highly influenced by the environmental stimulation they receive. In mouse A1 specifically, there are two critical periods of plasticity: one where A1 refines its response to pure tones (usually occurring from postnatal day P12 to P15), and another where A1 refines its response to frequency modulated sweeps (FMS, occurring from P31 to P38) (Nakamura et al., 2020)**.**

Having in mind these different critical periods in mice, we collected A1 samples at four different stages for proteomic analysis: 1) P10, before any critical period begins in A1; 2) P14, during A1 critical period for pure tones; 3) P21, in between A1 critical periods; and 4) P35, during A1 critical period for FMS. From 4132 proteins identified, 2739 were confidently quantified by SWATH-MS. Among those, 155 belonged to neuronal pathways according to the REACTOME database. Relative protein abundance was then normalized to WT levels for all developmental timepoints (Figure 13A) and then the average expression fold-change was statistically compared between WT and *InsG3680*$^{+/+}$ mice (Figure 13B). The five most up and downregulated proteins are represented in Figure 13C and D, respectively. Once again, data revealed that SHANK3 was the top downregulated protein as previously observed in our proteomics dataset from adult animals. HCN1, however, was not significantly upregulated, suggesting that HCN1 overexpression in A1 occurs only in the adult stage rather than during development.

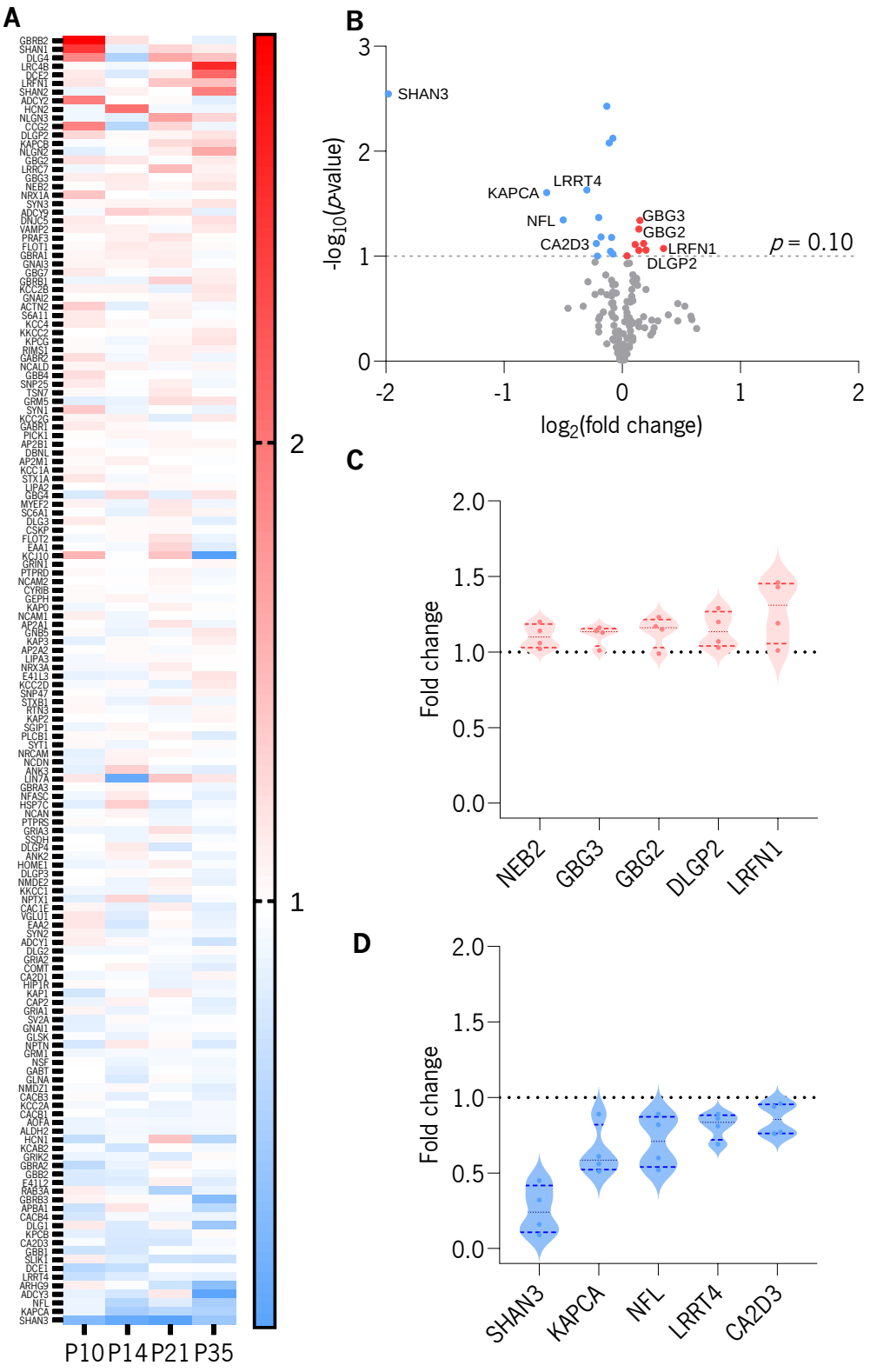

Figure 13. Proteomics screening of primary auditory cortex (A1) from young *InsG3680*$^{+/+}$ mice.

A) Heatmap showing all A1 proteins (y-axis) from the "neuronal system" family according to the REACTOME database. Each column represents *InsG3680*$^{+/+}$ protein levels normalized to the

corresponding WT levels. Protein fold-enrichment is color coded (blue: decreased expression; red: increased expression relative to control). (B) Volcano plot representing neuronal proteins identified in the proteomics screening. For a level of significance of 0.10, the ten proteins with the greatest fold change difference are depicted in the violin plots (C, D). One-sample Student's t-test, n = 1 per group (each sample corresponds to A1 tissue combined from 3 mice, aged 10, 14, 21 or 35 postnatal days).

When plotting together results from all timepoints (adulthood and early development), for both genotypes, HCN1 expression levels seem to gradually increase throughout early development and then stabilize around 6 weeks (Figure 14A). Other neuronal proteins such as SHANK3 and ADCY9, also seem to follow a similar expression curve through development (Figure 14C and E). Notably, from P21 onwards, expression levels of HCN1 and ADCY9 seem to be consistently increased in *InsG3680*$^{+/+}$ mice compared to WT. Both these proteins reach their plateau in adulthood where their expression levels become statistically different between *InsG3680*$^{+/+}$ and WT mice. This suggests that perhaps HCN1 upregulation starts to emerge early during development in *InsG3680*$^{+/+}$ mice but only manifests itself in adulthood. Of note, a sudden decrease in HCN1 and ADCY9 levels can be observed at P35 in the *InsG3680*$^{+/+}$ group. Such decrease seems abnormal and does not fit the overall expression curves. Although this phenomenon is likely due to experimental rather than biological causes, no conclusions can be drawn at this time due to reduced n number.

Lastly, we aimed to confirm our proteomics data by western blot analysis. Since no protocol for HCN1 detection was readily optimized in our lab, we first had to test several experimental conditions to detect HCN1. The first step was to obtain A1 protein homogenates from animals aged P10, P14, P21, P35 and 10 weeks old. Several conditions throughout the multi-step protocol were tested, namely: 1) protein denaturation (or not) before SDS-PAGE; 2) different poly-acrylamide concentrations for the SDS-PAGE gel (8%, 10% or concentration gradient); 3) other variations in the protocol such as wet-transfer vs semidry transfer, washing/blocking buffer stringency (PBS or TBS with vs without tween), blocking buffer composition (5% milk vs 5% milk + 1% NGS), primary antibody dilution (1:500 vs 1:200), and different signal detection methods (fluorescence vs chemiluminescence). The final protocol adopted is described in the methods sections. Nevertheless, it was not possible to obtain HCN1 labeling nor to eliminate some unspecific binding bands. The expected molecular weight for HCN1 is around 100 kDa, however, none of the detected bands were sufficiently close to the 100 kDa region. This fact, together with the absence

of a negative control (such as brain tissue from a HCN1-KO animal) prevents any conclusion from our western blot analysis.

4.5 HCN1 transcripts are increased at P21 in *InsG3680*$^{+/+}$ mice

The HCN family comprises 4 members, which are distributed beyond the central nervous system in regions such as the heart or skeletal muscle (Santoro and Tibbs, 1999). In our proteomics screening, besides HCN1, only HCN2 was detected in A1. This indicates that HCN1 and HCN2 are the main family members expressed in the primary auditory cortex, which is in accordance with previous reports from mice (Moosmang et al., 1999; Santoro et al., 2000) and rats (Monteggia et al., 2000). Contrarily to HCN1, HCN2 levels detected in our proteomics analysis seemed to be quite stable during development and adult stages (Figure 14B). Furthermore, HCN2 levels did not seem to differ between *InsG3680*$^{+/+}$ and WT mice, which suggests that disruption of SHANK3 expression does not affect HCN family members in the same way, being rather specific to HCN1 in A1 region.

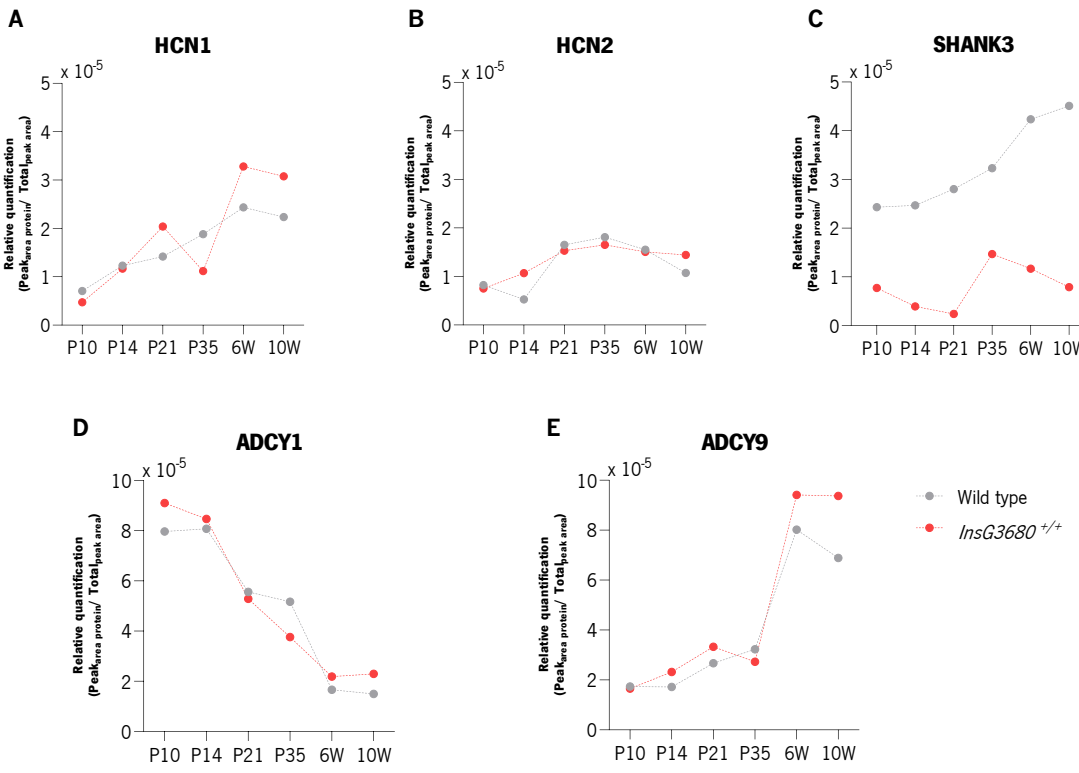

Figure 14. Relative protein expression levels in the primary auditory cortex (A1) of WT controls and *InsG3680*$^{+/+}$ mice throughout development.

Different panels display the relative quantification of hyperpolarization cyclic nucleotide gated channel 1 protein (HCN1; A), HCN2 (B), SHANK3 (C), adenylate cyclase 1 (ADCY1; D) and ADCY9 (E), obtained

from the A1 proteomics screening. n = 1 for samples from postnatal days 10 to 35 (P10-P35), n = 2 for samples of 6 and 10 weeks (6W and 10W); each sample represents a combination of A1 tissue from 3 littermates combined.

To check whether the overexpression of HCN1 protein was also present at the RNA level, we quantified the *mHcn1*, *mHcn2* and *mHcn3* transcripts in the A1 of WT and *InsG3680*$^{+/+}$ mice using real-time quantitative PCR (RT-qPCR). RNA was extracted from A1 samples from animals aged P14, P21 and 10W. The obtained results suggest an increase for both *mHcn1* and *mHcn2* transcripts in *InsG3680*$^{+/+}$ mice across all ages, despite the emergence of statistical significance only at P21 for both HCN transcripts (Figure 15). *Hcn3* was not detected which indicates that this isoform is scarcely expressed, or even totally absent, in A1, confirming previous descriptions from the literature (Schridde et al., 2006).

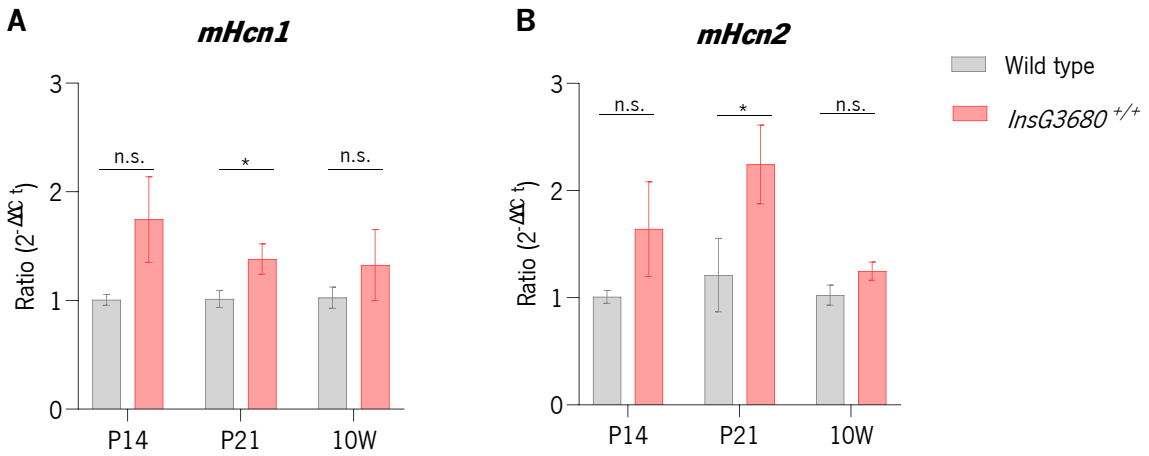

Figure 15. *mHcn1* and *mHcn2* transcripts are overexpressed in *InsG3680*$^{+/+}$ mice.
Relative expression of *mHcn1* and *mHcn2* was assessed through real-time quantitative PCR (RT-qPCR) in A1 samples from WT and *InsG3680*$^{+/+}$ mice. Bar graphs show the relative levels at postnatal days 14, 21 and week 10 (P14, P21, W10). A tendency for increased levels of both *mHcn1* and *mHcn2* can be observed at all ages in *InsG3680*$^{+/+}$ mice. Despite this tendency, statistically significant differences are only detected at P21. Each sample contains A1 tissue from 3 mice combined together. Unpaired Student's *t*-test for all groups, except for comparing the timepoint P21 *mHcn2* where the equivalent non-parametric test was applied (Mann-Whitney test); n = 2 biological replicates and 3 technical replicates. A biological replicate represents a different A1 sample with 3 littermates combined. A technical replicate represents the measurement of the same sample more than once. Data are mean ± SEM; $^{*}p < 0.05$, n.s. not significant.

4.6 *InsG3680*$^{+/+}$ mice have functional alterations in HCN-mediated currents

HCN channels are cationic channels permeable to both K^+ and Na^+ that are open at voltages ≤ -50 mV and mediate hyperpolarization currents (I_h). This quite unique biophysical property enables HCN channels to remain constitutively open at resting membrane potential and to contribute to a more depolarized resting membrane potential. HCN channels also influence both input resistance (R_{in}) and membrane resistance (R_m), thus contributing to regulate neuronal excitability (Robinson and Siegelbaum, 2003; Biel et al., 2009; Shah, 2014). According to the literature, HCN1 and HCN2 are the main HCN family members present in the neocortex (also corroborated by our molecular results in A1). Both members are mainly expressed at dendrites of pyramidal cells where they play an important role in dendritic integration, but also in the soma (cell body) of pyramidal cells as well as interneuron GABAergic basket cells (Shah, 2014).

Given that HCN channels influence the R_m of the cell (Wahl-Schott and Biel, 2009), we first asked if its overexpression in *InsG3680*$^{+/+}$ mice would have a functional impact on R_m values. To answer this question, we performed *ex vivo* patch clamp electrophysiology recordings in A1 region from *InsG3680*$^{+/+}$ and WT mice. In order to be able to study HCN currents, we used ZD7288, a selective HCN blocker. Baseline recordings revealed no differences between average R_m values in *InsG3680*$^{+/+}$ and WT mice (Figure 16A). However, after incubation with ZD7288, a greater decrease in R_m was observed in *InsG3680*$^{+/+}$ mice (although not statistically significant) (Figure 16B). Given that HCN channels are constitutively open at the holding potential used in our experiments (-70 mV), we expected their blockade (ZD7288 condition) to increase cellular R_m (because the inward K^+/Na^+ current they mediate would no longer be influencing the R_m of the cell). However, it is worth noting that, despite the decrease we observed in R_m value, this decrease reflects the average value for the whole population of cells. Notably, some cells increased their R_m value upon ZD7288 incubation, whereas others decreased, indicating some heterogeneity in the way that cells responded to HCN blockade.

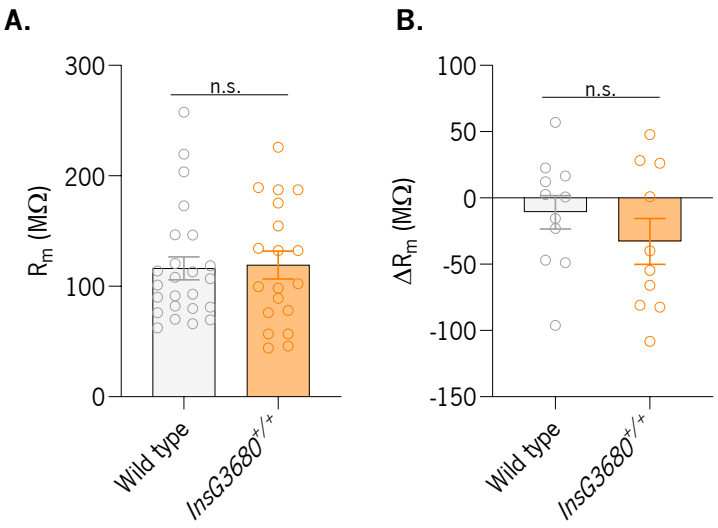

Figure 16. Membrane resistance from WT and *InsG3680*$^{+/+}$ neurons in A1 region.

Average membrane resistance (R_m) recorded was similar between wild type (WT) and *InsG3680*$^{+/+}$ neurons (A). Blockade of HCN channels with ZD7288 seems to have a greater impact on the R_m of *InsG3680*$^{+/+}$ neurons [$\Delta R_m = R_m(ZD7288) - R_m(Control)$], but this difference did not reach statistical significance. (A) Mann-Whitney test, WT: n = 24 neurons, *InsG3680*$^{+/+}$: n = 19 neurons; (B) Student's unpaired *t*-test, WT: n=11 neurons, *InsG3680*$^{+/+}$: n= 10 neurons. Data are mean ± SEM; n.s. not significant. WT: N = 6, *InsG3680*$^{+/+}$: N = 4 mice (males, 7-10 weeks old).

Besides HCN1 overexpression in *InsG3680*$^{+/+}$ mice, our data also revealed a concomitant overexpression of ADCY1, 5, and 9, which could result in higher levels of cAMP because ADCY are catalysts for the conversion of ATP to cAMP (Visel et al., 2006). Given that HCN1 and HCN2 are directly modulated by cAMP (which accelerates HCN opening kinetics and induces positive shifts in their activation curves (Wahl-Schott and Biel, 2009)), we hypothesized that A1 neurons in *InsG3680*$^{+/+}$ mice could present increased hyperpolarization currents (I_h) and an accelerated opening kinetics compared to WT. To test this hypothesis, we used a voltage clamp (V_c) electrophysiology protocol to elicit HCN opening (Figure 17A) in A1 cells. We first recorded I_h currents in baseline conditions (*Figure 17*B) and then proceeded to block HCN channels with ZD7288 (Figure 17C). HCN-mediated currents (also known as I_h) were then determined by subtracting ZD7288 traces from baseline traces (Figure 17D).

First, we measured the effect of ZD7288 incubation on steady-state current (I_{ss}) density. For both genotypes, ZD7288 incubation significantly decreased I_{ss} values (Figure 17F), which demonstrates that A1 cells are sensitive to ZD7288 and, hence, express functional HCN channels.

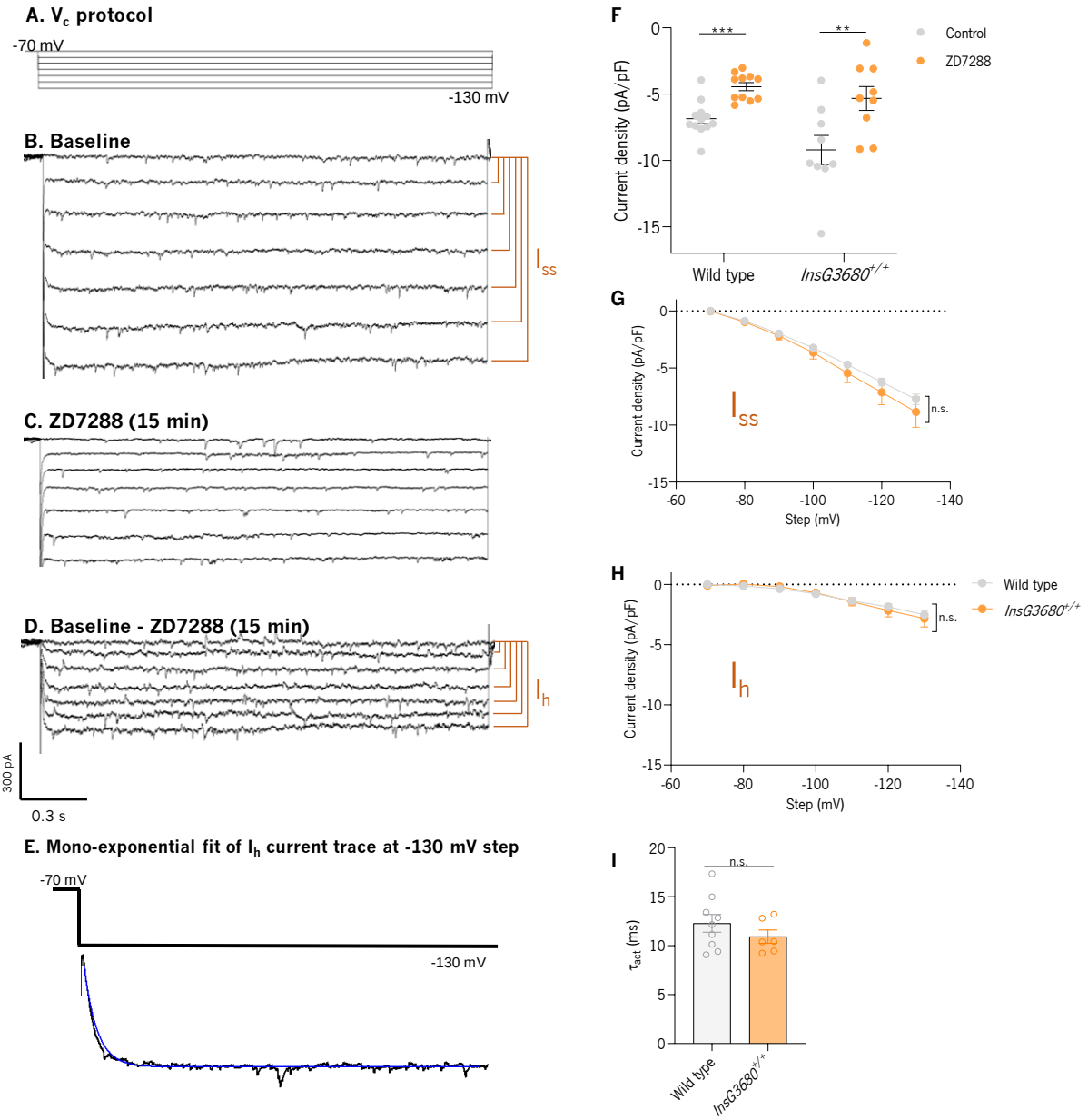

Figure 17. HCN-mediated currents from WT and *InsG3680*$^{+/+}$ neurons in A1 region.

A) Voltage-clamp (V_c) protocol applied in whole-cell mode. From a holding voltage of -70 mV, successive 2-second hyperpolarizing voltage steps were applied in 10 mV intervals until -130 mV. B) Representative traces of current response to the V_c applied in baseline conditions. C) Representative traces of current response to the V_c applied after 15 minutes incubation with 10 µM ZD7288 (HCN blocker). D) Representative traces of HCN-mediated currents obtained by subtracting the ZD7288 traces to the baseline traces. The steady state current (I_{ss}) and hyperpolarization current (I_h) are measured at the end of sweep, when the current response to each voltage step stabilizes. E) Mono-exponential fit in the initial milliseconds of the I_h response to a -130 mV step to obtain the respective activation kinetics. F) ZD7288 incubation for 15 minutes significantly decreases baseline I_{ss} current density, both in WT and *InsG3680*$^{+/+}$

neurons. G, H) Current-voltage (I-V) curves representing I_{ss} (G) and I_h (H) current densities in WT and *InsG3680*$^{+/+}$ neurons. No significant differences were found between groups. I) The activation time constant of *InsG3680*$^{+/+}$ neurons seems slightly faster in comparison to WT neurons, although not statistically significant. (F) Student's paired *t*-test, WT: n=11, *InsG3680*$^{+/+}$: n= 9; (G) Mixed-effects ANOVA, WT: n = 22, *InsG3680*$^{+/+}$ = 16; (H) Mixed-effects ANOVA, WT: n = 13, *InsG3680*$^{+/+}$ = 10; (I) Student's unpaired *t*-test, WT: n = 9, *InsG3680*$^{+/+}$ = 6. Data are mean ± SEM; $^{**}p<0.01$, $^{***}p<0.001$, n.s.: not significant. WT: N = 6, *InsG3680*$^{+/+}$: N = 4 mice (males, 7-10 weeks old).

Next, we asked if there were any differences regarding current density values between genotypes. Since there is an HCN1 upregulation in the A1 of *InsG3680*$^{+/+}$ mice, we would expect to observe a greater current density in response to hyperpolarizing voltage steps in this group. However, there was no significant effect of genotype explaining the variance observed in the I-V curve for I_{ss} current density (baseline conditions; Figure 17G) nor at I_h current density (Figure 17H).

Finally, to assess I_h decay time constant (τ_{act}), we fitted a standard mono-exponential function to the initial segment of the -130 mV step (Figure 17I). No significant differences were found between genotypes, suggesting that I_h activation kinetics is similar between genotypes.

There is a great variety of neuronal cell types in the neocortex with very different biophysical properties. These cells can be mainly classified into principal cells (cortical pyramidal neurons) and interneurons (Figure 18A). The principal cells are large glutamatergic neurons that send excitatory signals to different brain regions, whereas the interneurons are smaller GABAergic cells that inhibit the activity of local principal cells (Tremblay et al., 2016). Although interneurons can be divided into several classes depending on biophysical, morphological, and molecular characteristics, all interneurons tend to be very distinct from principal cells due to their smaller size and typically faster membrane time constant (τ_{memb}) (Tremblay et al., 2016). It is already reported that I_h dynamics between principal neurons and PV$^+$-interneurons shifts throughout mouse brain development (Yang et al., 2018), so we next asked whether this dynamics could be altered in *InsG3680*$^{+/+}$ mice.

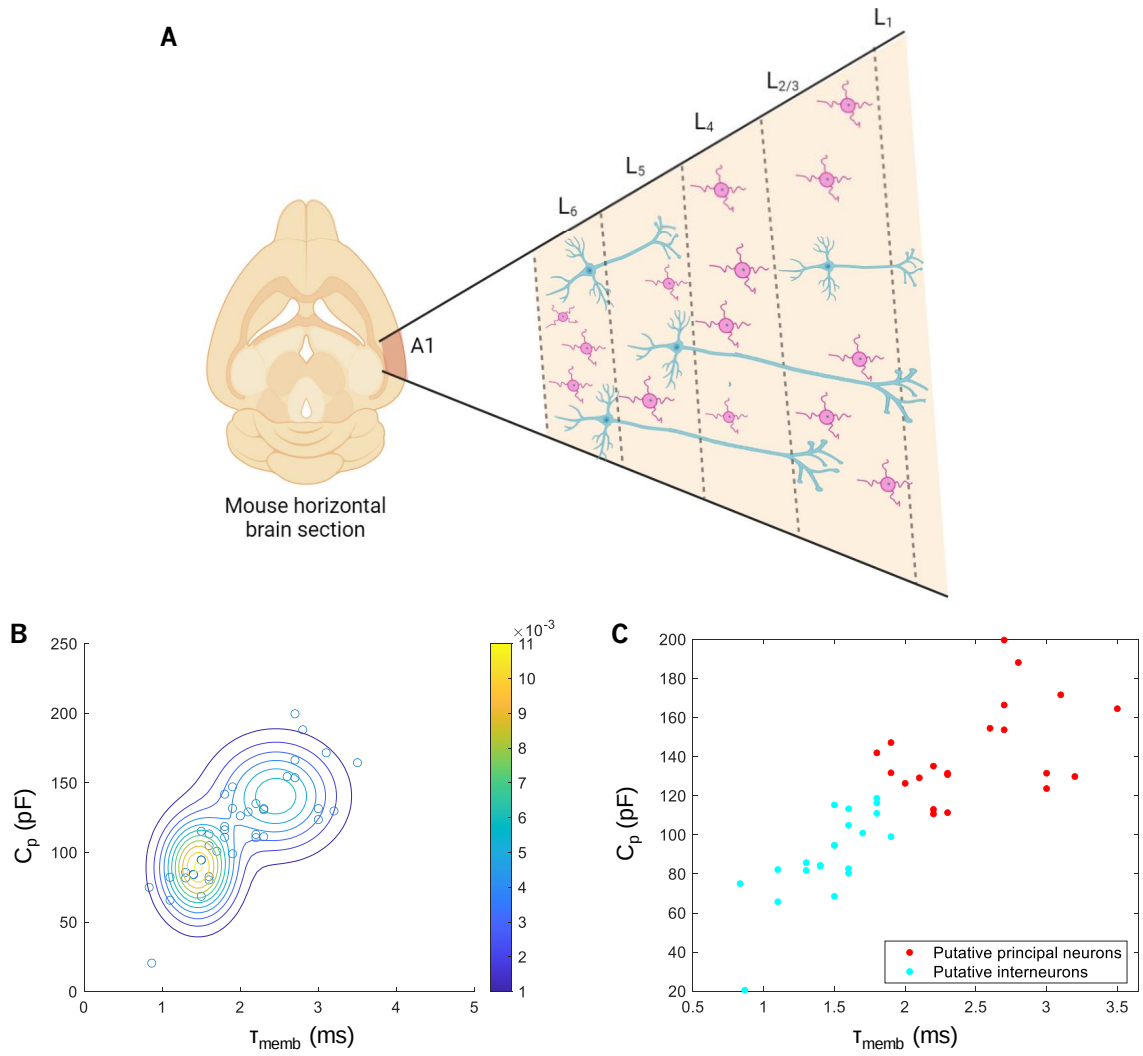

Figure 18. Clustering with Gaussian Mixture Model (GMM) of all the cells recorded in A1.

A) Schematic representation of cortical layers (L_1 to L_6) in A1 region and layer-specific distribution of neuronal cell types. Principal neurons (mainly cortical pyramidal cells) are represented in blue and cortical interneurons are represented in pink. B) Gaussian Mixture Model (GMM) was used for unsupervised clustering of all recorded cells according to their membrane time constant (τ_{memb}) and capacitance (C_p) values. The lines represent the contour of the probability density function from the GMM and are color-coded (blue and yellow represent, respectively, low or high probability of belonging to each cluster). C) The same data as represented in B with the final cluster classification: blue dots represent putative interneurons and red dots represent putative principal neurons. Panel A created with Biorender.com.

Given that principal neurons present higher τ_{memb} and C_p and the opposite is true for interneurons, we used these two properties to plot all our recorded cells and then used a Gaussian Mixture Model (GMM) to perform clustering analysis. GMM is a clustering method based on the probability of each point belonging to a certain gaussian distribution. As expected, GMM analysis revealed two main clusters of cells: one with faster τ_{memb} and smaller C_p (consistent with characteristics described for interneurons and, hence, further classified by us as putative interneurons), and another with higher τ_{memb} and C_p (further classified as putative principal neurons (Figure 18B)). The contour of the probability density function for the GMM is represented in Figure 18C and gives the relative likelihood for each datapoint to belong to the cluster. Next, we repeated all electrophysiological analysis as before, but now considering the two putative cell types as classified by GMM clustering. In baseline conditions, there were no statistically significant differences in the R_m explained by the genotype for any of the two cell types (Figure 19A). Nonetheless, *InsG3680*$^{+/+}$ putative interneurons seemed to have decreased R_m in comparison to WT and the opposite appeared to occur for the putative principal neurons. The effect of HCN blockade by ZD7288 in the R_m also seemed more pronounced in *InsG3680*$^{+/+}$ putative interneurons, but again without any statistical differences (Figure 19B). Such differences, if significant, could indicate that HCN has a cell-type specific impact on R_m.

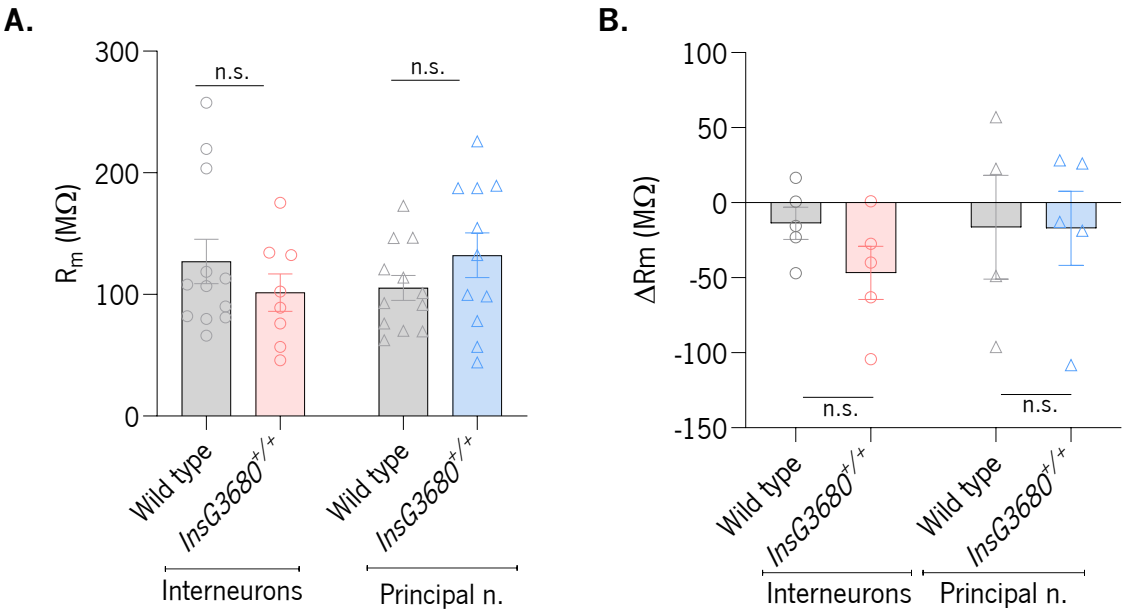

Figure 19. Membrane resistance from WT and *InsG3680*$^{+/+}$ A1 neurons according to cell-type.

A) Average membrane resistance (R_m) is not different between wild type (WT) and *InsG3680*$^{+/+}$ A1 neurons. B) Blocking HCN channels with ZD7288 incubation for 15 minutes seems to have greater impact on the R_m of *InsG3680*$^{+/+}$ putative interneurons but it is not significantly different from WT interneurons. There is no significant effect of the cell type or the genotype on the R_m or ΔR_m. (A) Mixed-effects ANOVA, Interneurons WT: n = 11, *InsG3680*$^{+/+}$: n = 8; Principal neurons WT and *InsG3680*$^{+/+}$: n=12 per group; (B) Mixed-effects ANOVA, Interneurons WT and *InsG3680*$^{+/+}$: n = 5 cells per group, Principal neurons WT: n = 4, *InsG3680*$^{+/+}$: n = 5; Data are mean ± SEM; n.s.: not significant. WT: N = 6, *InsG3680*$^{+/+}$: N = 4 mice (males, 7-10 weeks old).

To assess cell-type specific impact of HCN blockade on I_{ss} current amplitude, we compared baseline currents with currents recorded 15 minutes after ZD7288 incubation. Regarding putative interneurons, we observed a significant decrease in I_{ss} current density for both genotypes, suggesting these cells were sensitive to ZD7288 application. Interestingly, the same did not occur in putative principal neurons. Whereas in the WT group there was a significant decrease in I_{ss} amplitude, the same did not occur for the *InsG3680*$^{+/+}$ group, suggesting a poor modulation of HCN channels in principal neurons after ZD7288 incubation (figure 20A). Notably, I_h currents in *InsG3680*$^{+/+}$ putative principal neurons were significantly decreased as it can be observed in figure 20D (I-V curve). At baseline, neither putative principal neurons (Figure 20C) or interneurons (Figure 20D) showed significant differences associated with the genotype in I_{ss} current density and the variance of I_h in putative interneurons was not explained by the genotype. Overall, this suggests that I_h differences between WT and *InsG3680*$^{+/+}$ mice are cell-type specific, with decreased I_h in A1 principal neurons of *InsG3680*$^{+/+}$ mice.

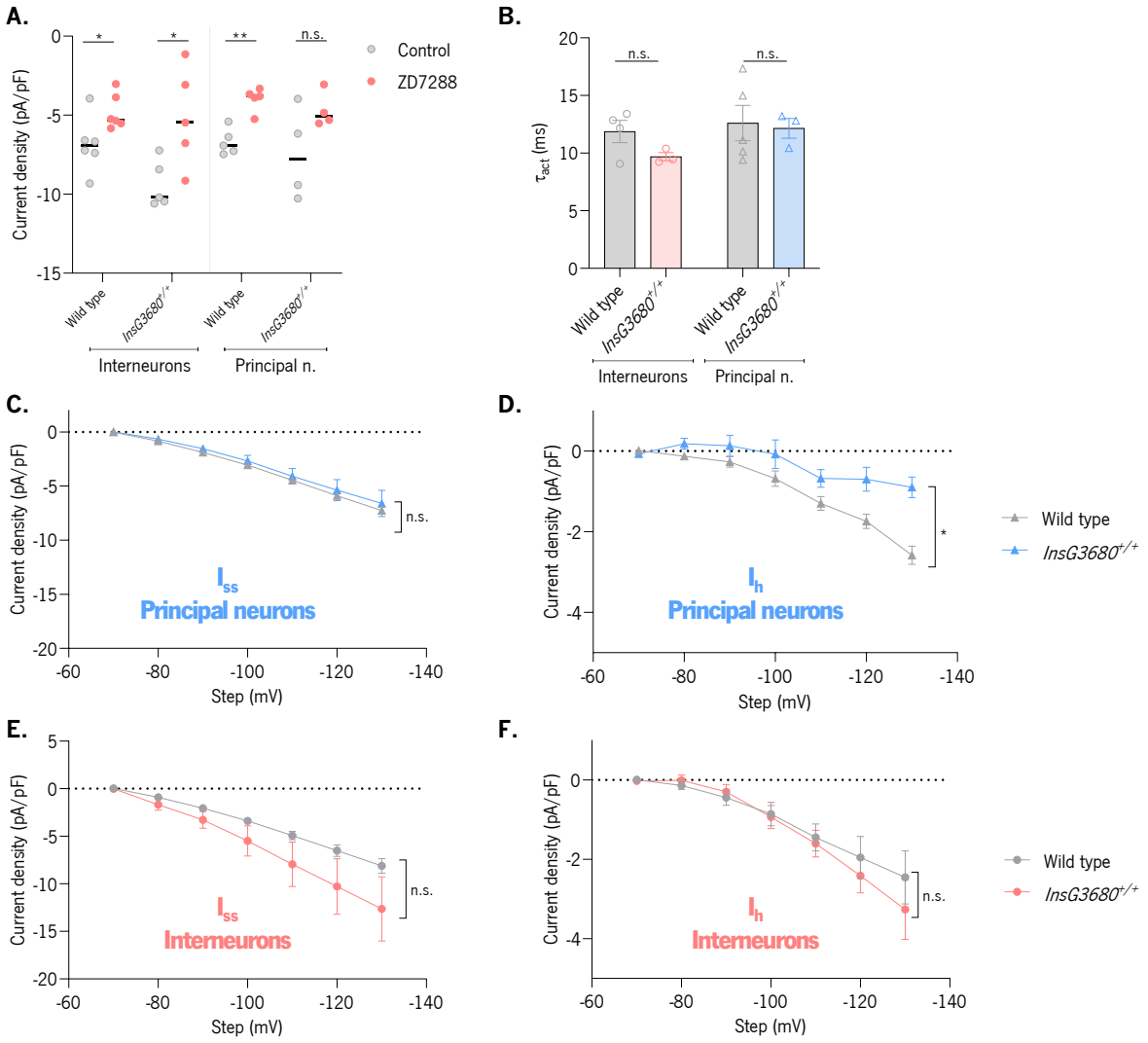

Figure 20. Cell-type specific HCN-mediated currents from WT and *InsG3680*$^{+/+}$ neurons in A1 region.

A) ZD7288 incubation for 15 minutes fails to significantly decrease baseline steady state current (I_{ss}) density in *InsG3680*$^{+/+}$ putative principal neurons. B) Activation time constant (τ_{act}) of *InsG3680*$^{+/+}$ putative interneurons seems faster in comparison to WT, although no statistically significant differences were found for genotype or cell type. C, D) Current-voltage (I-V) curves representing I_{ss} (C) and hyperpolarization current (I_h) (D) densities in WT and *InsG3680*$^{+/+}$ putative principal neurons. The I_h of *InsG3680*$^{+/+}$ putative principal neurons is significantly reduced (D) but no differences were found for the I_{ss} in comparison to WT (C). E, F) Current-voltage (I-V) curves representing I_{ss} (E) and I_h (F) current densities in WT and *InsG3680*$^{+/+}$ putative interneurons. No differences were found between genotypes for I_{ss} or I_h current densities. (A) Paired samples Student's *t*test; Principal neurons WT: n = 6, *InsG3680*$^{+/+}$: n = 5; Interneurons WT: n = 5, *InsG3680*$^{+/+}$: n = 4; (B) Unpaired Student's *t*test; Principal neurons WT: n = 5, *InsG3680*$^{+/+}$: n = 3, Interneurons WT: n = 4, *InsG3680*$^{+/+}$: n = 3; (C-F) Mixed-effects ANOVA with

Bonferroni's *post-hoc* test for multiple comparisons; (C) Principal neurons WT: n = 11, *InsG3680*$^{+/+}$: n = 9; (D) Principal neurons WT: n = 7, *InsG3680*$^{+/+}$ n = 4; (E) Interneurons WT: n = 11, *InsG3680*$^{+/+}$ n = 8; (F) Interneurons WT: n = 6, *InsG3680*$^{+/+}$ n = 5. Data are mean ± SEM, *p<0.05, **p<0.01, n.s. not significant. WT: N = 6, *InsG3680*$^{+/+}$: N = 4 mice (males, 7-10 weeks old).

τ_{act} was not found to be significantly different between genotypes for neither cell types, although *InsG3680*$^{+/+}$ putative interneurons seemed to present a slightly faster τ_{act} in comparison to WT (Figure 20B). In putative principal neurons that putative difference was not so prominent.

5. DISCUSSION

ASD is a complex and multifactorial disorder that manifests itself in several degrees of severity and variety of symptoms. Nonetheless, shared manifestations such as social-communication impairments and repetitive restricted behaviors may share a common pathological mechanism upstream (American Psychiatric Association, 2013).

Sensory abnormalities are present in approximately 90% of individuals with autism (Balasco et al., 2020), being auditory hypersensitivity the most common sensory-perceptual abnormality. One hypothesis in the ASD-field is that ASD impairments in communication might be a consequence of the auditory hypersensitivity observed in patients, where atypical neuronal activity in brain auditory cortex region could underlie the noxious or unpleasant perception of auditory stimuli. For this reason, patients would avoid auditory stimulation, ultimately affecting their learning, communication, and quality of life. As such, in this dissertation, it was our aim to explore potential molecular and functional alterations in the primary auditory cortex region, using a rodent model of ASD. Given the central translational assumption between human and rodents, it was crucial for us to use the best possible animal model that could mimic the human disorder both in terms of its biological origin (construct validity) and behavioral phenotype (face validity). For this reason, we used a transgenic animal model of ASD that carries a patient derived mutation in the *Shank3* gene, the *Shank3-InsG3680*$^{+/+}$ mice. This mutation inserts a single guanine nucleotide (G) at cDNA position 3680, inducing a frameshift mutation that leads to a subsequent stop codon downstream. In order words, this knock-in mouse line leads to a knock-out (KO) of *Shank3*. *Shank3-InsG3680*$^{+/+}$ mice exhibit impaired social interaction, repetitive spontaneous self-grooming behavior, anxiety, and behavioral sensory alterations, being a good animal model of ASD (Zhou et al., 2016). In order to further study the auditory cortex in this animal model, we began by validating their genotype and phenotype in our hands.

Unpublished results from our group, and not described on this dissertation, confirm impaired social interaction in the 3-chamber social test as well as auditory hypersensitivity in *InsG3680*$^{+/+}$ mice. Furthermore, the splash test performed in this dissertation revealed increased self-grooming time in *InsG3680*$^{+/+}$ mice upon spraying a 30% sucrose solution on their fur coat, reflecting perhaps an increased susceptibility to enroll in repetitive behavioral patterns upon triggering. Although the splash test has not been typically used in the autism field to evaluate repetitive behaviors, it is a well-established test to evaluate grooming behavior and to assess depressive-like states and motivation for self-care (Yalcin et al., 2005; Pitzer et al., 2022). Here, we use this approach with the purpose of understanding the impact of introducing an external trigger on mice behavior. The striking differences observed, not only in the time spent grooming but also in the number of grooming bouts, support a phenotype of repetitive behavior

commonly observed in animal models of ASD (as reviewed in the introduction of this dissertation). Moreover, the fact that we introduced here an external trigger for grooming shows that, besides having increased spontaneous grooming behavior (as previously described in the literature), these mice also have increased evoked grooming behavior.

When analyzing behavioral videos collected during the splash test, we noticed that some exploratory and naturalistic behaviors seemed altered in *InsG3680*$^{+/+}$ mice. Upon quantification, we found that rearing behavior, which could be considered as an exploratory behavior (Krüttner et al., 2022) and as an indirect measure of anxiety in rodents (Sturman et al., 2018), was reduced in *InsG3680*$^{+/+}$ mice. This suggests the existence of an anxious phenotype in *InsG3680*$^{+/+}$ mice, corroborating the findings previously published by Zhou et al (Zhou et al., 2016). Furthermore, we also detected reduced / absent digging behavior in *InsG3680*$^{+/+}$ mice. Digging behavior is usually tested through the marble burying test where it is considered a measure of repetitive behavior (Angoa-Pérez et al., 2013). But given that the *InsG3680*$^{+/+}$ mice have increased repetitive behavior (grooming), why not repetitive digging? One possibility is that the splash test has a bigger driving force behind: the sticky sucrose solution makes mice focus on self-grooming for cleaning their fur coat, reducing the overall richness of their behavioral repertoire such as dig, rear, etc. Moreover, the marble burying test uses marbles to evoke digging behavior in rodents, a triggering factor that was absent during the splash test.

After validating the *InsG3680*$^{+/+}$ mouse model of ASD in our hands, we moved on towards our main aim which was to explore potential molecular and functional alterations in the primary auditory cortex region (A1).

Despite not being reported in this dissertation, preliminary data from our lab indicates that *InsG3680*$^{+/+}$ mice display an auditory hypersensitivity behavioral phenotype, which is already a strong indication that molecular and/or functional alterations might be present in their auditory cortex. This was actually first suggested in previous published work with the same animal model where the acoustic thresholds for a startle response were greatly diminished in *InsG3680*$^{+/+}$ mice in comparison to WT controls (Zhou et al., 2016), suggesting an hyperreactive behavior in response to sounds.

To start unveiling potential molecular underpinnings for auditory hypersensitivity in this model, we decided to study molecular signatures in A1, a brain region that is crucial to the processing of auditory stimuli. Using an unbiased proteomics approach, we found a large set of neuronal proteins that displayed altered expression levels in adult *InsG3680*$^{+/+}$ male mice. Notably, there was a strong functional convergence between some of the most upregulated proteins: the HCN1 channel and ADCY1, 5 and 9 proteins. ADCYs are catalysts for the conversion of ATP to cAMP (Visel et al., 2006), while HCN1 is a

cationic channel whose activity can be modulated by cAMP (Wahl-Schott and Biel, 2009). Such finding indicates that SHANK3 absence, somehow, affects this pathway. Surprisingly, the SHANK3 protein has been shown to directly bind to HCN channels and to have a general function in scaffolding HCN channels at the cell surface (Yi et al., 2016). One possibility is that lack of SHANK3 leads to unstable tethering of HCN channels, compromising their function and hence triggering a compensation mechanism of HCN upregulation, both by its overexpression as well as upregulation of the cAMP pathway, in an attempt to restore HCN function.

Given that ASD is a neurodevelopmental disorder, we also investigated A1 proteome during postnatal development but found fewer proteins significantly altered in young *versus* adult *InsG3680*$^{+/+}$ mice. Of note, and contrarily to the adulthood dataset, HCN1 expression was not found to be increased in young *InsG3680*$^{+/+}$ mice. Such observation could in fact support our hypothesis that HCN1 upregulation may be a compensation mechanism due to the loss of SHANK3. Given that SHANK3 expression is known to increase after P21 and peak only after P35 (Wang et al., 2014), it is perhaps not surprising that HCN1 upregulation only occurs after that timepoint because it is being triggered by the absence of SHANK3 at P35, a timepoint where SHANK3 presence was expected at the synapse. In fact, our proteomic results show a sudden and abrupt decrease of HCN1 levels at P35 (Figure 14A). Although one possible explanation is an experimental error that can only be ruled out by replicating such experiment, another possibility is that the sudden absence of SHANK3 at P35 (a timepoint where its expression should peak), leads to an abrupt reduction of HCN1 levels, hence triggering a long-term compensation mechanism of HCN1 upregulation. Repeating the quantification of HCN1 expression levels at several neurodevelopmental timepoints would be crucial to solve this question. Given that proteomics is a powerful but expensive technique to apply in this context, we pursued other molecular biology techniques to tackle the same question: how does the expression of HCN1 evolve across time? The first approach tested was western blot analysis which unfortunately failed, probably due to poor affinity of the primary antibody. Alternatively, we looked to *mHcn1* transcript levels along development using real-time quantitative PCR (RT-qPCR). Although not answering exactly the same question (changes in RNA level do not necessarily translate into changes at the protein level), this experiment allowed us to assess whether the overexpression of HCN1 protein was also present at the RNA level.

Somehow in agreement with the idea that subtle genotype differences in HCN1 expression may start around P21, our RT-qPCR results clearly indicate increased levels of *mHcn1* transcript in the A1 at P21. In fact, the remaining timepoints tested also show a clear tendency (although not statistically significant) for increased *mHcn1*, although with higher experimental variability. The same phenomenon

was observed for *mHcn2*, the transcript for HCN2 channel that is also expressed in the neocortex. However, unlike HCN1 protein, HCN2 expression does not seem to follow the profile of increased transcript levels. Together this data suggests P21 as a crucial age for HCN dynamics in A1 and indicate that post-transcriptional regulation mechanisms likely play a key role in regulating the expression of different HCNs.

HCN channels are responsible for mediating hyperpolarization currents (I_h) which were first observed in motorneurons and later in the heart by Noma and Irisawa (Noma and Irisawa, 1976; Bender and Baram, 2008). HCN1 channels are, together with HCN2, the main I_h currents facilitators in the neocortex (Shah, 2014). Given the increase in HCN1 expression in *InsG3680*$^{+/+}$ adult mice, we expected to observe also a change in I_h currents in the neurons of A1. However, upon application of hyperpolarizing voltage steps in A1 neurons, no differences were observed between genotypes (neither in baseline I_{ss} or in I_h). However, several explanations are possible for this observation.

Our recordings were performed in neurons of deeper layers (around layer 4 to 6) of the A1, where we would expect greater HCN1 expression, especially in pyramidal neurons from layer 5 (Santoro et al., 2000). However, the expression pattern of HCN1 does not only vary depending on the cortical layer, but also at the cellular sub compartmental level. Observations both in rats and mice show that, in pyramidal neurons, HCN1 is mostly expressed at distal apical dendrites that expand from layer 5 until layer 1, where they co-localize with HCN2. Their abundance reduces gradually near the soma, where they are much less expressed (Lörincz et al., 2002; Notomi and Shigemoto, 2004). In other cell types, such as GABAergic inhibitory interneurons, HCN1, 2 and 4 seem to be further expressed in pre-synaptic terminals, especially in parvalbumin-expressing interneurons from layers 5-6. Here, HCN channels play an important regulatory role for GABA release from the GABAergic terminals through increasing Ca^{2+} influx by T-type Ca^{2+} channels (Cai et al., 2022). Since all our recordings were performed solely at the soma, we are probably not fully detecting I_h currents in more distal dendritic regions due to filtering effects and spatial clamping limitations, especially in pyramidal neurons. Hence, not only I_h currents at the soma may differ significantly depending on cell type but potential differences in HCN1 function may not be readily detectable among genotypes due to its distal expression at dendrites.

Accordingly, and since the properties of the recorded cells varied considerably, we performed unsupervised clustering of our recorded cells based on their C_p and τ_{memb} values into two main classes: putative principal neurons and putative interneurons. Interestingly, certain differences emerged, especially regarding putative principal neurons in *InsG3680*$^{+/+}$ mice. I_h current density was decreased in this group, suggesting a decrease in functional HCN1 expression in these cells. Consistently, putative

principal neurons in *InsG3680*$^{+/+}$ mice were not sensitive to HCN blockade: their R_m and their current density in response to hyperpolarization were not affected by ZD7288 incubation. Such observations seem to add to our previous picture of what is happening downstream of SHANK3 absence at the synapse: HCN1 are not being properly scaffold at the synapse leading to decrease HCN1 function (reduced I_h current density) and triggering overexpression of HCN1 as a compensation mechanism that tries to normalized the lack of proper HCN1 function.

Regarding putative interneurons, we do not observe significant changes in any of the parameters studied. However, there are certain data trends that suggest I_h-related alterations in this cell population. The R_m of putative interneurons is slightly smaller in *InsG3680*$^{+/+}$ mice, and R_m change upon HCN blockade is greater than in WT. In both genotypes, HCN blockade significantly impacted I_{ss} current density, indicating that these cells express HCN channels. Despite not observing genotype differences, we cannot assure that they do not exist, not only because of spatial clamping issues discussed above but also because of our small sample size. Nonetheless, our data does suggest that I_h differences between WT and *InsG3680*$^{+/+}$ mice are cell-type specific.

Of note, it is worth to mention a developmental study in the medial prefrontal cortex showing that I_h dynamics strongly change throughout postnatal development and are cell-type specific. The I_h in pyramidal neurons increases from juveniles (P16-P21) to adolescence (P35-P40) and stabilizes in adulthood (around 10 weeks), whereas Ih in PV$^+$-interneurons displays the opposite tendency (Yang et al., 2018). This is consistent with the HCN1 expression pattern we observe in the A1 proteomic analysis of our WT mice (assuming, of course, that HCN1 increase in protein expression translates into increased I_h currents in "normal" WT mice). However, in our *InsG3680*$^{+/+}$ mice we observed an even greater HCN1 increase that did not translate into increased I_h currents. In fact, we see the opposite, a cell-type specific decrease of I_h in putative principal neurons. This suggests that, at some point in development, the increase in I_h that was supposed to happen in principal neurons failed to occur and could be triggering HCN1 overexpression as a compensation mechanism that is trying to restore normal levels of I_h currents.

At the same time, we did not detect an impact on interneurons' I_h currents. Nevertheless, it is worth mentioning that, despite medial prefrontal cortex and A1 being both neocortical regions, there is no way to guarantee that I_h matures in the same way in both regions, making it difficult to extrapolate conclusions between prefrontal cortex and A1. However, given that no studies are yet available in A1 specifically, comparisons within the neocortex are perhaps the best option available. Given that SHANK3 is a protein highly expressed in cortical pyramidal neurons, one possible explanation is that the lack of SHANK3 is

having a preferential detrimental effect in I_h currents in this cell type rather than affecting I_h currents in interneurons.

Despite scarce, there are already some studies relating SHANK3 deficiency and HCN channelopathy. Recently some authors reported that SHANK3 absence, or deficiency, impairs I_h in several regions such as the ventrobasal complex (VB) in the thalamus (Zhu et al., 2018), and the hippocampus (Lee et al., 2020). Both studies report decreased resting membrane potential, increased neuronal excitability, and increased input resistance (Zhu et al., 2018; Lee et al., 2020) as the main functional consequences. Earlier, in 2016, Yi and colleagues first reported that SHANK3 absence impacts HCN dynamics in both human neuronal cell lines and mouse hippocampal cell lines. They found SHANK3 absence to be associated with decreased I_h and HCN expression levels in cultured neurons. This had an impact on neuronal intrinsic electrical properties, such as increased input resistance and resting membrane potential, consistent with an also described increased neuronal excitability profile (Yi et al., 2016). In our work, we observe a general increase in HCN1 levels, but a decreased I_h in putative principal neurons in adult *InsG3680*$^{+/+}$ mice. Despite seemingly controversial at first, it is important to keep in mind that *in vivo* cortical circuitry is a much more complex system than cell cultured neurons, where feedback/compensatory mechanisms can occur. Hence, our detected increase in HCN1 protein expression might reflect an *in vivo* compensation mechanism that fails to occur *in vitro*, however, both share the same underlying cause: decreased functional I_h currents.

In summary, SHANK3 interacts with HCN channels and this interaction seems crucial for the tethering of HCN in the cell membrane and to generate normal I_h currents (Yi et al., 2016). Given that SHANK3 is highly expressed in cortical pyramidal neurons, its absence could underlie the failure of principal neurons in gradually increasing I_h currents during development in *InsG3680*$^{+/+}$ mice, which could explain why I_h is decreased in these mice. In future work, it would be interesting to study how I_h currents evolve through postnatal development in a cell-type specific manner, and when exactly I_h currents start to diverge between WT and *InsG3680*$^{+/+}$ mice, specifically in A1 brain region.

Limitations

The A1 of the mouse is a quite small region of the brain. This is an experimental limitation in several aspects. For molecular biology assays, such as neuroproteomics and RT-qPCR performed in this dissertation, the combination of A1 tissue from 3 different mice is always required to obtain sufficient amount of protein or RNA extracts. This increases experimental complexity (having age matched synchronized animals to combine) and possibly also experimental variability. Furthermore, the high

number of experimental animals required also imposes some limitations in performing biological replicates. For patch clamp experiments, this is also limiting, since only a limited number of slices (usually 2 to 3) will contain the region of interest for A1 recordings and only two cells per slice (one from each brain hemisphere) can undergo the whole protocol with HCN blockade, due to drug incubation.

Regarding western blot experiments, we were not able to obtain satisfactory results. Despite testing several experimental conditions, the antibody binding did not seem to be sufficiently specific. In some attempts, a signal was detected near the molecular weight of 100 kDa, but we could not be confidently sure that we were detecting HCN1 because we did not have a proper negative control, such as brain tissue from a HCN1-KO mouse.

Lastly, clustering of patched cells based on their C_p and τ_{memb} allowed the identification of two putative cell populations and revealed the possibility that I_h alterations might be cell-type specific. However, clustering is not the ideal method to evaluate this. SHANK3 absence and HCN1 alterations could themselves affect C_p and τ_{memb} values, respectively, which would then bias the clustering (Robinson and Siegelbaum, 2003). Hence, to reach cell-type conclusions, it would be better to use transgenic mouse lines expressing fluorescent markers under cell-type specific promoters for principal neurons and interneurons (Murphey et al., 2014).

6. Future perspectives

This dissertation represents the initial steps on a better understanding of the auditory cortex in the *InsG3680*$^{+/+}$ model of ASD and proposes HCN1 as a promising molecular target in ASD. In the future, it is important to better dissect the mechanistic link between behavioral auditory hypersensitivity and HCN1. It would be exciting to test whether HCN1 manipulation in A1 can modulate the behavioral auditory hypersensitivity phenotype in *InsG3680*$^{+/+}$ mice.

Regarding our electrophysiology approach, it would be important to assess intrinsic cell properties such as resting membrane potential, input resistance, and neuronal excitability, as well as the impact of HCN blockade on those parameters because they are known to be influenced by I_h (Biel et al., 2009) and known to be altered in *Shank3* mutant mice (Zhu et al., 2018; Lee et al., 2020). Given that I_h regulates excitatory synaptic release in regions such as the entorhinal cortex and hippocampus (Shah, 2014), it would also be useful to evaluate excitation, inhibition, and E/I ratio, in the A1 region, in developing and adult mice. Furthermore, because HCN activity is also influenced by other channels present in its vicinity (Shah, 2014; Zhu et al., 2018), addressing excitatory and inhibitory post-synaptic currents would be important to understand if HCN plays the same E/I regulatory role in A1 as in other regions of the brain.

Further understanding the role of HCN1 in the developing auditory cortex of *InsG3680*$^{+/+}$ mice might better elucidate the mechanisms underlying abnormal auditory sensitivity in ASD and perhaps help uncover future therapeutic approaches.

REFERENCES

American Psychiatric Association (2013). *Diagnostic and Statistical Manual of Mental Disorders*. American Psychiatric Association doi:10.1176/appi.books.9780890425596.

Angoa-Pérez, M., Kane, M. J., Briggs, D. I., Francescutti, D. M., and Kuhn, D. M. (2013). Marble Burying and Nestlet Shredding as Tests of Repetitive, Compulsive-like Behaviors in Mice. *J. Vis. Exp.* doi:10.3791/50978.

Anomal, R. F., Villers-Sidani, E. De, Brandão, J. A., Diniz, R., Costa, M. R., and Romcy-Pereira, R. N. (2015). Impaired processing in the primary auditory cortex of an animal model of autism. *Front. Syst. Neurosci.* 9, 1–12. doi:10.3389/fnsys.2015.00158.

Arndt, T. L., Stodgell, C. J., and Rodier, P. M. (2005). The teratology of autism. *Int. J. Dev. Neurosci.* 23, 189–199. doi:10.1016/j.ijdevneu.2004.11.001.

Auerbach, B. D., Manohar, S., Radziwon, K., and Salvi, R. (2021). Auditory hypersensitivity and processing deficits in a rat model of fragile X syndrome. *Neurobiol. Dis.* 161, 105541. doi:10.1016/j.nbd.2021.105541.

Balaan, C., Corley, M. J., Eulalio, T., Leite-ahyo, K., Pang, A. P. S., Fang, R., et al. (2019). Juvenile Shank3b deficient mice present with behavioral phenotype relevant to autism spectrum disorder. *Behav. Brain Res.* 356, 137–147. doi:10.1016/j.bbr.2018.08.005.

Balasco, L., Provenzano, G., and Bozzi, Y. (2020). Sensory Abnormalities in Autism Spectrum Disorders: A Focus on the Tactile Domain, From Genetic Mouse Models to the Clinic. *Front. Psychiatry* 10. doi:10.3389/fpsyt.2019.01016.

Bassell, G. J., and Warren, S. T. (2008). Fragile X Syndrome: Loss of Local mRNA Regulation Alters Synaptic Development and Function. *Neuron* 60, 201–214. doi:10.1016/j.neuron.2008.10.004.

Bender, R. A., and Baram, T. Z. (2008). Hyperpolarization activated cyclic-nucleotide gated (HCN) channels in developing neuronal networks. *Prog. Neurobiol.* 86, 129–140. doi:10.1016/j.pneurobio.2008.09.007.

Betancur, C. (2011). Etiological heterogeneity in autism spectrum disorders: More than 100 genetic and genomic disorders and still counting. *Brain Res.* 1380, 42–77. doi:10.1016/j.brainres.2010.11.078.

Biel, M., Wahl-Schott, C., Michalakis, S., and Zong, X. (2009). Hyperpolarization-Activated Cation Channels: From Genes to Function. *Physiol. Rev.* 89, 847–885. doi:10.1152/physrev.00029.2008.

Bozdagi, O., Sakurai, T., Papapetrou, D., Wang, X., Dickstein, D. L., Takahashi, N., et al. (2010). Haploinsufficiency of the autism-associated Shank3 gene leads to deficits in synaptic function, social

interaction, and social communication. *Mol. Autism* 1, 15. doi:10.1186/2040-2392-1-15.

Brand, B. A., Blesson, A. E., and Smith-Hicks, C. L. (2021). The impact of x-chromosome inactivation on phenotypic expression of x-linked neurodevelopmental disorders. *Brain Sci.* 11. doi:10.3390/brainsci11070904.

Braun, K., and Segal, M. (2000). FMRP involvement in formation of synapses among cultured hippocampal neurons. *Cereb. Cortex* 10, 1045–1052. doi:10.1093/cercor/10.10.1045.

Brunner, D., Kabitzke, P., He, D., Cox, K., Thiede, L., Hanania, T., et al. (2015). Comprehensive analysis of the 16p11.2 deletion and null cntnap2 mouse models of autism spectrum disorder. *PLoS One* 10, 1–39. doi:10.1371/journal.pone.0134572.

Burd, L., Severud, R., Kerbeshian, J., and Klug, M. G. (1999). Prenatal and perinatal risk factors for autism. *J. Perinat. Med.* 27, 1311–1321. doi:10.1515/JPM.1999.059.

Cai, W., Liu, S.-S., Li, B.-M., and Zhang, X.-H. (2022). Presynaptic HCN channels constrain GABAergic synaptic transmission in pyramidal cells of the medial prefrontal cortex. *Biol. Open* 11. doi:10.1242/bio.058840.

Castro, A. C., and Monteiro, P. (2022). Auditory Dysfunction in Animal Models of Autism Spectrum Disorder. *Front. Mol. Neurosci.* 15. doi:10.3389/fnmol.2022.845155.

Chen, L., Li, X., Tjia, M., and Thapliyal, S. (2022). Homeostatic plasticity and excitation-inhibition balance: The good, the bad, and the ugly. *Curr. Opin. Neurobiol.* 75, 102553. doi:10.1016/j.conb.2022.102553.

Chen, L., and Toth, M. (2001). Fragile X mice develop sensory hyperreactivity to auditory stimuli. *Neuroscience* 103, 1043–1050. doi:10.1016/S0306-4522(01)00036-7.

Crane, L., Goddard, L., and Pring, L. (2009). Sensory processing in adults with autism spectrum disorders. *Autism* 13, 215–228. doi:10.1177/1362361309103794.

D'Mello, S. R. (2021). MECP2 and the biology of MECP2 duplication syndrome. *J. Neurochem.* 159, 29–60. doi:10.1111/jnc.15331.

D'Souza, R. D., and Burkhalter, A. (2017). A Laminar Organization for Selective Cortico-Cortical Communication. *Front. Neuroanat.* 11. doi:10.3389/fnana.2017.00071.

De Jaco, A., Bernardini, L., Rosati, J., and Tata, A. M. (2016). Alpha-7 Nicotinic Receptors in Nervous System Disorders: From Function to Therapeutic Perspectives. *Cent. Nerv. Syst. Agents Med. Chem.* 17. doi:10.2174/1871524916666160729111446.

DeFelipe, J., Alonso-Nanclares, L., and Arellano, J. I. (2002). Microstructure of the neocortex: comparative aspects. *J. Neurocytol.* 31, 299–316. doi:10.1023/a:1024130211265.

Delling, J. P., and Boeckers, T. M. (2021). Comparison of SHANK3 deficiency in animal models: phenotypes, treatment strategies, and translational implications. *J. Neurodev. Disord.* 13, 55. doi:10.1186/s11689-021-09397-8.

Dennis, M. K., Field, A. S., Burai, R., Ramesh, C., Whitney, K., Bologa, C. G., et al. (2012). Structures and Molecular Mechanisms for Common 15q13.3 Microduplications Involving CHRNA7: Benign or Pathological? *Hum Mutat* 127, 358–366. doi:10.1002/humu.21284.Structures.

Dhamne, S. C., Silverman, J. L., Super, C. E., Lammers, S. H. T., Hameed, M. Q., Modi, M. E., et al. (2017). Replicable in vivo physiological and behavioral phenotypes of the Shank3B null mutant mouse model of autism. *Mol. Autism* 8, 26. doi:10.1186/s13229-017-0142-z.

Di Bonito, M., and Studer, M. (2017). Cellular and molecular underpinnings of neuronal assembly in the central auditory system during mouse development. *Front. Neural Circuits* 11, 1–25. doi:10.3389/fncir.2017.00018.

Domínguez-Iturza, N., Lo, A. C., Shah, D., Armendáriz, M., Vannelli, A., Mercaldo, V., et al. (2019). The autism- and schizophrenia-associated protein CYFIP1 regulates bilateral brain connectivity and behaviour. *Nat. Commun.* 10, 1–13. doi:10.1038/s41467-019-11203-y.

Drapeau, E., Riad, M., Kajiwara, Y., and Buxbaum, J. D. (2018). Behavioral Phenotyping of an Improved Mouse Model of Phelan–McDermid Syndrome with a Complete Deletion of the Shank3 Gene. *eneuro* 5, ENEURO.0046-18.2018. doi:10.1523/ENEURO.0046-18.2018.

Dubiel, A., and Kulesza, R. J. (2016). Prenatal valproic acid exposure disrupts tonotopic c-Fos expression in the rat brainstem. *Neuroscience* 324, 511–523. doi:10.1016/j.neuroscience.2016.01.030.

Durand, C. M., Betancur, C., Boeckers, T. M., Bockmann, J., Chaste, P., Fauchereau, F., et al. (2007). Mutations in the gene encoding the synaptic scaffolding protein SHANK3 are associated with autism spectrum disorders. *Nat. Genet.* 39, 25–27. doi:10.1038/ng1933.

Elsabbagh, M., Divan, G., Koh, Y.-J., Kim, Y. S., Kauchali, S., Marcín, C., et al. (2012). Global Prevalence of Autism and Other Pervasive Developmental Disorders. *Autism Res.* 5, 160–179. doi:10.1002/aur.239.

Engineer, C. T., Centanni, T. M., Im, K. W., Borland, M. S., Moreno, N. A., Carraway, R. S., et al. (2014a). Degraded auditory processing in a rat model of autism limits the speech representation in non-primary auditory cortex. *Dev. Neurobiol.* 74, 972–986. doi:10.1002/dneu.22175.

Engineer, C. T., Centanni, T. M., Im, K. W., Rahebi, K. C., Buell, E. P., and Kilgard, M. P. (2014b). Degraded speech sound processing in a rat model of fragile X syndrome. *Brain Res.* 1564, 72–84. doi:10.1016/j.brainres.2014.03.049.

Engineer, C. T., Rahebi, K. C., Borland, M. S., Buell, E. P., Im, K. W., Wilson, L. G., et al. (2018). Shank3-deficient rats exhibit degraded cortical responses to sound. *Autism Res.* 11, 59–68. doi:10.1002/aur.1883.

Esclassan, F., Francois, J., Phillips, K. G., Loomis, S., and Gilmour, G. (2015). Phenotypic characterization of nonsocial behavioral impairment in neurexin 1α knockout rats. *Behav. Neurosci.* 129, 74–85. doi:10.1037/bne0000024.

Felix, R. A., Chavez, V. A., Novicio, D. M., Morley, B. J., and Portfors, C. V. (2019). Nicotinic acetylcholine receptor subunit α7-knockout mice exhibit degraded auditory temporal processing. *J. Neurophysiol.* 122, 451–465. doi:10.1152/jn.00170.2019.

Gandal, M. J., Edgar, J. C., Ehrlichman, R. S., Mehta, M., Roberts, T. P. L., and Siegel, S. J. (2010). Validating γ oscillations and delayed auditory responses as translational biomarkers of autism. *Biol. Psychiatry* 68, 1100–1106. doi:10.1016/j.biopsych.2010.09.031.

Gandhi, T., and Lee, C. C. (2021). Neural Mechanisms Underlying Repetitive Behaviors in Rodent Models of Autism Spectrum Disorders. *Front. Cell. Neurosci.* 14. doi:10.3389/fncel.2020.592710.

Garcia-Pino, E., Gessele, N., and Koch, U. (2017). Enhanced excitatory connectivity and disturbed sound processing in the auditory brainstem of fragile X mice. *J. Neurosci.* 37, 7403–7419. doi:10.1523/JNEUROSCI.2310-16.2017.

Gkogkas, C. G., Khoutorsky, A., Cao, R., Jafarnejad, S. M., Prager-Khoutorsky, M., Giannakas, N., et al. (2014). Pharmacogenetic Inhibition of eIF4E-Dependent Mmp9 mRNA Translation Reverses Fragile X Syndrome-like Phenotypes. *Cell Rep.* 9, 1742–1755. doi:10.1016/j.celrep.2014.10.064.

Gogolla, N., Takesian, A. E., Feng, G., Fagiolini, M., and Hensch, T. K. (2014). Sensory Integration in Mouse Insular Cortex Reflects GABA Circuit Maturation. *Neuron* 83, 894–905. doi:10.1016/j.neuron.2014.06.033.

Gomes, E., Pedroso, F. S., and Wagner, M. B. (2008). Hipersensibilidade auditiva no transtorno do espectro autístico. *Pró-Fono Rev. Atualização Científica* 20, 279–284. doi:10.1590/S0104-56872008000400013.

Hacohen-Kleiman, G., Yizhar-Barnea, O., Touloumi, O., Lagoudaki, R., Avraham, K. B., Grigoriadis, N., et al. (2019). Atypical Auditory Brainstem Response and Protein Expression Aberrations Related to ASD and Hearing Loss in the Adnp Haploinsufficient Mouse Brain. *Neurochem. Res.* 44, 1494–1507. doi:10.1007/s11064-019-02723-6.

Herbert, M. R. (2010). Contributions of the environment and environmentally vulnerable physiology to autism spectrum disorders. *Curr. Opin. Neurol.* 23, 103–110.

doi:10.1097/WCO.0b013e328336a01f.

Ida-Eto, M., Hara, N., Ohkawara, T., and Narita, M. (2017). Mechanism of auditory hypersensitivity in human autism using autism model rats. *Pediatr. Int.* 59, 404–407. doi:10.1111/ped.13186.

Jaramillo, T. C., Speed, H. E., Xuan, Z., Reimers, J. M., Escamilla, C. O., Weaver, T. P., et al. (2017). Novel Shank3 mutant exhibits behaviors with face validity for autism and altered striatal and hippocampal function. *Autism Res.* 10, 42–65. doi:10.1002/aur.1664.

Jaramillo, T. C., Speed, H. E., Xuan, Z., Reimers, J. M., Liu, S., and Powell, C. M. (2016). Altered Striatal Synaptic Function and Abnormal Behaviour in Shank3 Exon4-9 Deletion Mouse Model of Autism. *Autism Res.* 9, 350–375. doi:10.1002/aur.1529.

Jonak, C. R., Sandhu, M. S., Assad, S. A., Barbosa, J. A., Makhija, M., and Binder, D. K. (2021). The PDE10A Inhibitor TAK-063 Reverses Sound-Evoked EEG Abnormalities in a Mouse Model of Fragile X Syndrome. *Neurotherapeutics* 18, 1175–1187. doi:10.1007/s13311-021-01005-w.

Knipper, M., Van Dijk, P., Nunes, I., Rüttiger, L., and Zimmermann, U. (2013). Advances in the neurobiology of hearing disorders: Recent developments regarding the basis of tinnitus and hyperacusis. *Prog. Neurobiol.* 111, 17–33. doi:10.1016/j.pneurobio.2013.08.002.

Kokash, J., Alderson, E. M., Reinhard, S. M., Crawford, C. A., Binder, D. K., Ethell, I. M., et al. (2019). Genetic reduction of MMP-9 in the Fmr1 KO mouse partially rescues prepulse inhibition of acoustic startle response. *Brain Res.* 1719, 24–29. doi:10.1016/j.brainres.2019.05.029.

Krüttner, S., Falasconi, A., Valbuena, S., Galimberti, I., Bouwmeester, T., Arber, S., et al. (2022). Absence of familiarity triggers hallmarks of autism in mouse model through aberrant tail-of-striatum and prelimbic cortex signaling. *Neuron* 110, 1468-1482.e5. doi:10.1016/j.neuron.2022.02.001.

Kulinich, A. O., Reinhard, S. M., Rais, M., Lovelace, J. W., Scott, V., Binder, D. K., et al. (2020). Beneficial effects of sound exposure on auditory cortex development in a mouse model of Fragile X Syndrome. *Neurobiol. Dis.* 134, 104622. doi:10.1016/j.nbd.2019.104622.

Lee, J., Chung, C., Ha, S., Lee, D., Kim, D.-Y., Kim, H., et al. (2015). Shank3-mutant mice lacking exon 9 show altered excitation/inhibition balance, enhanced rearing, and spatial memory deficit. *Front. Cell. Neurosci.* 9. doi:10.3389/fncel.2015.00094.

Lee, S.-Y., Vuong, T. A., So, H.-K., Kim, H.-J., Kim, Y. Bin, Kang, J.-S., et al. (2020). PRMT7 deficiency causes dysregulation of the HCN channels in the CA1 pyramidal cells and impairment of social behaviors. *Exp. Mol. Med.* 52, 604–614. doi:10.1038/s12276-020-0417-x.

Leekam, S. R., Nieto, C., Libby, S. J., Wing, L., and Gould, J. (2007). Describing the sensory abnormalities of children and adults with autism. *J. Autism Dev. Disord.* 37, 894–910. doi:10.1007/s10803-006-

0218-7.

Liu, C., Li, C., Hu, C., Wang, Y., Lin, J., Jiang, Y., et al. (2018). CRISPR/Cas9-induced shank3b mutant zebrafish display autism-like behaviors. *Mol. Autism* 9, 23. doi:10.1186/s13229-018-0204-x.

Liu, H., Huang, X., Xu, J., Mao, H., Li, Y., Ren, K., et al. (2021). Dissection of the relationship between anxiety and stereotyped self-grooming using the Shank3B mutant autistic model, acute stress model and chronic pain model. *Neurobiol. Stress* 15, 100417. doi:10.1016/j.ynstr.2021.100417.

Lörincz, A., Notomi, T., Tamás, G., Shigemoto, R., and Nusser, Z. (2002). Polarized and compartment-dependent distribution of HCN1 in pyramidal cell dendrites. *Nat. Neurosci.* 5, 1185–1193. doi:10.1038/nn962.

Lovelace, J. W., Ethell, I. M., Binder, D. K., and Razak, K. A. (2018). Translation-relevant EEG phenotypes in a mouse model of Fragile X Syndrome. *Neurobiol. Dis.* 115, 39–48. doi:10.1016/j.nbd.2018.03.012.

Lovelace, J. W., Ethell, I. M., Binder, D. K., and Razak, K. A. (2020a). Minocycline Treatment Reverses Sound Evoked EEG Abnormalities in a Mouse Model of Fragile X Syndrome. *Front. Neurosci.* 14, 1–16. doi:10.3389/fnins.2020.00771.

Lovelace, J. W., Rais, M., Palacios, A. R., Shuai, X. S., Bishay, S., Popa, O., et al. (2020b). Deletion of Fmr1 from Forebrain Excitatory Neurons Triggers Abnormal Cellular, EEG, and Behavioral Phenotypes in the Auditory Cortex of a Mouse Model of Fragile X Syndrome. *Cereb. Cortex* 30, 969–988. doi:10.1093/cercor/bhz141.

Lovelace, J. W., Wen, T. H., Reinhard, S., Hsu, M. S., Sidhu, H., Ethell, I. M., et al. (2016). Matrix metalloproteinase-9 deletion rescues auditory evoked potential habituation deficit in a mouse model of Fragile X Syndrome. *Neurobiol. Dis.* 89, 126–135. doi:10.1016/j.nbd.2016.02.002.

Lukose, R., Schmidt, E., Wolski, T. P., Murawski, N. J., and Kulesza, R. J. (2011). Malformation of the superior olivary complex in an animal model of autism. *Brain Res.* 1398, 102–112. doi:10.1016/j.brainres.2011.05.013.

Maciag, D., Simpson, K. L., Coppinger, D., Lu, Y., Wang, Y., Lin, R. C. S., et al. (2006). Neonatal antidepressant exposure has lasting effects on behavior and serotonin circuitry. *Neuropsychopharmacology* 31, 47–57. doi:10.1038/sj.npp.1300823.

Malmierca, M. S. (2003). "The Structure And Physiology Of The Rat Auditory System: An Overview," in *International Review of Neurobiology*, 147–211. doi:10.1016/S0074-7742(03)56005-6.

Mansour, Y., Ahmed, S. N., and Kulesza, R. (2021). Abnormal morphology and subcortical projections to the medial geniculate in an animal model of autism. *Exp. Brain Res.* 239, 381–400.

doi:10.1007/s00221-020-05982-w.

Mansour, Y., Mangold, S., Chosky, D., and Kulesza, R. J. (2019). Auditory Midbrain Hypoplasia and Dysmorphology after Prenatal Valproic Acid Exposure. *Neuroscience* 396, 79–93. doi:10.1016/j.neuroscience.2018.11.016.

Marco, E. J., Hinkley, L. B. N., Hill, S. S., and Nagarajan, S. S. (2011). Sensory Processing in Autism: A Review of Neurophysiologic Findings. *Pediatr. Res.* 69, 48R-54R. doi:10.1203/PDR.0b013e3182130c54.

Masini, E., Loi, E., Vega-Benedetti, A. F., Carta, M., Doneddu, G., Fadda, R., et al. (2020). An Overview of the Main Genetic, Epigenetic and Environmental Factors Involved in Autism Spectrum Disorder Focusing on Synaptic Activity. *Int. J. Mol. Sci.* 21, 8290. doi:10.3390/ijms21218290.

Matsuzaki, H., Iwata, K., Manabe, T., and Mori, N. (2012). Triggers for Autism: Genetic and Environmental Factors. *J. Cent. Nerv. Syst. Dis.* 4, JCNSD.S9058. doi:10.4137/JCNSD.S9058.

Mei, Y., Monteiro, P., Zhou, Y., Kim, J.-A., Gao, X., Fu, Z., et al. (2016). Adult restoration of Shank3 expression rescues selective autistic-like phenotypes. *Nature* 530, 481–484. doi:10.1038/nature16971.

Monteggia, L. M., Eisch, A. J., Tang, M. D., Kaczmarek, L. K., and Nestler, E. J. (2000). Cloning and localization of the hyperpolarization-activated cyclic nucleotide-gated channel family in rat brain. *Mol. Brain Res.* 81, 129–139. doi:10.1016/S0169-328X(00)00155-8.

Monteiro, P., and Feng, G. (2017). SHANK proteins: roles at the synapse and in autism spectrum disorder. *Nat. Rev. Neurosci.* 18, 147–157. doi:10.1038/nrn.2016.183.

Moosmang, S., Biel, M., Hofmann, F., and Ludwig, A. (1999). Differential Distribution of Four Hyperpolarization-Activated Cation Channels in Mouse Brain. *Biol. Chem.* 380, 975–980. doi:10.1515/BC.1999.121.

Muhle, R., Trentacoste, S. V., and Rapin, I. (2004). The Genetics of Autism. *Pediatrics* 113, e472–e486. doi:10.1542/peds.113.5.e472.

Murphey, D. K., Herman, A. M., and Arenkiel, B. R. (2014). Dissecting inhibitory brain circuits with genetically-targeted technologies. *Front. Neural Circuits* 8. doi:10.3389/fncir.2014.00124.

Nagode, D. A., Meng, X., Winkowski, D. E., Smith, E., Khan-Tareen, H., Kareddy, V., et al. (2017). Abnormal Development of the Earliest Cortical Circuits in a Mouse Model of Autism Spectrum Disorder. *Cell Rep.* 18, 1100–1108. doi:10.1016/j.celrep.2017.01.006.

Nakamura, M., Valerio, P., Bhumika, S., and Barkat, T. R. (2020). Sequential Organization of Critical Periods in the Mouse Auditory System. *Cell Rep.* 32, 108070. doi:10.1016/j.celrep.2020.108070.

Nguyen, A. O., Binder, D. K., Ethell, I. M., and Razak, K. A. (2020). Abnormal development of auditory responses in the inferior colliculus of a mouse model of Fragile X Syndrome. *J. Neurophysiol.* 123, 2101–2121. doi:10.1152/jn.00706.2019.

Noma, A., and Irisawa, H. (1976). Membrane currents in the rabbit sinoatrial node cell as studied by the double microelectrode method. *Pflugers Arch. Eur. J. Physiol.* 364, 45–52. doi:10.1007/BF01062910.

Notomi, T., and Shigemoto, R. (2004). Immunohistochemical localization of Ih channel subunits, HCN1-4, in the rat brain. *J. Comp. Neurol.* 471, 241–276. doi:10.1002/cne.11039.

Peça, J., Feliciano, C., Ting, J. T., Wang, W., Wells, M. F., Venkatraman, T. N., et al. (2011). Shank3 mutant mice display autistic-like behaviours and striatal dysfunction. *Nature* 472, 437–442. doi:10.1038/nature09965.

Peñagarikano, O., Abrahams, B. S., Herman, E. I., Winden, K. D., Gdalyahu, A., Dong, H., et al. (2011). Absence of CNTNAP2 leads to epilepsy, neuronal migration abnormalities, and core autism-related deficits. *Cell* 147, 235–246. doi:10.1016/j.cell.2011.08.040.

Pirbhoy, P. S., Jonak, C. R., Syed, R., Argueta, D. A., Perez, P. A., Wiley, M. B., et al. (2021). Increased 2-arachidonoyl-sn-glycerol levels normalize cortical responses to sound and improve behaviors in Fmr1 KO mice. *J. Neurodev. Disord.* 13, 47. doi:10.1186/s11689-021-09394-x.

Pirbhoy, P. S., Rais, M., Lovelace, J. W., Woodard, W., Razak, K. A., Binder, D. K., et al. (2020). Acute pharmacological inhibition of matrix metalloproteinase-9 activity during development restores perineuronal net formation and normalizes auditory processing in Fmr1 KO mice. *J. Neurochem.* 155, 538–558. doi:10.1111/jnc.15037.

Pitzer, C., Kurpiers, B., and Eltokhi, A. (2022). Sex Differences in Depression-Like Behaviors in Adult Mice Depend on Endophenotype and Strain. *Front. Behav. Neurosci.* 16. doi:10.3389/fnbeh.2022.838122.

Reinhard, S. M., Rais, M., Afroz, S., Hanania, Y., Pendi, K., Espinoza, K., et al. (2019). Reduced perineuronal net expression in Fmr1 KO mice auditory cortex and amygdala is linked to impaired fear-associated memory. *Neurobiol. Learn. Mem.* 164, 107042. doi:10.1016/j.nlm.2019.107042.

Rendall, A. R., Perrino, P. A., Buscarello, A. N., and Fitch, R. H. (2019). Shank3B mutant mice display pitch discrimination enhancements and learning deficits. *Int. J. Dev. Neurosci.* 72, 13–21. doi:10.1016/j.ijdevneu.2018.10.003.

Robertson, C. E., and Baron-Cohen, S. (2017). Sensory perception in autism. *Nat. Rev. Neurosci.* 18, 671–684. doi:10.1038/nrn.2017.112.

Robinson, R. B., and Siegelbaum, S. A. (2003). Hyperpolarization-Activated Cation Currents: From Molecules to Physiological Function. *Annu. Rev. Physiol.* 65, 453–480. doi:10.1146/annurev.physiol.65.092101.142734.

Rodenas-Cuadrado, P., Ho, J., and Vernes, S. C. (2014). Shining a light on CNTNAP2: Complex functions to complex disorders. *Eur. J. Hum. Genet.* 22, 171–178. doi:10.1038/ejhg.2013.100.

Rotschafer, S. E., and Cramer, K. S. (2017). Developmental emergence of phenotypes in the auditory brainstem nuclei of Fmr1 knockout mice. *eNeuro* 4. doi:10.1523/ENEURO.0264-17.2017.

Rotschafer, S. E., Marshak, S., and Cramer, K. S. (2015). Deletion of Fmr1 alters function and synaptic inputs in the auditory brainstem. *PLoS One* 10, 1–15. doi:10.1371/journal.pone.0117266.

Rotschafer, S., and Razak, K. (2013). Altered auditory processing in a mouse model of fragile X syndrome. *Brain Res.* 1506, 12–24. doi:10.1016/j.brainres.2013.02.038.

Ruby, K., Falvey, K., and Kulesza, R. J. (2015). Abnormal neuronal morphology and neurochemistry in the auditory brainstem of Fmr1 knockout rats. *Neuroscience* 303, 285–298. doi:10.1016/j.neuroscience.2015.06.061.

Rylaarsdam, L., and Guemez-Gamboa, A. (2019). Genetic Causes and Modifiers of Autism Spectrum Disorder. *Front. Cell. Neurosci.* 13. doi:10.3389/fncel.2019.00385.

Sanes, D. H., and Kotak, V. C. (2011). Developmental plasticity of auditory cortical inhibitory synapses. *Hear. Res.* 279, 140–148. doi:10.1016/j.heares.2011.03.015.

Santoro, B., Chen, S., Lüthi, A., Pavlidis, P., Shumyatsky, G. P., Tibbs, G. R., et al. (2000). Molecular and Functional Heterogeneity of Hyperpolarization-Activated Pacemaker Channels in the Mouse CNS. *J. Neurosci.* 20, 5264–5275. doi:10.1523/JNEUROSCI.20-14-05264.2000.

Santoro, B., and Tibbs, G. (1999). The HCN Gene Family: Molecular Basis of the Hyperpolarization-Activated Pacemaker Channels. *Ann. N. Y. Acad. Sci.* 868, 741–764. doi:10.1111/j.1749-6632.1999.tb11353.x.

Sarn, N., Thacker, S., Lee, H., and Eng, C. (2021). Germline nuclear-predominant Pten murine model exhibits impaired social and perseverative behavior, microglial activation, and increased oxytocinergic activity. *Mol. Autism* 12, 1–19. doi:10.1186/s13229-021-00448-4.

Satterstrom, F. K., Kosmicki, J. A., Wang, J., Breen, M. S., De Rubeis, S., An, J.-Y., et al. (2020). Large-Scale Exome Sequencing Study Implicates Both Developmental and Functional Changes in the Neurobiology of Autism. *Cell* 180, 568-584.e23. doi:10.1016/j.cell.2019.12.036.

Schaaf, C. P. (2014). Nicotinic acetylcholine receptors in human genetic disease. *Genet. Med.* 16, 649–656. doi:10.1038/gim.2014.9.

Schmeisser, M. J., Ey, E., Wegener, S., Bockmann, J., Stempel, A. V., Kuebler, A., et al. (2012). Autistic-like behaviours and hyperactivity in mice lacking ProSAP1/Shank2. *Nature* 486, 256–260. doi:10.1038/nature11015.

Schridde, U., Strauss, U., Bräuer, A. U., and van Luijtelaar, G. (2006). Environmental manipulations early in development alter seizure activity, I h and HCN1 protein expression later in life. *Eur. J. Neurosci.* 23, 3346–3358. doi:10.1111/j.1460-9568.2006.04865.x.

Scott, K. E., Schormans, A. L., Pacoli, K. Y., De Oliveira, C., Allman, B. L., and Schmid, S. (2018). Altered auditory processing, filtering, and reactivity in the cntnap2 knock-out rat model for neurodevelopmental disorders. *J. Neurosci.* 38, 8588–8604. doi:10.1523/JNEUROSCI.0759-18.2018.

Sethna, F., Moon, C., and Wang, H. (2014). From FMRP Function to Potential Therapies for Fragile X Syndrome. *Neurochem. Res.* 39, 1016–1031. doi:10.1007/s11064-013-1229-3.

Shah, M. M. (2014). Cortical HCN channels: function, trafficking and plasticity. *J. Physiol.* 592, 2711–2719. doi:10.1113/jphysiol.2013.270058.

Shah, M. M. (2016). Recording Hyperpolarization-Activated Cyclic Nucleotide-Gated Channel Currents (I h) in Neurons. *Cold Spring Harb. Protoc.* 2016, pdb.prot091462. doi:10.1101/pdb.prot091462.

Sohal, V. S., and Rubenstein, J. L. R. (2019). Excitation-inhibition balance as a framework for investigating mechanisms in neuropsychiatric disorders. *Mol. Psychiatry* 24, 1248–1257. doi:10.1038/s41380-019-0426-0.

Song, T.-J., Lan, X.-Y., Wei, M.-P., Zhai, F.-J., Boeckers, T. M., Wang, J.-N., et al. (2019). Altered Behaviors and Impaired Synaptic Function in a Novel Rat Model With a Complete Shank3 Deletion. *Front. Cell. Neurosci.* 13. doi:10.3389/fncel.2019.00111.

Stanfield, C. L. (2013). *Principles of Human Physiology*. 5th editio. Pearson.

Strumbos, J. G., Brown, M. R., Kronengold, J., Polley, D. B., and Kaczmarek, L. K. (2010). Fragile X mental retardation protein is required for rapid experience-dependent regulation of the potassium channel Kv3.1b. *J. Neurosci.* 30, 10263–10271. doi:10.1523/JNEUROSCI.1125-10.2010.

Sturman, O., Germain, P.-L., and Bohacek, J. (2018). Exploratory rearing: a context- and stress-sensitive behavior recorded in the open-field test. *Stress* 21, 443–452. doi:10.1080/10253890.2018.1438405.

Sztainberg, Y., and Zoghbi, H. Y. (2016). Lessons learned from studying syndromic autism spectrum disorders. *Nat. Neurosci.* 19, 1408–1417. doi:10.1038/nn.4420.

The Dutch-Belgian Fragile X Consorthium, Bakker, C. E., Verheij, C., Willemsen, R., van der Helm, R.,

Oerlemans, F., et al. (1994). Fmr1 knockout mice: A model to study fragile X mental retardation. *Cell* 78, 23–33. doi:10.1016/0092-8674(94)90569-X.

Tomchek, S. D., and Dunn, W. (2007). Sensory Processing in Children With and Without Autism: A Comparative Study Using the Short Sensory Profile. *Am. J. Occup. Ther.* 61, 190–200. doi:10.5014/ajot.61.2.190.

Tremblay, R., Lee, S., and Rudy, B. (2016). GABAergic Interneurons in the Neocortex: From Cellular Properties to Circuits. *Neuron* 91, 260–292. doi:10.1016/j.neuron.2016.06.033.

Truong, D. T., Rendall, A. R., Castelluccio, B. C., Eigsti, I. M., and Holly, R. (2015). Auditory processing and morphological anomalies in medial geniculate nucleus of Cntnap2 mutant mice. *Behav. Neurosci.* 129, 731–741. doi:10.1037/bne0000096.

Tsugiyama, L. E., Ida-Eto, M., Ohkawara, T., Noro, Y., and Narita, M. (2020). Altered neuronal activity in the auditory brainstem following sound stimulation in thalidomide-induced autism model rats. *Congenit. Anom. (Kyoto).* 60, 82–86. doi:10.1111/cga.12353.

Vicidomini, C., Ponzoni, L., Lim, D., Schmeisser, M. J., Reim, D., Morello, N., et al. (2017). Pharmacological enhancement of mGlu5 receptors rescues behavioral deficits in SHANK3 knock-out mice. *Mol. Psychiatry* 22, 689–702. doi:10.1038/mp.2016.30.

Visel, A., Alvarez-Bolado, G., Thaller, C., and Eichele, G. (2006). Comprehensive analysis of the expression patterns of the adenylate cyclase gene family in the developing and adult mouse brain. *J. Comp. Neurol.* 496, 684–697. doi:10.1002/cne.20953.

Wahl-Schott, C., and Biel, M. (2009). HCN channels: Structure, cellular regulation and physiological function. *Cell. Mol. Life Sci.* 66, 470–494. doi:10.1007/s00018-008-8525-0.

Wang, X., Bey, A. L., Katz, B. M., Badea, A., Kim, N., David, L. K., et al. (2016). Altered mGluR5-Homer scaffolds and corticostriatal connectivity in a Shank3 complete knockout model of autism. *Nat. Commun.* 7, 11459. doi:10.1038/ncomms11459.

Wang, X., McCoy, P. A., Rodriguiz, R. M., Pan, Y., Je, H. S., Roberts, A. C., et al. (2011). Synaptic dysfunction and abnormal behaviors in mice lacking major isoforms of Shank3. *Hum. Mol. Genet.* 20, 3093–3108. doi:10.1093/hmg/ddr212.

Wang, X., Xu, Q., Bey, A. L., Lee, Y., and Jiang, Y. (2014). Transcriptional and functional complexity of Shank3 provides a molecular framework to understand the phenotypic heterogeneity of SHANK3 causing autism and Shank3 mutant mice. *Mol. Autism* 5, 30. doi:10.1186/2040-2392-5-30.

Wen, T. H., Afroz, S., Reinhard, S. M., Palacios, A. R., Tapia, K., Binder, D. K., et al. (2018). Genetic Reduction of Matrix Metalloproteinase-9 Promotes Formation of Perineuronal Nets Around

Parvalbumin-Expressing Interneurons and Normalizes Auditory Cortex Responses in Developing Fmr1 Knock-Out Mice. *Cereb. Cortex* 28, 3951–3964. doi:10.1093/cercor/bhx258.

Werling, D. M., and Geschwind, D. H. (2013). Sex differences in autism spectrum disorders. *Curr. Opin. Neurol.* 26, 146–153. doi:10.1097/WCO.0b013e32835ee548.

Wilson, H. L., Wong, A. C. C., Shaw, S. R., Tse, W.-Y., Stapleton, G. A., Phelan, M. C., et al. (2003). Molecular characterisation of the 22q13 deletion syndrome supports the role of haploinsufficiency of SHANK3/PROSAP2 in the major neurological symptoms. *J. Med. Genet.* 40, 575–84. doi:10.1136/jmg.40.8.575.

Xiong, Q., Oviedo, H. V., Trotman, L. C., and Zador, A. M. (2012). PTEN regulation of local and long-range connections in mouse auditory cortex. *J. Neurosci.* 32, 1643–1652. doi:10.1523/JNEUROSCI.4480-11.2012.

Yalcin, I., Aksu, F., and Belzung, C. (2005). Effects of desipramine and tramadol in a chronic mild stress model in mice are altered by yohimbine but not by pindolol. *Eur. J. Pharmacol.* 514, 165–174. doi:10.1016/j.ejphar.2005.03.029.

Yang, M., Bozdagi, O., Scattoni, M. L., Wohr, M., Roullet, F. I., Katz, A. M., et al. (2012). Reduced Excitatory Neurotransmission and Mild Autism-Relevant Phenotypes in Adolescent Shank3 Null Mutant Mice. *J. Neurosci.* 32, 6525–6541. doi:10.1523/JNEUROSCI.6107-11.2012.

Yang, S.-S., Li, Y.-C., Coley, A. A., Chamberlin, L. A., Yu, P., and Gao, W.-J. (2018). Cell-Type Specific Development of the Hyperpolarization-Activated Current, Ih, in Prefrontal Cortical Neurons. *Front. Synaptic Neurosci.* 10. doi:10.3389/fnsyn.2018.00007.

Yi, F., Danko, T., Botelho, S. C., Patzke, C., Pak, C., Wernig, M., et al. (2016). Autism-associated SHANK3 haploinsufficiency causes Ih channelopathy in human neurons. *Science (80-.).* 352, aaf2669–aaf2669. doi:10.1126/science.aaf2669.

Yoo, Y.-E., Yoo, T., Lee, S., Lee, J., Kim, D., Han, H.-M., et al. (2019). Shank3 Mice Carrying the Human Q321R Mutation Display Enhanced Self-Grooming, Abnormal Electroencephalogram Patterns, and Suppressed Neuronal Excitability and Seizure Susceptibility. *Front. Mol. Neurosci.* 12. doi:10.3389/fnmol.2019.00155.

Zhang, X.-C., Shu, L.-Q., Zhao, X.-S., and Li, X.-K. (2019). Autism spectrum disorders: autistic phenotypes and complicated mechanisms. *World J. Pediatr.* 15, 17–25. doi:10.1007/s12519-018-0210-2.

Zhou, C., Yan, S., Qian, S., Wang, Z., Shi, Z., Xiong, Y., et al. (2019a). Atypical response properties of the auditory cortex of awake MECP2-overexpressing mice. *Front. Neurosci.* 13, 1–10. doi:10.3389/fnins.2019.00439.

Zhou, J., and Parada, L. F. (2012). PTEN signaling in autism spectrum disorders. *Curr. Opin. Neurobiol.* 22, 873–879. doi:10.1016/j.conb.2012.05.004.

Zhou, X., Feliciano, P., Shu, C., Wang, T., Astrovskaya, I., Hall, J. B., et al. (2022). Integrating de novo and inherited variants in 42,607 autism cases identifies mutations in new moderate-risk genes. *Nat. Genet.* 54, 1305–1319. doi:10.1038/s41588-022-01148-2.

Zhou, Y., Kaiser, T., Monteiro, P., Zhang, X., Van der Goes, M. S., Wang, D., et al. (2016). Mice with Shank3 Mutations Associated with ASD and Schizophrenia Display Both Shared and Distinct Defects. *Neuron* 89, 147–162. doi:10.1016/j.neuron.2015.11.023.

Zhou, Y., Sharma, J., Ke, Q., Landman, R., Yuan, J., Chen, H., et al. (2019b). Atypical behaviour and connectivity in SHANK3-mutant macaques. *Nature* 570, 326–331. doi:10.1038/s41586-019-1278-0.

Zhu, M., Idikuda, V. K., Wang, J., Wei, F., Kumar, V., Shah, N., et al. (2018). Shank3-deficient thalamocortical neurons show HCN channelopathy and alterations in intrinsic electrical properties. *J. Physiol.* 596, 1259–1276. doi:10.1113/JP275147.

Zimmerman, R., Patel, R., Smith, A., Pasos, J., and Kulesza, R. J. (2018). Repeated Prenatal Exposure to Valproic Acid Results in Auditory Brainstem Hypoplasia and Reduced Calcium Binding Protein Immunolabeling. *Neuroscience* 377, 53–68. doi:10.1016/j.neuroscience.2018.02.030.

Zimmerman, R., Smith, A., Fech, T., Mansour, Y., and Kulesza, R. J. (2020). In utero exposure to valproic acid disrupts ascending projections to the central nucleus of the inferior colliculus from the auditory brainstem. *Exp. Brain Res.* 238, 551–563. doi:10.1007/s00221-020-05729-7.

ANNEXES

Supplementary table 1. Statistical report of Student's *t*-tests and Mann-Whitney's tests.

Figure	Parameter	Groups	Mean ± SD	Statistical Report
10A.	Time grooming	WT	215.6 ± 93.41	Unpaired Student's t-test
		InsG3680$^{-/+}$	372.2 ± 62.13	t (8) = 3.121, p = 0.0142, d = 1.975
10B.	Grooming bouts	WT	13.60 ± 3.362	Unpaired Student's t-test
		InsG3680$^{-/+}$	19.20 ± 3.564	t (8) = 2.556, p = 0.03, d = 1.616
10C.	Time rearing	WT	87.60 ± 30.01	Unpaired Student's t-test
		InsG3680$^{-/+}$	52.60 ± 30.07	t (8) = 1.842, p = 0.10, d = 1.165
10D.	Rearing events	WT	40.40 ± 9.659	Unpaired Student's t-test
		InsG3680$^{-/+}$	25.20 ± 13.08	t (8) = 2.090, p = 0.07, d = 0.757
15A.	*mHcn1* | P14	WT	1.006 ± 0.1230	Unpaired Student's t-test (Welch's correction)
		InsG3680$^{-/+}$	1.745 ± 0.9653	t (5.162) = 1.861, p = 0.120, d = 1.074
	mHcn1 | P21	WT	1.014 ± 0.1880	Unpaired Student's t-test
		InsG3680$^{-/+}$	1.381 ± 0.3441	t (10) = 2.292, p = 0.045, d = 1.324
	mHcn1 | 10W	WT	1.026 ± 0.2373	Unpaired Student's t-test (Welch's correction)
		InsG3680$^{-/+}$	1.325 ± 0.8019	t (5.869) = 0.8763, p = 0.415, d = 0.506
15B.	*mHcn2* | P14	WT	1.009 ± 0.1487	Unpaired Student's t-test (Welch's correction)
		InsG3680$^{-/+}$	1.640 ± 1.082	t (5.189) = 1.415, p = 0.214, d = 0.817
	mHcn2 | P21	WT	1.211 ± 0.8406	Mann-Whitney test
		InsG3680$^{-/+}$	2.244 ± 0.9024	U = 4, p = 0.026, r = 0.8355
	mHcn2 | 10W	WT	1.025 ± 0.2307	Unpaired Student's t-test
		InsG3680$^{-/+}$	1.249 ± 0.2054	t (10) = 1.777, p = 0.106, d = 1.026
16A.	R_m control	WT	116.3 ± 51.37	Unpaired Student's t-test
		InsG3680$^{-/+}$	119.3 ± 55.23	U = 223.5, p = 0.918, r = 0.017
16B.	ΔR_m	WT	-10.80 ± 41.84	Unpaired Student's t-test
		InsG3680$^{-/+}$	-32.88 ± 54.71	t (19) = 1.045, p = 0.309, d = 0.453
17F.	ZD7288 effect on I_{ss} current density WT	Control	-6.779 ± 1.340	Paired Student's t-test
		ZD7288	-4.435 ± 1.004	t (10) = 6.309, p < 0.001, d = 1.980
	ZD7288 effect on I_{ss} current density *InsG3680*$^{-/+}$	Control	-9.206 ± 3.290	Paired Student's t-test
		ZD7288	-5.792 ± 3.049	t (8) = 4.059, p = 0.004, d = 1.076
17I.	τ_{act}	WT	12.28 ± 2.720	Unpaired Student's t-test
		InsG3680$^{-/+}$	10.93 ± 1.687	t (13) = 1.081, p = 0.299, d = 0.596
20A.	I_{ss} putative interneurons WT	Control	-6.857 ± 1.739	Paired Student's t-test
		ZD7288	-4.808 ± 1.104	t (5) = 3.311, p = 0.021, d = 1.407
	I_{ss} putative interneurons *InsG3680*$^{-/+}$	Control	-9.383 ± 1.487	Paired Student's t-test
		ZD7289	-5.121 ± 3.122	t (4) = 4.205, p = 0.014, d = 1.743
	I_{ss} putative princ. neurons WT	Control	-6.686 ± 0.8289	Paired Student's t-test
		ZD7289	-3.987 ± 0.7326	t (4) = 7.565, p = 0.002, d = 3.450
	I_{ss} putative princ. neurons *InsG3680*$^{-/+}$	Control	-7.459 ± 2.918	Paired Student's t-test
		ZD7289	-4.683 ± 1.117	t (3) = 2.825, p = 0.066, d = 1.256

Supplementary table 2. Factorial analysis.

Figure	Parameter		Main effect	Statistical Report
17G.	I_{ss} current density (control)	Mixed-effects ANOVA	Step (mV)	F (1.056, 22.17) = 168.7, p < 0.0001
			Genotype	F (1.000, 21.00) = 0.8091, p = 0.3786
			Interaction	F (1.022, 13.80) = 0.8828, p = 0.366
17H.	I_h current density	Mixed-effects ANOVA	Step (mV)	F (1.056, 22.17) = 168.7, p < 0.0001
			Genotype	F (1.000, 21.00) = 0.8091, p = 0.3786
			Interaction	F (1.022, 13.80) = 0.8828, p = 0.366
19A.	R_m control	Mixed-effects ANOVA	Cell type	F (1, 11) = 0.1705, p = 0.6876
			Genotype	F (1, 11) = 0.01123, p = 0.9175
			Interaction	F (1, 6) = 6.566, p = 0.0428
19B.	ΔR_m	Mixed-effects ANOVA	Cell type	F (1, 4) = 0.3663, p = 0.5777
			Genotype	F (1, 4) = 2.016, p = 0.2287
			Interaction	F (1, 3) = 0.8163, p = 0.4329
20C.	I_{ss} current density (control) Principal neurons	Mixed-effects ANOVA	Cell type	F (6, 60) = 136.8, p < 0.0001
			Genotype	F (1, 10) = 0.4345, p = 0.5247
			Interaction	F (6, 43) = 0.1756, p = 0.982
20D.	I_h current density Principal neurons	Mixed-effects ANOVA	Cell type	F (6, 36) = 44.55, p < 0.0001
			Genotype	F (1, 6) = 12.14, p = 0.0131
			Interaction	F (6, 10) = 7.986, p = 0.0024
			Bonferroni's *post-hoc* test for main effect of genotype:	
			-120 mV step: t (16) = 3.654, p = 0.015	
			-130 mV step: t (16) = 6.176, p < 0.0001	
20E.	I_{ss} current density (control) Interneurons	Mixed-effects ANOVA	Cell type	F (6, 60) = 45.57, p < 0.0001
			Genotype	F (1, 10) = 2.296, p = 0.1607
			Interaction	F (6, 39) = 2.108, p = 0.0743
20F.	I_h current density Interneurons	Mixed-effects ANOVA	Cell type	F (6, 30) = 27.35, p < 0.0001
			Genotype	F (1, 5) = 0.4193, p = 0.5458
			Interaction	F (6, 23) = 4.936, p = 0.0022